Transient Flow Boiling CHF under exponentially escalating heat inputs

by

Artyom Kossolapov

B.Eng. Nuclear Engineering

Peter the Great St. Petersburg Polytechnic University, 2015

SUBMITTED TO THE DEPARTMENT OF NUCLEAR SCIENCE AND ENGINEERING IN PARTIAL FULFILLMENT OF THE REQUIREMENTS FOR THE DEGREE OF

MASTER OF SCIENCE IN NUCLEAR SCIENCE AND ENGINEERING

AT THE

MASSACHUSETTS INSTITUTE OF TECHNOLOGY

FEBRUARY 2018

Author:_____

Artyom Kossolapov
Department of Nuclear Science and Engineering
January 24, 2018

Certified by:_____

Matteo Bucci, Ph. D.
Assistant Professor of Nuclear Science and Engineering
Thesis Supervisor

Certified by:_____

Jacopo Buongiorno, Ph. D.
TEPCO Professor of Nuclear Science and Engineering
Thesis Reader

Accepted by:_____

Ju Li, Ph. D.
Battelle Energy Alliance Professor of Nuclear Science and Engineering
Professor of Materials Science and Engineering
Chair, Department Committee on Graduate Students

Transient Flow Boiling CHF under exponentially escalating heat inputs

by

Artyom Kossolapov

Submitted to the Department of Nuclear Science and Engineering on January 24, 2018 in Partial Fulfillment of the Requirements for the Degree of Master of Science in Nuclear Science and Engineering

Abstract

Reactivity initiated accidents (RIAs) are a potential concern for nuclear reactor safety. In RIA scenarios, following the insertion of positive reactivity, e.g. by an unanticipated extraction of the control rods, the reactor power may increase exponentially. The period of the exponential rise, τ, depends on the amount of positive reactivity inserted, as well as the fuel composition. During such an event, boiling of the water coolant can provide not only an effective way of heat removal, but also a stabilizing, negative reactivity feedback. However, the reactor power could reach extremely high levels and lead to a boiling crisis, e.g. by departure from nucleate boiling (DNB), in turn leading to fuel damage.

The aim of the current work is to improve the understanding of transient DNB phenomena. This goal was achieved by running experiments on a specially designed flow boiling platform, which includes high speed video (HSV) and high speed infrared (HSIR) diagnostics. Specifically, the IR radiation recorded by the HSIR camera was analyzed with dedicated post processing algorithms that enable measurements of the time-dependent temperature and heat flux distributions on the boiling surface. Experiments were performed on a flat heater in upward flow conditions at atmospheric pressure. This work explores the effects of flow velocity, liquid subcooling and exponential power escalation period on critical heat flux (CHF). The results show that, for our flow conditions, the CHF value does not depend on the escalation period for periods longer than 100 ms, and is essentially the same as in steady-state boiling. For shorter periods, CHF increases as the escalation period decreases, and the effect of flow velocity becomes less important at short periods. Larger subcooling was shown to increase the CHF at all conditions. For extreme cases of 50 K and 75 K of subcooling the entire heating surface was covered by tiny bubbles. Those bubbles had a very short (less than 50 μs) lifetime and were quenched right after the nucleation. Such behavior prevented bubbles from coalescing and resulted in a very efficient heat transfer mechanism. CHF was observed at much higher values compared to steady boiling conditions, when nucleation site density and bubble size were large enough for the bubble to start coalescing. An interesting effect was observed for very short periods (5, 10 and 20 ms) and low subcoolings (10 K). At those conditions the boiling surface experiences CHF during the growth of the first generation of bubbles. Therefore, the points of ONB and CHF are almost coincident, with CHF delayed only by the time required for adjacent bubbles to coalesce and the microlayer underneath them to evaporate.

Thesis Supervisor: Matteo Bucci

Title: Assistant Professor of Nuclear Science and Engineering

Acknowledgements

First, I would like to thank my advisers: Professor Matteo Bucci and Professor Jacopo Buongiorno for all the support and knowledge that I received from them over the past two years. Skills that I acquired from you have shaped this work and are invaluable for my future career. You have created an amazing working atmosphere that made my years in your research group extremely enjoyable.

Second, I want to express my highest gratitude to Doctor Thomas J. McKrell. He has guided my laboratory work from my very first weeks at MIT. Dr. McKrell made me appreciate the complicated details that are crucial for achieving high quality results. His mentoring was a great inspiration for me.

My close friends: Stephen, Malik, Sam and Chris, thank you for the great support in our times of classes and quals. Days (and sometimes nights) we spent crushing the material as a study group were extremely productive and your company turned it into a wonderful experience.

Thanks to all my lab mates who were always there to help both with their knowledge and physical strength. Guan Yu, your knowledge and experience in transient boiling were extremely helpful. Andrew and Megan, this work would not be possible without your help; from preparing for the experiments to collecting the data you were there to help me.

Thanks to Prof. Eisa Alsafran with whom we had multiple fruitful discussions regarding the fascinating physics of transient CHF.

This work would not have been possible without funding from Commissariat à l'énergie atomique et aux énergies alternatives (CEA)

Lastly, I want to thank my family for all the support they have given me over these years. You have always been there for me, worrying about my hardships more than I did. It was your encouragement that sustained me through the most challenging times.

Contents

List of Figures

List of Tables

Nomenclature

$\dot{Q}_{max}$ – maximum reactor power during the power pulse, W
h_{com} – combined heat transfer coefficient for transient conduction and convection, W/(m^2·K)
h_{fg} – latent heat of evaporation, J/kg
$\dot{Q}$ – reactor thermal power, W
T_B – saturation temperature at atmospheric pressure, K
T_{cr} – critical temperature, K
T_f – fuel temperature, K
T_m – moderator temperature, K
V_1 – voltage between the positive electrode of the heater and the ground, V
V_2 – voltage between the negative electrode of the heater and the ground, V
V_s – voltage drop across electrical shunt, V
c_p – isobaric heat capacity, J/(kg·K)
l_0 – Laplace length, m
$q''_{c,ss,sat}$ – CHF in saturated steady state boiling, W/m^2
$q''_{c,ss}$ – CHF in steady-state boiling, W/m^2
$q''_{c,tr}$ – CHF in transient boiling, W/m^2
t_{max} – time when the reactor reaches the maximum power during the power pulse, s
v_1 – volumetric growth rate of the vapor patch, m^3/s
ΔT_i – heterogeneous nucleation wall superheat, K
ΔT_{sat} – wall superheat, K
ΔT_{sub} – bulk liquid subcooling, K
D_h – hydraulic diameter, m
J – rate of embryo formation, 1/(s·m^2)
k_i – effective neutron multiplication at i^{th} state of the reactor
P – pressure, Pa
x_e – equilibrium quality
Bo – boiling number
G – mass flux, kg/m^2·s
Pr – Prandtl number
Re – Reynolds number
T – temperature, K
g – gravitational acceleration, m/s^2
q'' – heat flux, W/m^2
t – time, s

Greek symbols

β_e – effective fraction of delayed neutrons
ζ_d – fuel Doppler coefficient of reactivity, 1/K
ζ_m – moderator temperature coefficient of reactivity, 1/K
ζ_v – void coefficient of reactivity
λ_D – the most dangerous Taylor instability wavelength, m
ρ_l – liquid density, kg/m^3
ρ_v – vapor density, kg/m^3
σ_B – saturated liquid surface tension at atmospheric pressure
τ_c – time required to evaporate liquid macrolayer, s
τ_d – vapor patch hovering period, s
Λ – effective neutron lifetime, s
μ - viscosity, Pa·s

α – void fraction
β – aperture angle of nucleation cavity
η – ratio between transient and steady state CHF
θ – solid-liquid contact angle
ν – kinematic viscosity, m^2/s
ρ – reactivity
σ – liquid surface tension, N/m
τ – period of the exponential power rise, s

Acronyms

CHF – critical heat flux
DC – direct current
DNB – departure from nucleate boiling
FDNB – fully developed nucleate boiling
FG – function generator
Fps – frames per second
HSDAS – high speed data acquisition system
HSIR – high speed infrared
HSN – heterogeneous spontaneous nucleation
HSV – high speed video
HTC – heat transfer coefficient
IR - infrared
ITO – indium tin oxide
LED – light emitting diode
LWR – light water reactor
ONB – onset of nucleate boiling
PTFE - PolyTetraFluoroEthylene
RIA – reactivity initiated accident

1. Introduction

Reactivity initiated accidents (RIAs) have been an active research topic from the beginning of the nuclear industry. Such accidents could be caused by a rapid extraction of control rods, which introduces a large positive reactivity, and may bring the reactor into a super prompt-critical state. This causes the reactor power $\dot{Q}$ to rise exponentially as $\dot{Q} \propto e^{t/\tau}$, where the power escalation period τ depends on the value of the reactivity step and the reactor fuel. For large reactivity insertions, the period τ could be as short as 1 ms. The occurrence of such transient poses a potential threat to the reactor fuel integrity. However, while boiling introduces a stabilizing, negative reactivity feedback, heat fluxes achieved during RIA can be high enough to cause departure from nucleate boiling (DNB). DNB can lead to fuel meltdown and failure of the cladding. If so, the molten fuel could be expulsed, fragmented and lead to steam explosion. Therefore, a thorough understanding of the DNB mechanism under RIA conditions should be achieved in order to improve the accuracy of safety analyses for such accidents.

In the current work, we present the methodology and results of an extensive experimental campaign aimed at improving the understanding of DNB phenomena during RIA transient. In the first chapter an overview of RIA scenarios and the current understanding of transient boiling phenomenon is given. Details of the experimental setup as well as procedures used in the current work are outlined in chapter 2. The discussion of results is presented in chapter 3.

1.1. Progression of Reactivity Initiated Accidents (RIAs)

RIAs have been an active research topic from the beginning of the nuclear industry. Several RIAs occurred in early reactor systems, e.g. the Idaho Falls SL-1 accident in 1961 [1]. Lessons learned from these early accidents led to improvements in design of new reactor systems, whereas the unknowns that they presented motivated thorough, additional research on the topic. The consequences of RIA depend on multiple properties including fuel composition and irradiation, coolant temperature, core geometry and, most importantly, the worth of the control element removed from the reactor.

Most reactor systems use control rods as the main control element of the nuclear reaction. Therefore, an unexpected control rod extraction from the reactor core could lead to RIA. The worth of the control rod can be defined by the amount of reactivity that is introduced when the control rod is removed from the reactor. The reactivity ρ is defined as the relative difference of effective neutron multiplication factors k_i between two states

$$\rho = \frac{k_1 - k_0}{k_1 \cdot k_0} \tag{1}$$

where we typically assume $k_0 = 1$ for comparison with a stable, critical reactor. The worth of the control rod determines how fast the reactor power will increase following the rod ejection. In general, the reactor power distribution will be a function of both space and time and cannot be calculated analytically. Nevertheless, there are several approximations that are useful for the understanding of RIA power transients. Such approximations are described below.

Depending on the worth of the removed rod, after the rod ejection, the reactor can be prompt sub- or super-critical. The reactor power after the rod removal is governed by both prompt and delayed neutrons. Point kinetics approximation allows to express this behavior as a sum of exponential

functions [2]. However, most of those exponential functions rapidly die out and the asymptotic behavior of the power rise can be expressed as

$$\dot{Q}(t) = \dot{Q}_0 \cdot \mathrm{e}^{t/\tau} \tag{2}$$

where τ is the reactor period. Note that since (2) describes an asymptotic behavior of the power rise the value of $\dot{Q}_0$ differs from the initial power of the reactor by the so-called prompt jump [3]. The reactor period provides a characteristic time scale for the transient. A larger worth of the ejected control rod results in a smaller value of the reactor period leading to a faster transient.

Real reactors have intrinsic reactivity feedback mechanisms that tend to counteract a runaway power rise described by Eq. (2). Major reactivity feedback mechanisms are summarized below:

- Doppler effect: it is the fastest of the reactivity feedback mechanisms. It depends on the temperature of the uranium fuel and does not experience a delay due to thermal transport processes. Physically, a higher temperature of the uranium fuel causes a widening of U^{238} capture resonances. This leads to a smaller resonance escape probability lowering neutron multiplication.
- Moderator temperature effect: it activates when the energy released during the power escalation in the fuel reaches the moderator, e.g. water, and starts to increase its temperature. Thermal expansion of the moderator results in fewer neutron-moderator interactions which stabilizes the power of under-moderated cores.
- The void effect can be viewed as a more powerful version of the moderator effect. It represents the change in reactivity when a gas phase is created in the reactor core. Most often voids are created during boiling of the reactor coolant. Since in LWRs the coolant is also the moderator, creation of the vapor phase dramatically reduces the density of the moderator hindering the neutron slowing down process.

The combined contribution of the above mentioned effects is summarized in

$$\frac{d\rho}{dt} = \zeta_d \cdot \frac{dT_f}{dt} + \zeta_m \cdot \frac{dT_m}{dt} + \zeta_v \cdot \frac{d\alpha}{dt} \tag{3}$$

where ζ_d, ζ_m and ζ_v are Doppler, moderator and void coefficients of reactivity respectively. T_f and T_m are fuel and moderator temperatures respectively and α is the void fraction.

Reactivity feedback effects combined with reactor SCRAM eventually bring down the reactor power. Therefore, the real RIA transient is represented by a power pulse rather than a runaway exponential power rise. Nevertheless, the time it takes to SCRAM the reactor is in the order of seconds whereas the RIA power pulse takes only tens of milliseconds to complete. Sometimes this leads to multiple power pulses preceding the total shutdown. Frequency and magnitude of consecutive pulses depend on the response time for reactivity feedback mechanisms. Undesired consequences of individual power pulse in commercial LWR can be separated into 4 stages [4]:

1. Almost adiabatic increase in fuel temperature results in a significant thermal expansion of uranium fuel. This leads to large mechanical loads on the fuel cladding with the potential of cladding failure. The cladding temperature remains relatively low during this phase
2. As the heat reaches the coolant, it can cause DNB. This could lead to cladding temperatures above 1000 K. Thermal expansion and extreme temperatures result in fragmentation of uranium oxide fuel which releases a vast amount of fission gasses increasing the pressure

inside the fuel cladding. Such buildup of pressure combined with thermally weakened cladding may result in cladding failure.
3. As the cladding undergoes quenching, there is a risk of brittle failure.
4. During the last stage, there is a risk of molten fuel dispersion through the damaged cladding. The molten fuel will immediately vaporize the water around it, which could potentially result in steam explosion.

Shape, amplitude and temporal width of the power pulse define the total energy release and the potential for the above mentioned failure mechanisms. Shape and width of the power pulse can be described analytically using Nordheim-Fuchs model.

$$\dot{Q}(t) = \dot{Q}_{max} \cdot \operatorname{sech}^2 \left[\frac{(\rho - \beta_e) \cdot (t - t_{max})}{2 \cdot \Lambda} \right] \tag{4}$$

where t_{max} is time when the maximum power $\dot{Q}_{max}$ is reached. β_e is an effective fraction of delayed neutrons and Λ is an effective neutron lifetime. The model assumes adiabatic temperature rise in fuel with a constant fuel temperature coefficient of reactivity. The Nordheim-Fuchs model predictions are in a good agreement with 3D kinetics codes [1]. The model captures a big fraction of energy released by the fuel whereas 3D kinetics codes also capture some additional energy attributed to delayed neutrons.

Such remarkable agreement between the analytical model and state-of-the-art computer codes illustrates a dominance of fuel Doppler effect compared to other reactivity feedbacks. While being true for commercial LWRs, certain research reactors (e.g. BR-2 in Belgium) that use highly enriched uranium have negligible Doppler effect. In such systems, typically operated at low or even ambient pressure, moderator and void effects become paramount and the thermal hydraulic behavior of the reactor governs the duration of the transient. The use of co-extruded metallic fuel in such reactors presents additional constrains on the fuel temperature. First, the metallic fuel can melt at lower temperature than ceramic fuel. Second, there is no gap between fuel and cladding. Therefore, rapid thermal expansion of metallic fuel exerts extreme stresses on the cladding.

1.2. Transient Heat Transfer

The complicated shape of the real power pulse depends on a large range of coupled parameters, e.g. fuel burnup, proximity of the ejected control rod, initial temperature and power level of the reactor. Integral effect tests on actual cores, e.g. SPERT and CABRI, have been performed in the past. However, while these studies were very informative, their conclusions cannot be generalized to any reactor. In particular, this kind of experiments could not be instrumented enough to gain a deep, universal understanding of transient heat transfer processes. That is the reason why, over the years, the focus has shifted from integral effect tests to separate effect experiments, consisting of simple, carefully controlled exponential power escalation with constant period (Eq. (1). Based on these studies it is now possible to have an understanding of differences between steady state and transient heat transfer processes and how these differences change with the rate of power rise (i.e. escalation period τ). Heat transfer between reactor cladding and coolant during exponentially escalating power transients can be divided in four parts:

1. Single phase heat transfer;
2. Nucleate boiling;
3. Transition boiling;
4. Film boiling.

The transition between single phase and boiling heat transfer regimes is called onset of nucleate boiling (ONB). Physically it is defined by the appearance of the first bubble on the boiling surface. Departure from nucleate boiling (DNB) indicates a critical point when the regime of nucleate boiling can no longer be sustained and a regime of transition boiling begins, as observed by Bessiron [5]. Heat flux at DNB is referred to as a critical heat flux (CHF). The transition boiling regime is generally unstable[1] and the boiling surface quickly switches to the film boiling regime. Although all of these regimes are extensively studied in steady state conditions, the knowledge about the effect of rapidly varying heat flux remains limited.

Boiling curves shown in Figure 1 highlight main differences between steady state and transient boiling. Note that sketches shown in Figure 1 are more representative of subcooled boiling. The main differences between steady and transient boiling curves are:

1. Single phase heat transfer coefficient (HTC) is higher for transient conditions and increases with decreasing power escalation periods.
2. Wall superheat at ONB is higher for transient boiling. In addition, the wall superheat decreases after ONB creating a distinct temperature "overshoot".
3. CHF is higher for transient boiling.
4. During the transition to film boiling a transient boiling curve can exhibit an extreme drop in heat flux [5]. Such behavior could be caused by the thermal inertia of the heating element (e.g. reactor fuel rod) and becomes more important for shorter escalation periods.

A more detailed description of the above mentioned mechanisms is described in following sections.

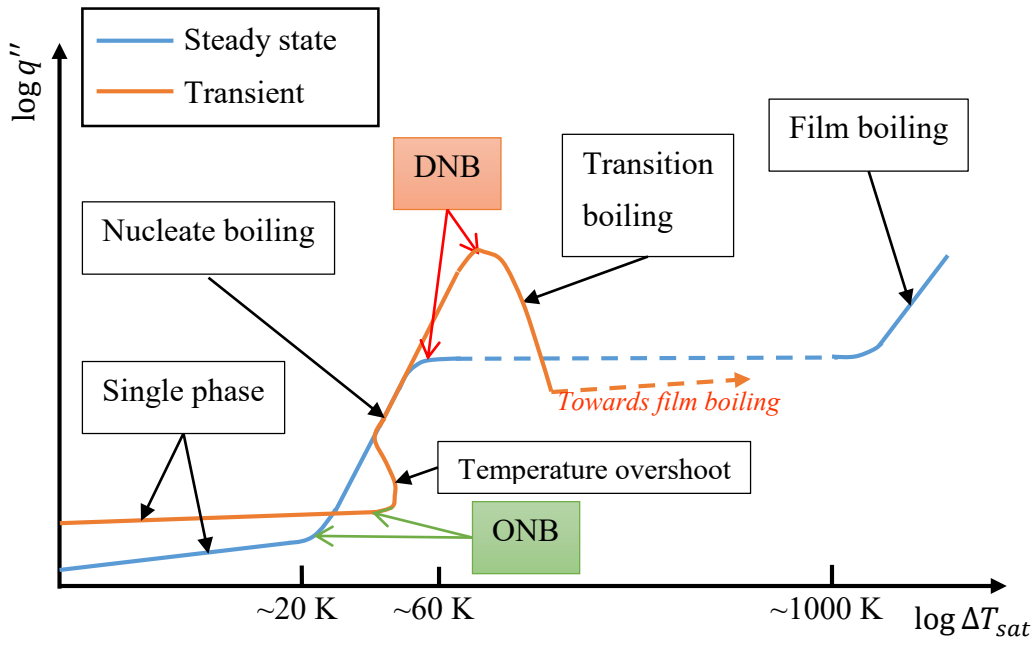

Figure 1. Sketch of boiling curves observed during steady state and transient boiling regimes

[1] Unless the wall temperature is controlled

1.3. Single Phase Heat Transfer

Multiple studies confirmed that a single phase heat transfer coefficient (HTC) during the transient can be characterized as a superposition of convection and transient conduction HTCs. Convection dominates when the power transient is relatively slow, whereas transient conduction governs the heat transfer process during short transients. In 1957, Rosenthal and Miller demonstrated the dominance of transient conduction in pool boiling experiments in a vertically oriented ribbon-shape heater [6]. Soliman and Johnson [7] extended the analysis of single-phase heat transfer by including the effect of flow. They used three different approaches to characterize their experimental database:

- The first approach, known as Slug flow model (introduced by P.L. Chambré), provides an analytical solution for energy conservation equation retaining conductive and advective terms. This model, however, assumes a uniform velocity distribution in the fluid. The model gave good results in cases with short power escalation periods and small velocities. Notably, it reduces to the pure transient conduction solution of Rosenthal and Miller [6] when the flow velocity is set to zero.
- The second approach extended the slug flow model by prescribing a turbulent flow velocity profile near the heater surface. This model was applicable to cases with large velocity and escalation periods.
- Both models break down in the intermediate range and a semi-empirical approach was used.

Other approaches included the correlation of experimental data by Kataoka et al. [8], as well as the use of time-scales analysis to correlate the steady state forced convection and the transient conduction heat transfer coefficients, as proposed by Su et al. [9].

1.4. Onset of Nucleate Boiling

Onset of nucleate boiling is of great importance for RIA analysis because it determines the appearance of the negative void reactivity feedback. The increase of the ONB temperature in transient conditions was demonstrated in the early study by Rosenthal and Miller [6]. Further studies showed that transient ONB is delayed compared to the steady state[8, 10, 11]. It was also observed that, when the boiling starts, it results in a rapid increase of the HTC which brings the wall temperature down. This phenomenon is called “temperature overshoot” and is illustrated in Figure 1.

Recently, Su et al. [12] demonstrated that the delay of ONB is dictated by the steepness of the temperature profile near the heated wall and can be predicted by a simple mechanistic model. According to the Hsu criterion, the bubble embryo cannot grow out of the nucleation cavity until the saturation temperature (corresponding to the vapor internal pressure) is reached or exceeded all around the bubble embryo and, in particular, at the tip. As temperature profiles tend to be stiffer for shorter periods, according to the Hsu criterion, the ONB wall superheat increases with decreasing power escalation periods. However, while Sakurai [13]and Johnson [10] speculated on a similar mechanism, a thorough, comprehensive experimental proof was lacking before the work of Su et al. [12].

Heterogeneous spontaneous nucleation as a mechanism for the ONB was postulated by Sakurai and was presented in multiple works. The summary of these studies is found in [11]. Sakurai argued that the heterogeneous spontaneous nucleation in a completely flooded cavity can occur at

superheats as low as 70 K. As described in [14], the heterogeneous nucleation temperature can be estimated by thermodynamic analysis of embryo in contact with the wall. The outcome of such analysis is the likelihood of the nucleation event described by the rate of embryo formation, *J*, as a function of fluid temperature. In 1977, Kottowsky developed an analytical expression for *J* as a function of fluid properties and geometrical parameters for heterogeneous nucleation in conical cavities [11]. Two geometrical parameters are present in the model of Kottowsky:

$$S = \frac{1}{2} \cdot \left[1 + \cos\left(\theta + \frac{\pi - \beta}{2}\right)\right] \tag{5}$$

$$f = \frac{1}{4} \cdot \left[2 + 3\cos\left(\theta + \frac{\pi - \beta}{2}\right) - \cos^3\left(\theta + \frac{\pi - \beta}{2}\right)\right] \tag{6}$$

where θ is solid-liquid contact angle and β is the aperture angle of the nucleation cavity. Sakurai argued that since average values of θ and β are not known the only way to determine them is by measuring the heterogeneous nucleation temperature experimentally and correlating Eqs. (5 and (6 with experimental data. By performing such experiment Sakurai developed the following correlations for a rate of embryo formation $J = 10^6$:

$$S = \exp\left[-21.6 \cdot \left(1 - 0.52 \cdot \exp(-60 \cdot Z) \cdot Z^{0.1} \cdot \frac{T_{cr} - T}{T_{cr}}\right)\right] \tag{7}$$

$$f = \frac{1}{4} \cdot [2 + 3(2S - 1) - (2S - 1)^3] \tag{8}$$

$$Z = \frac{\sigma_B \cdot T_{cr}}{T_{cr} - T_B} \tag{9}$$

where T_{cr} – critical temperature, T_B – saturation temperature at atmospheric pressure, σ_B – liquid surface tension at T_B. Using this approach, Sakurai reported a value of *S* for water in the order of 10^{-3} [11]. Table 1 illustrates possible values of contact angle θ and cavity aperture angle β for $S = 10^{-3}$ calculated from Eq. (5. It is clear that the homogeneous nucleation with $S = 10^{-3}$ is only possible on hydrophobic surfaces since values of contact angle θ smaller then 87° lead to negative values of β. However, commercial metallic surfaces are rarely hydrophobic. Additionally, to reach the homogeneous nucleation temperature the boiling surface has to be completely degassed – condition rarely achieved in the real-life application. Therefore, the heterogeneous nucleation ONB model is only useful for a narrow range of conditions.

Table 1. Combination of contact angle and cavity aperture angle for the value of geometrical parameter $S = 10^{-3}$

Solid-liquid contact angle θ	Aperture angle of a conical cavity β
87	1
90	7
120	67
150	127

1.5. Fully developed nucleate boiling

After the temperature overshoot, the transient boiling curve generally coincides with the steady state one (see Figure 2, adapted from Serizawa[15]). In some cases, the end of temperature overshoot phase happens at extremely high heat fluxes, higher than the steady state CHF. Still, such boiling curve usually approaches the extrapolation of the FDNB part of the steady state boiling curve before experiencing CHF (see Figure 2, A and B). For extremely fast transients the transient boiling curve experiences CHF before returning to the extension of the steady state FDNB curve (see Figure 2, C). Another type of boiling curve (type D) that is shown on Figure 2 is differentiated by a "loop" before CHF. While different periods or subcooling may result in different transient boiling curve types, optical observation showed no appreciable difference in FDNB behavior between steady state and transient cases [4, 7, 8]. The fully developed nucleate boiling regime during transient boiling can be approximated by the relation of the form

$$q'' = C \cdot (\Delta T_{sat})^a \tag{10}$$

where ΔT_{sat} is wall superheat; C and a are empirical constants. It should be noted that many saturated pool boiling curves measured by Sakurai [11] have no temperature overshoot and never

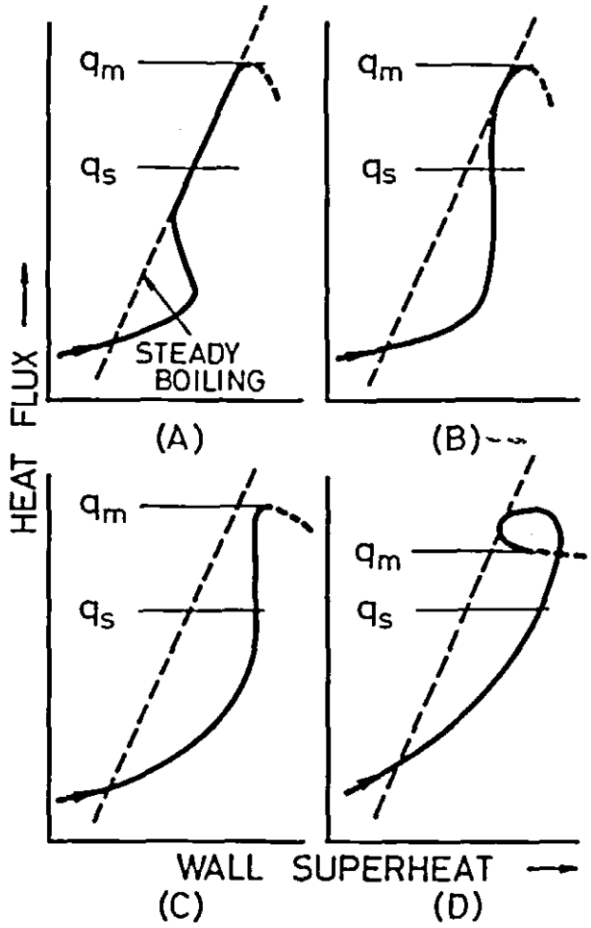

Figure 2. Different types of boiling curves observed during exponential transients. q_m represents transient CHF and q_s represents steady state CHF. Adapted from [15].

reach a FDNB regime. For such tests, points of ONB and CHF are practically the same. However, such observations are probably biased by the time-resolution of the available diagnostics [11] since any nucleation effect should result in a momentary rise in HTC even if it is followed by the immediate transition to film boiling.

1.6. Departure from nucleate boiling

A vast number of transient CHF experiments were performed in the past. Both pool and flow boiling regimes were explored. A general trend observed by multiple researchers is that CHF increases as escalation period decreases. In other words, faster transients have higher CHF values. Based on these observations a variety of mechanisms and correlations for the prediction of CHF in transient boiling were proposed. Selected models are presented below.

Sakurai [11] presented two distinct mechanisms for CHF in transient pool boiling. For long periods and low subcoolings the increase in transient CHF compared to the steady state was attributed to the time lag required for hydrodynamic instability to cause DNB. An empirical relation was developed for this regime:

$$q''_{c,tr} = q''_{c,ss} \cdot (1 + 0.21 \cdot \tau^{-0.5}) \tag{11}$$

where τ – power escalation period, $q''_{c,ss}$ – steady state CHF and $q''_{c,tr}$ is transient CHF. It was claimed that, in all other regimes, CHF is caused by spontaneous heterogeneous nucleation (HSN) in flooded cavities. When escalation period is long and subcooling is high, HSN should occur during the FDNB or partially developed boiling regime. Another empirical relation was developed for this range of conditions

$$q''_{c,tr} = q''_{c,ss} \cdot (1 + 0.023 \cdot \tau^{-0.7}) \tag{12}$$

Finally, in the case of short periods the points of CHF and ONB coincided with each other and a relation based on the heterogeneous nucleation model (briefly discussed in section 1.4) was developed

$$q''_{c,tr} = h_{com} \cdot (\Delta T_i(\tau) + \Delta T_{sub}) \tag{13}$$

where h_{com} is a combined HTC for transient conduction and convection, ΔT_i is the heterogeneous nucleation wall superheat (40-70 K depending on pressure [11]) and ΔT_{sub} is the liquid subcooling. It should be noted that ONB could be significantly delayed when heater cavities are free of entrapped gases, i.e. are completely flooded. In experiments of Sakurai, this effect was investigated by pressurizing the boiling vessel up to 5 MPa prior to the experiment. Then, the pressure was decreased back to the desired value and a transient boiling experiment was performed. Note that, after such procedure, the cavities in the boiling surface should be completely flooded. As shown by Sakurai, Eq. (13) only predicts data points that were taken at saturated conditions and short periods. In such conditions, the pre-pressurization procedure led to CHF happening immediately after ONB. Such behavior was explained by Sakurai with the heterogeneous spontaneous nucleation mechanisms. Although cavities with low heterogeneous nucleation superheat are rare (see Table 1) it only takes one of them to start boiling on the entire surface. In fact, at saturation or low superheat, bubbles can grow very large, e.g. with diameters as large as a few millimeters. So, once a bubble nucleates on a certain cavity, it covers the surrounding cavities with vapor, causing a cascade activation of originally flooded cavities. Additionally, if ONB is delayed, i.e. it happens at higher wall superheat, at the moment of nucleation more energy is stored in a thin superheated liquid layer close to the heater surface. These conditions promote a more rapid

evaporation of the liquid in contact with the boiling surface, which in turn results is a faster growth of the dry area surface. Thus, CHF happens almost immediately after the nucleation of the first, big bubble. However, when CHF was preceded by a nucleate boiling phase, i.e. with multiple bubble departure cycles, experimental CHF values were much higher than predictions made by using Eq. (13) [11]. Importantly, nucleate boiling on unflooded cavities (not HSN) is the expected nucleation mechanism because, at wall superheats below 100 K, HSN can only happen in a narrow range of cavity geometries (see Table 1). Thus, while it has been speculated that HSN is the CHF mechanism in such conditions, there is no clear experimental evidence to ultimately verify this claim.

The model of Serizawa [15] and the improvement proposed by Pasamehmetoglu et al. [16] explain the enhancement of transient CHF compared with the steady state by the evaporative thinning of a macrolayer trapped between the heater surface and a vapor patch that hovers above the boiling surface. They argued that during steady state CHF such layer is thinned hydrodynamically. However, in transient boiling the rate at which the hydrodynamic thinning proceeds is slower than the evaporation of the macrolayer, which is the dominant mechanism. Therefore, an energy balance was applied to the macrolayer in order to determine the time lag for the complete macrolayer evaporation. The heat flux at the moment of the complete macrolayer evaporation is the transient CHF. The final version of the model presented in [16] is summarized below:

$$\eta^{n+1} - \frac{1}{n \cdot B_s^2} \cdot \left[\frac{n \cdot \tau_c}{\tau} + n \cdot B_s^3 + B_s^2\right] \cdot \eta^n + \frac{B_s^n}{n} = 0 \tag{14}$$

$$B_s^{n+1} - \frac{2\tau_c}{\tau} \cdot B_s^{n-2} - 1 = 0 \tag{15}$$

$$\eta = \frac{q''_{c,tr}}{q''_{c,ss}} \tag{16}$$

where $q''_{c,ss}$ is the steady state CHF, $q''_{c,tr}$ is the transient CHF and τ is the power escalation period. The parameter $n \in [0; \infty]$ is the unknown that characterizes the liquid supply to the macrolayer during the process of thinning. When $n = 0$ the liquid supply is constant over the entire time of thinning. Such assumption was used in the model of Serizawa [15]. Conversely, when $n = \infty$ the liquid supply diminishes right at the beginning of the macrolayer thinning. No model was proposed for the value of *n*. In the work of Pasamehmetoglu et al. [16] $n = 2$. The parameter B_s can be calculated from Eq. (15) if the total time required to evaporate the macrolayer, τ_c, is known. This time is calculated from:

$$\tau_c = \left(\frac{q''_{c,ss,sat}}{q''_{c,ss}}\right)^3 \cdot \left(1 + K \cdot \frac{c_p \cdot \Delta T_{sub}}{h_{fg}}\right) \cdot \tau_d \tag{17}$$

where $q''_{c,ss,sat}$ – steady state CHF at saturated conditions, c_p – heat capacity of liquid, ΔT_{sub} – bulk subcooling, h_{fg} – latent heat of evaporation. The parameter K was set to 1 in the work of Pasamehmetoglu et al. [16]. The time scale τ_d represents a vapor patch hovering period and can be calculated by using the idealized bubble model presented by Haramura and Katto [17]

$$\tau_d = \left(\frac{3}{4\pi}\right)^{1/5} \cdot \left[\frac{4 \cdot \left(\frac{11}{16} \cdot \rho_l + \rho_v\right)}{g \cdot (\rho_l - \rho_v)}\right]^{3/5} \cdot v_1^{1/5}$$

where v_1 is the volumetric growth rate of the vapor patch given by

$$v_1 = \frac{\lambda_D^2 \cdot q''_{c,ss,sat}}{\rho_v \cdot h_{fg}}$$

where λ_D is the most dangerous Taylor instability wavelength

$$\lambda_D = \sqrt{3} \cdot 2\pi \cdot \sqrt{\frac{\sigma}{g \cdot (\rho_l - \rho_v)}}$$

where σ is liquid-vapor interfacial tension. It should be noted that the above model requires the establishment of a large vapor patch hovering over the heater surface. According to our experiments, such vapor structure might not form in highly subcooled boiling due to rapid re-condensation of the bubbles forming on the surface. Additionally, even at low subcoolings, very fast transients cannot be modeled by this mechanism, since the transition between the ONB and CHF is too fast for the hovering vapor mass to form.

Kataoka et al. [8] performed flow boiling experiments on the wire-shaped heater. Based on their data an empirical correlation was developed:

$$\frac{q''_{c,tr} - q''_{c,ss}}{G \cdot h_{fg}} = 0.2038 \cdot \left(\frac{\rho_v}{\rho_l}\right)^{0.52} \cdot \left(\frac{\sigma \cdot \rho_l}{G^2 \cdot l_0}\right)^{0.19} \cdot \left(\frac{\tau \cdot G}{\rho_l \cdot l_0}\right)^{-0.63}$$

where l_0 is the Laplace length.

In conclusion, the above discussion illustrates that CHF models proposed in the past do not cover all the physical mechanisms observed in transient conditions. The model of Serizawa [15] provides a compelling description of the physical behavior close to CHF, but is not applicable to a wide range of subcoolings and power escalation periods. In the current work, advanced diagnostics are used to achieve a deeper understanding of transient CHF phenomena and illustrate the physical mechanisms in view of new mechanistic models of transient CHF.

2. Experimental Apparatus and Methodology

Experiments were performed on a vertically oriented flat heater cooled by forced upward flow. Figure 3 illustrates the main components used in the experiment. An IRC806 high speed infrared (HSIR) camera was installed behind the heater. It was used to capture the temperature distribution on the boiling surface. IR videos were acquired with the temporal resolution of 2,500 frames per second (fps) and spatial resolution of 115 μm/pixel. A Phantom v.12.1 HSV camera was installed in front of the heater, and used to image the distribution of bubbles on the boiling surface. High speed videos were acquired with the temporal resolution of 20,000 fps and spatial resolution of 25 μm/pixel. Two Chroma 62050P-100-100 DC power supplies were connected in series. They were used to amplify the exponential curve generated by the Rigol DG1022U function generator FG-2 and apply a transient voltage to the heater with a prescribed rate of change. Another function generator, FG-1, was used to provide a 5 V synchronization signal to the HSV camera. At the beginning of each test, HSIR camera, HSDAS, FG-1 and FG-2 were initiated simultaneously by the 5 V triggering signal. Nevertheless, a controlled delay was introduced between the trigger and outputs of FG-1 and FG-2 in order to capture the beginning of the transient.

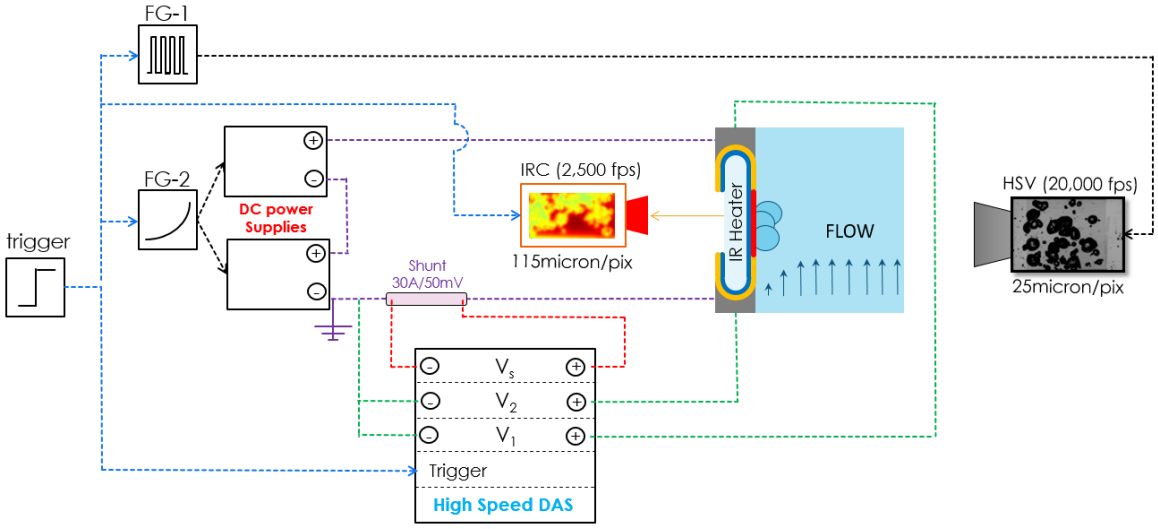

Figure 3. Schematics of the experimental setup

Voltage and current were measured with an Agilent U2542A high speed data acquisition system (HSDAS). Voltage drop across the electrical shunt of 1.67 mΩ calibrated resistance (V_s) was converted into current using Ohm's law. In order to precisely measure the voltage drop across the heater, a three-point measurement was performed. First, the voltage between positive electrode of the heater and ground was measured (V_1). The voltage between the negative electrode of the heater and the ground (V_2) was measured as well. With such arrangement the voltage drop across the heater was calculated as the difference between V_1 and V_2. Such approach allowed us to keep negative electrodes of V_1 and V_2 grounded, which significantly lowers the measurement noise. The shunt was located as close as possible to the negative electrode of the power supply, which automatically grounded the negative electrode of the DAS channel.

2.1. IR heater

Figure 4 shows the heater design. It consists of square sapphire substrate, 20x20 mm^2 , 1 mm thick. Indium tin oxide (ITO) coating is wrapped around the substrate and serves as a heater. The ITO coating is opaque in the 3-5 μm wavelength range and transparent in the visible light wavelengths. Sapphire is instead quasi-transparent in the 3-5 μm wavelength range. Such heater configuration allows an IR camera to image the radiation emitted by ITO, while simultaneously allowing a high-speed video camera to image the heater from the top with an LED back-lighting. The ITO is nano-smooth, with typical grain size in the order of 200 nm, with a thickness of 0.7 μm and a resistivity of 2.5 Ω/sq. Silver pads are deposited on top of the ITO and wrapped around the filleted edges of the sapphire substrate (see Figure 4). They define a square active ITO area of 10x10 mm^2 and allow a uniform supply of electric power to the heater surface.

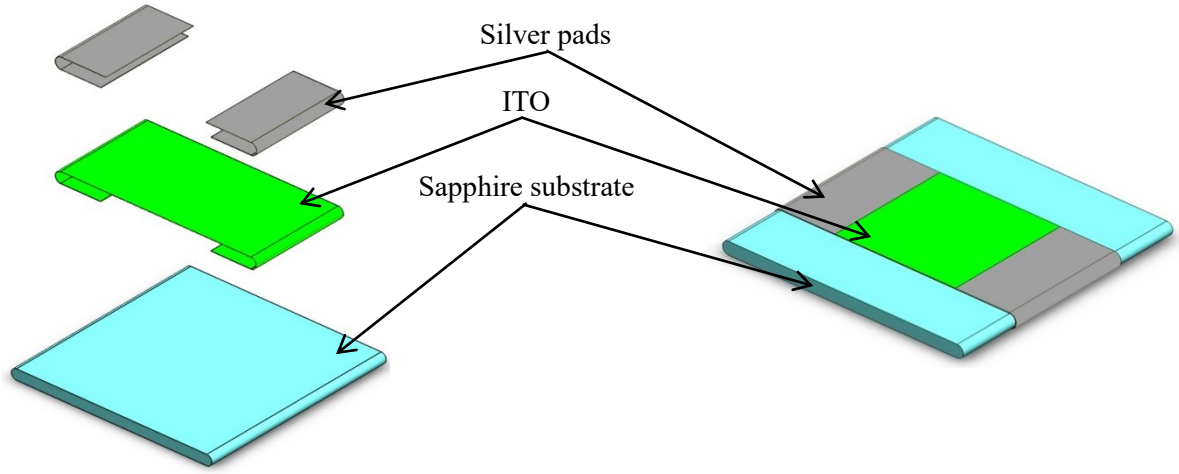

a) b)

Figure 4. Exploded (a) and assembled (b) views of the heater

Sapphire is quasi-transparent to infrared light and has high thermal conductivity and thermal capacity. Its high thermal effusivity leads to a large fraction of the total heat flux deposited in the ITO film to be directed to the sapphire instead of water, especially before the water starts to boil. As will be shown in section 2.4, due to these properties, a complicated post-processing algorithm needs to be used in order to reconstruct exact values of time-dependent temperature and heat flux distributions on the boiling surface. Despite this downside, sapphire is the only material that can provide sufficient structural strength together with a good level of IR transparency and affordable price.

Reaching CHF during exponential power escalation leads to very high surface temperatures (as high as 300 °C). At the same time, due to the transient nature of the tests, most of the substrate remains at the initial bulk temperature of the water, which can be as low as 25 °C. This introduces significant thermal stress across the substrate. Before the beginning of the experimental campaign several simple simulations were performed in order to predict whether the substrate can withstand the occurrence of the CHF during an exponential power rise followed by a power coast down. Details of these simulations are presented in Appendix A.

Several CHF values between 1 and 30 MW/m^2 were assumed in our analysis. Heat transfer coefficients during single-phase and nucleate boiling regimes were adopted from the previous study [9]. Results are presented in TablesTable 2 andTable 3 for tests at 75 K and 10 K of subcooling, respectively. It was assumed that the power coast-down is an exponential decay with the same period as the power rise. A conservative assumption was made that CHF occurs at the peak value of the escalation and the vapor film stays on the heater surface for the entire coast down. Experimental conditions marked as "GOOD" should not result in substrate cracking. Note that the total heat flux delivered to the ITO film, rather than the fraction that goes to water, is shown in Table 2 and Table 3,. Also note that among all tests shown in Chapter 3 the maximum achieved heat flux was slightly higher than 30 MW/m^2. There was no damage to the sapphire substrate during these tests, which illustrates the level of conservatism in this analysis. Nevertheless, if higher heat fluxes are needed in future studies, a more detailed and accurate analysis should be performed in order to ensure structural integrity of IR heaters.

Table 2. Results of substrate structural integrity analysis for 75 K subcooling

	Power escalation periods, ms					
Assumed value of CHF, MW/m^2	5	10	50	100	200	500
1	Single-Phase	Single-Phase	Single-Phase	Single-Phase	Single-Phase	GOOD
2	Single-Phase	Single-Phase	Single-Phase	Single-Phase	GOOD	GOOD
5	Single-Phase	Single-Phase	GOOD	GOOD	GOOD	GOOD
10	Single-Phase	GOOD	GOOD	GOOD	GOOD	GOOD
15	GOOD	GOOD	GOOD	Risk of Thermal Shock	Risk of Thermal Shock	Risk of Thermal Shock
20	GOOD	GOOD	Risk of Thermal Shock	Risk of Thermal Shock	Risk of Thermal Shock	Risk of Thermal Shock
25	GOOD	Risk of Thermal Shock	Risk of Thermal Shock	Risk of Thermal Shock	Risk of Thermal Shock	Risk of Thermal Shock
30	Risk of Thermal Shock	Risk of Thermal Shock	Risk of Thermal Shock	Risk of Thermal Shock	Risk of Thermal Shock	Risk of Thermal Shock

Table 3. Results of substrate structural integrity analysis for 10 K subcooling

	Power escalation periods, ms					
Assumed value of CHF, MW/m^2	5	10	50	100	200	500
1	Single-Phase	Single-Phase	Single-Phase	GOOD	GOOD	GOOD
2	Single-Phase	Single-Phase	GOOD	GOOD	GOOD	GOOD
5	Single-Phase	GOOD	GOOD	GOOD	GOOD	GOOD
10	GOOD	GOOD	GOOD	GOOD	GOOD	GOOD
15	GOOD	GOOD	GOOD	Risk of Thermal Shock	Risk of Thermal Shock	Risk of Thermal Shock
20	GOOD	GOOD	Risk of Thermal Shock	Risk of Thermal Shock	Risk of Thermal Shock	Risk of Thermal Shock
25	GOOD	Risk of Thermal Shock	Risk of Thermal Shock	Risk of Thermal Shock	Risk of Thermal Shock	Risk of Thermal Shock
30	Risk of Thermal Shock	Risk of Thermal Shock	Risk of Thermal Shock	Risk of Thermal Shock	Risk of Thermal Shock	Risk of Thermal Shock

2.2. Test Section

Figure 1 shows the test section, which is made of 316 stainless steel. It has three openings to accommodate quartz windows and one opening for the installation of the heater cartridge. Both windows and the heater cartridge are held in place by stainless steel flanges. PolyTetraFluoroEthylene (PTFE, also known as Teflon®) gaskets allow for the uniform distribution of a force upon tightening. Silicone O-rings are used to create a pressure boundary between the windows and test section body. The test section is designed to operate at pressures up to 10 bar and temperatures up to 180 ºC. The flow channel has a rectangular cross section (3×1 cm^2) with a hydraulic diameter D_h of 1.5 cm. The entrance channel has the same cross section as the test section. The length of the entrance channel is 965 mm, i.e. roughly 65 hydraulic diameters, which ensures a fully developed momentum boundary layer before the heating section. Table 4 presents the range of possible operating conditions for the test section.

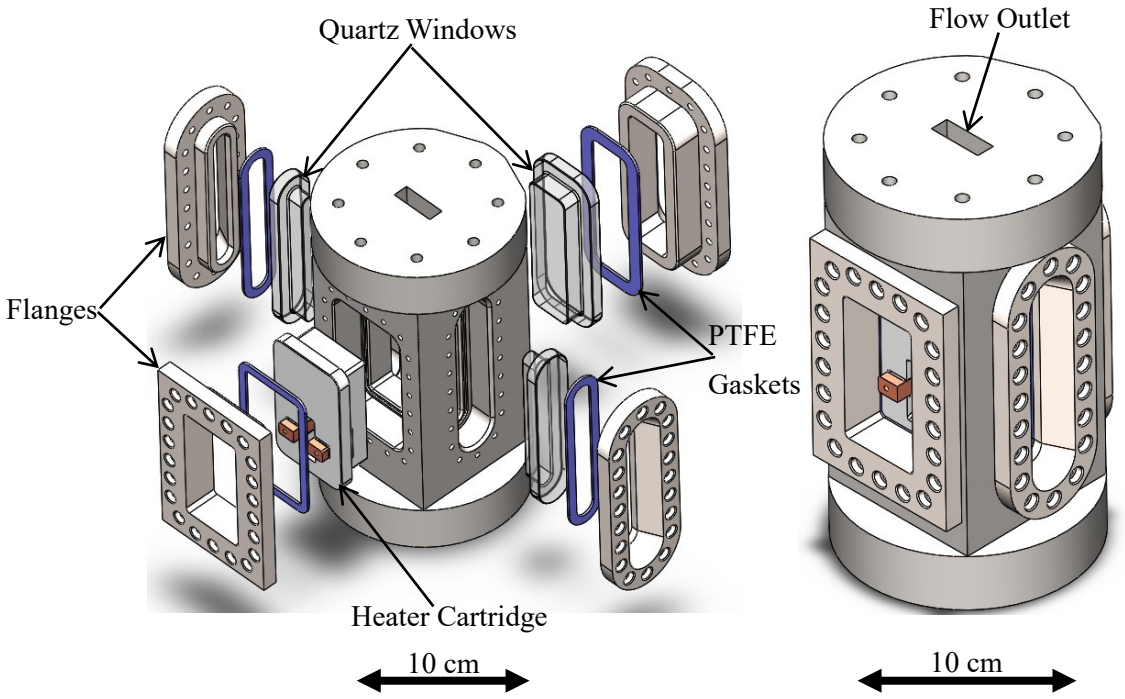

Figure 5. Test section design. Exploded (left) and assembled (right) views

Table 4. Test section operating conditions

Parameters	Range
Pressure, P	ambient to 10 bar
Temperature, T	ambient to saturation
Mass Flux, G	0 – 2500 kg/m^{2}s
Reynolds Number, $Re = \frac{G \cdot D_h}{\mu}$, here μ – fluid viscosity, Pa·s	0 – 250,000
Hydraulic Diameter, D_h	1.5 cm
Boiling Number, $Bo = \frac{q''}{h_{fg} \cdot G}$ (for 2500 kg/m^{2}s) here h_{fg} – latent heat of evaporation, J/kg	0 – 0.018
Heat flux, q''	0 – 100 MW/m^2

Parameters	Range
Prandtl Number, $Pr = \frac{\nu}{\alpha}$, here ν – kinematic viscosity, m^2/s; α – thermal diffusivity, m^2/s	0.98 – 6.13
Equilibrium Quality, x_e	-0.326 – 0
Subcooling, ΔT_{sub}	0 – 155 K depending on pressure

Figure 6 shows the arrangement of the heater cartridge. The body of the cartridge is made of Shapal™. Stainless steel side clamps push the heater to create a seal between the cartridge body and the heater. Such a design allows for a quick replacement of the heater if required. Copper leads are connected from behind and are used to supply electrical power to the heater. However, aluminum (or copper) tape has been used as it provides equally reliable electrical contact and flexibility without degrading the silver pads of the heater. The use of clamps and O-ring for the heater installation provides the degrees of freedom required to accommodate the thermal expansion of the heater substrate, and reduces the risk of thermal shock. Arrangement of mirrors is shown on Figure 7. Black arrows show the direction of the visible light as it is reflected from mirrors and sent to the HSV camera lens. LED light is used as back lighting from the side opposite to the mirror. As shown in the same Figure, the IR radiation emitted by the ITO-sapphire heater (red arrows) is reflected to the IR camera by a hot mirror.

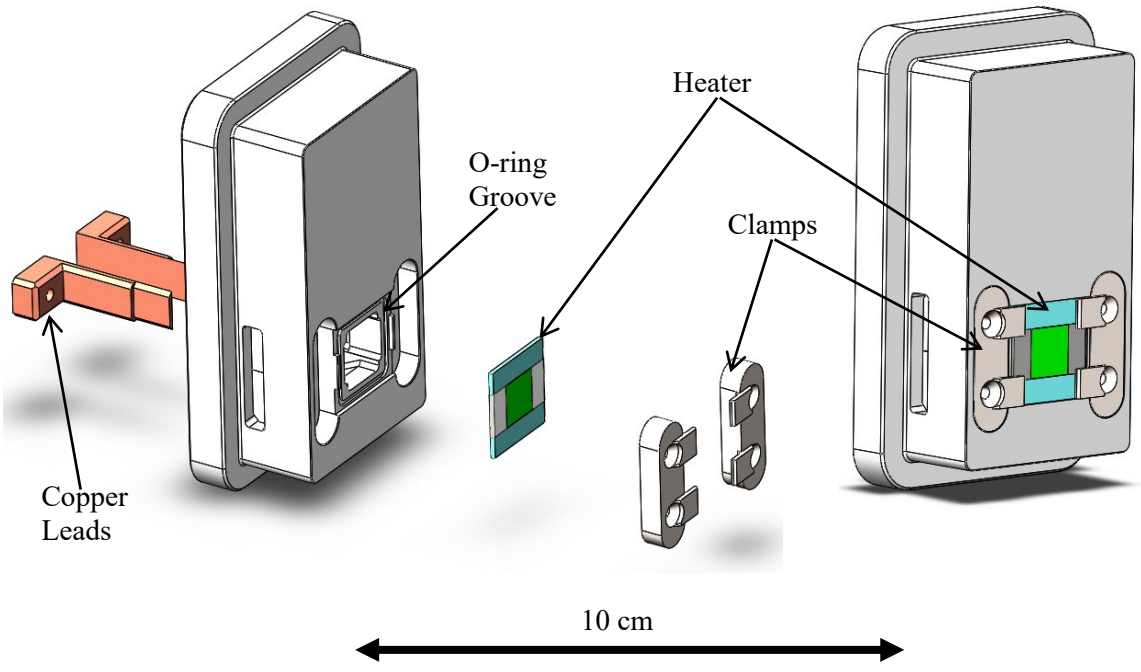

Figure 6. Exploded (left) and assembled (right) views of the heater cartridge

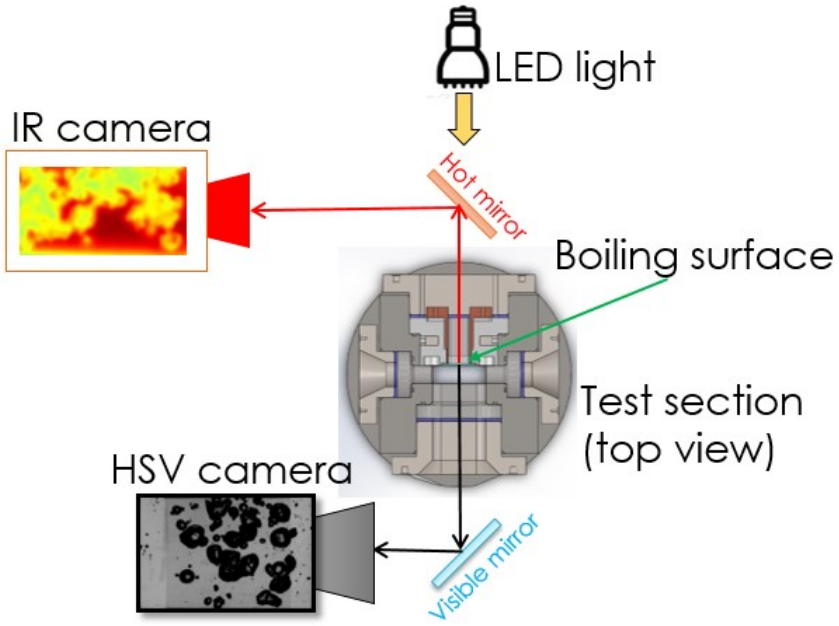

Figure 7. Optical arrangement

2.3. Flow Loop

The test section and entrance region were installed in a specially designed frame (Figure 8). The frame is equipped with an optical table and opto-mechanical components to enable a precise alignment of cameras and mirrors. The entire frame is standing on levelling casters with wheels which allow connection, disconnection and motion of the test section without any alteration to the optical setup. A similar frame was built for the flow loop itself, making the entire facility completely mobile. The diagram of the flow loop is shown on Figure 9. It is equipped with variable frequency pump, flow meter, temperature and pressure instrumentation, preheater, flow channel with the test section, heat exchanger, accumulator, filtering/degassing system and a fill and drain tank.

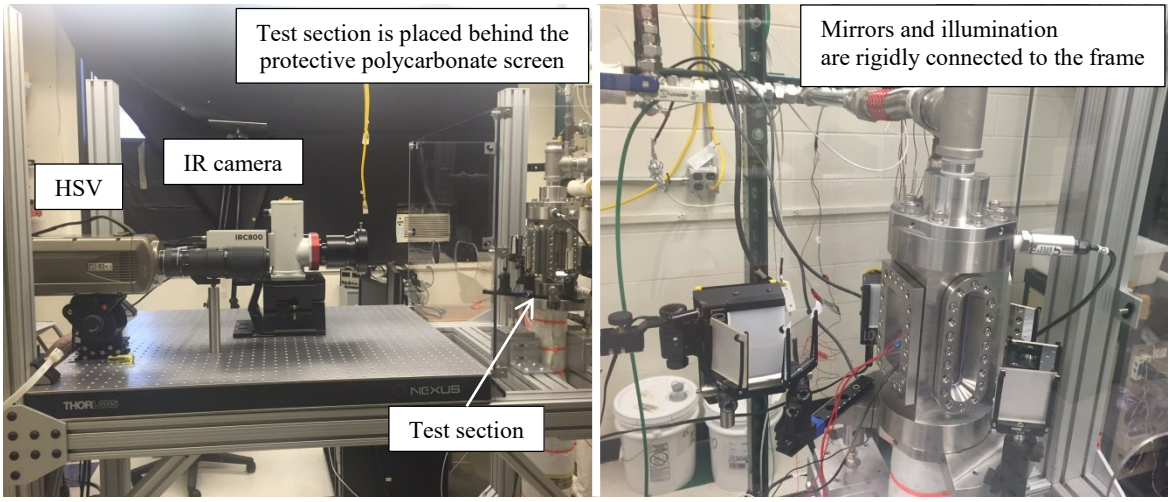

Figure 8. Pictures of the test section connected to the flow loop

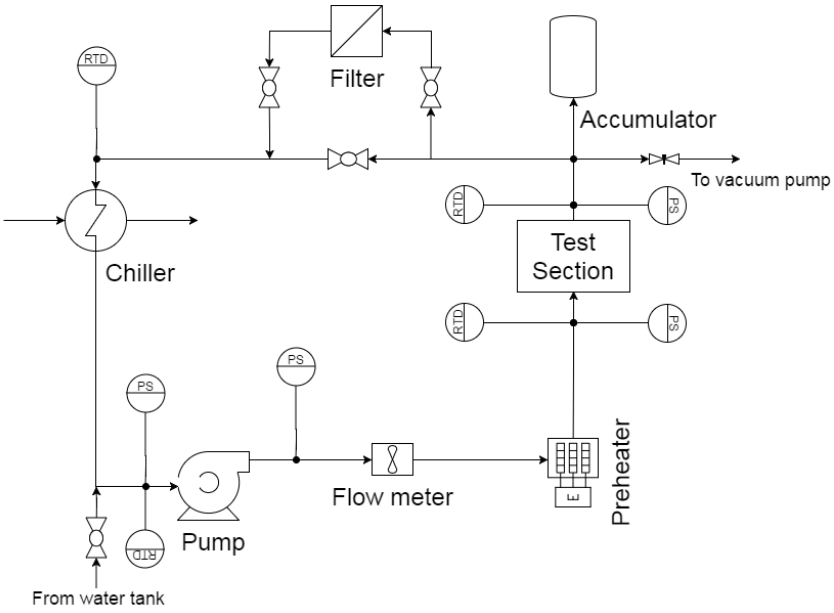

Figure 9. Flow loop diagram

2.4. Infrared Camera Calibration

A brief description of the IR calibration technique is presented below. For more details the reader can refer to [18]. The temperature of the ITO is proportional to the IR radiation it emits. However, in addition to the IR radiation from ITO, the IR camera also receives the radiation from the sapphire substrate (which is not completely transparent in the 3-5 μm wavelength range and whose optical properties are strongly wavelength dependent) and the radiation reflected from the background, as sketched in Figure 10. Therefore, it is important to exclude contributions from the sapphire and background radiations from the total signal in order to measure the actual ITO temperature[2]. This goal is achieved by solving an inverse problem coupling optical radiation and conduction heat

[2] Note that the ITO is very thin. Its thermal resistance and thermal capacity can be neglected. So, the ITO temperature coincides with the temperature on the actual boiling surface.

transfer. The problem is inverse because the boundary condition of the problem, i.e. the actual ITO temperature, is not known but is part of the solution, which is obtained iteratively. A guess ITO temperature is used as tentative boundary condition for the 3D conduction equation, which is solved in the sapphire substrate. The updated temperature distribution in the substrate is used to calculate the radiation emitted and reflected by the whole heater and received by the camera. This radiation is compared to the actual radiation detected by the IR camera. If these two radiations are not exactly the same, the guess ITO temperature is updated and the process is repeated until satisfactory convergence is achieved. Such procedure is applied to each IR frame throughout the transient.

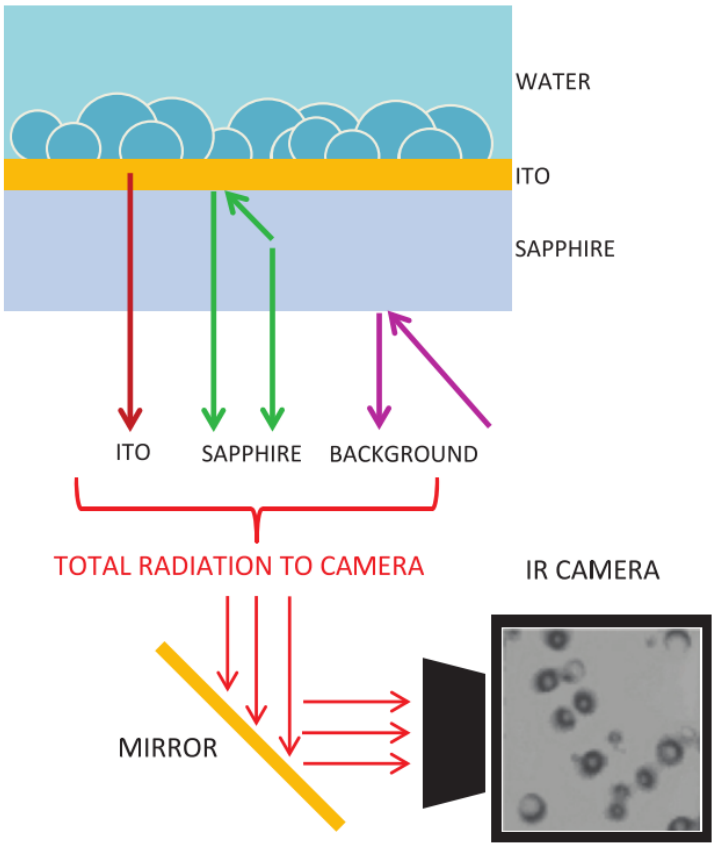

Figure 10. Different contributions of the total radiation measured by IR camera

2.5. Experimental procedures

The following experimental procedures were implemented during the experimental campaign:

1. In the beginning of each experimental day a steady state boiling was induced on the heater surface and maintained for approximately 30 minutes. This procedure is necessary to remove non-condensable gases from nucleation cavities.
2. Desired operating conditions (pressure, subcooling and mass flux) were established.
3. The exponential power curve with certain period and peak value was programmed in the function generator FG-2 (see Figure 3).
4. HSV and HSIR cameras as well as the HSDAS were pre-triggered.
5. Master-trigger was actuated.

6. Recorded IR video was examined. If the CHF was not achieved, steps 2-6 were repeated with a larger peak value of exponential curve.

2.6. Test Matrix

The test matrix for the current study is shown in Table 5. It is divided into three parts:

- The main test matrix represents the bulk of the collected data. It includes 3 Reynolds numbers, 4 subcoolings and 7 power escalation periods. Each test in the main test matrix was repeated three times to provide better statistical significance for CHF values.
- In additional 4 tests the coast down of exponential curve was set to the same period as escalation. These tests were used to explore the possibility of CHF happening during the coast down of the power pulse.

The following chapter presents main findings of the study.

Table 5. Test matrix

Main test matrix	
Parameter	**Range**
Reynolds number	As low as possible; 25,000; 35,000
Subcooling, K	75; 50; 25; 10
Power escalation periods, ms	5; 10; 20; 50; 100; 200; 500
Pressures, bar	1
Number of repetitions	3
Exploratory tests with long coast down	
Parameter	**Range**
Reynolds number	35,000
Subcooling, K	75
Power escalation periods, ms	5, 10, 20, 50
Pressures, bar	1
Number of repetitions	1

3. Results and Discussion

It is challenging to clearly define CHF for transient boiling. In our experiments we defined CHF as the value of heat flux that creates the first irreversible dry spot on the boiling surface. An irreversible dry spot is such that it never gets rewetted once it appears on the boiling surface unless the applied heat flux is decreased. Generally, there is no stable state for such a dry spot; it can only grow, if the heat flux keeps growing, or shrink and be quenched, if the heat flux decreases. Figure 11 supports this statement. It shows several frames of heat flux distributions of for a test, starting from the appearance of the first few bubbles (283.7 ms) and ending with the whole heater surface covered by the vapor film. A dry spot is clearly seen on the second snapshot (299.7 ms), with an extended area where the heat flux is very close to zero. However, this dry spot is eventually quenched, which means that it is a reversible dry spot (304.9 ms). While the quenching proceeds, two new dry spots are formed on the top and the bottom of the heater (304.9 ms). These dry spots are irreversible because they continue to grow (306.5 ms). Eventually they coalesce (308.9 ms) and a combined dry spot continues to grow until a vapor film covers the whole heater area (331.3 ms).

The values of CHF as well as the physics of the dry spot formation were influenced by subcooling, Reynolds number and escalation period. Each effect is described in greater detail below.

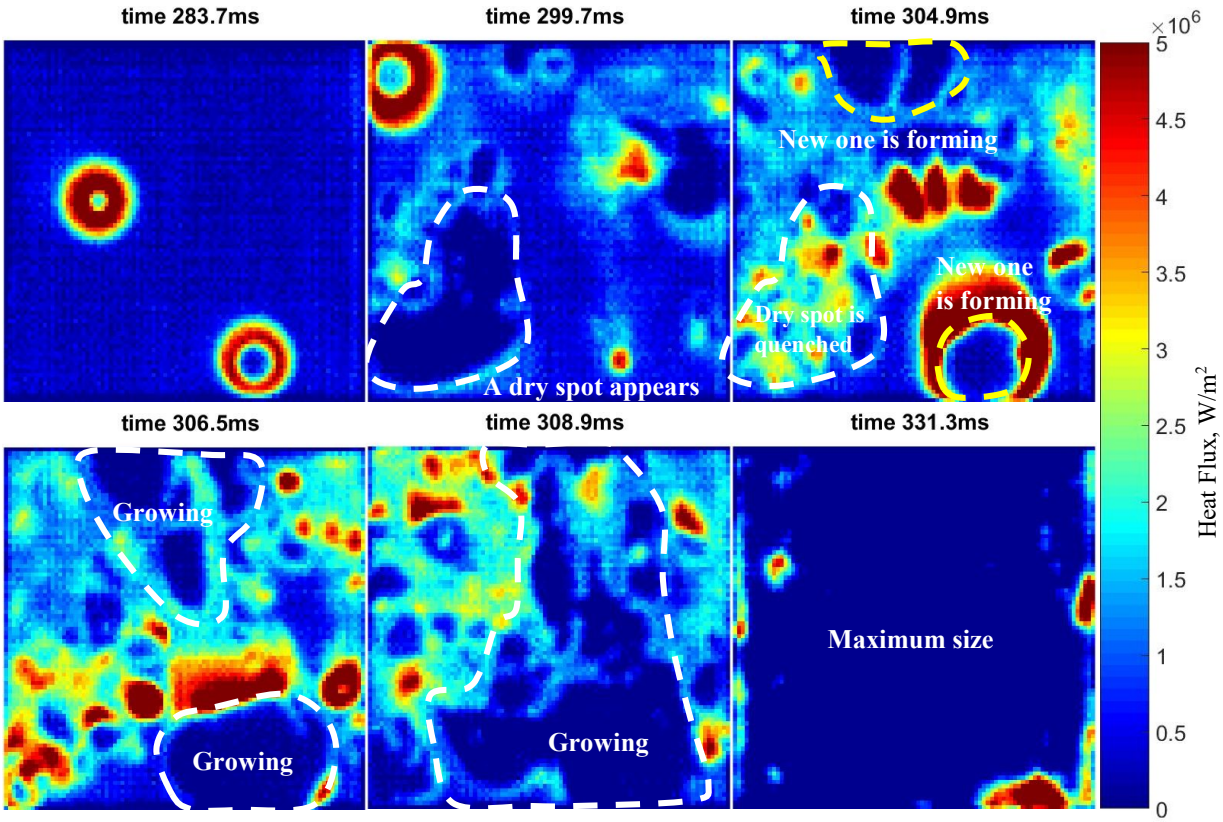

Figure 11. Escalation to CHF in a the test at
10 K of subcooling, 16,000 Reynolds number and 50 ms power escalation period

3.1. Influence of the Reynolds number

Figure 12 shows the influence of Reynolds number on CHF at 5 and 500 ms periods. For a very short escalation period (left figure), CHF is nearly independent on the Reynolds number (within the range of Reynolds numbers explored here). We speculate that a dependence might appear if the Reynolds number is increased further. As expected, the CHF dependence on the Reynolds number is more pronounced for long periods (right figure). These trends can also be observed in the boiling curves shown in Figure 13. An interesting flow effect was observed at 75 K subcooling, at all periods. In this regime, the presence of flow makes the dry spots to be shaped as elongated patches, aligned with the flow direction (Figure 14 a). Conversely, in the absence of flow, the dry spots had a random shape (Figure 14 b). The distance between such patches and their width could be related to the turbulent structure of the boundary layer. However, clear conclusions regarding such relation have not been drawn yet.

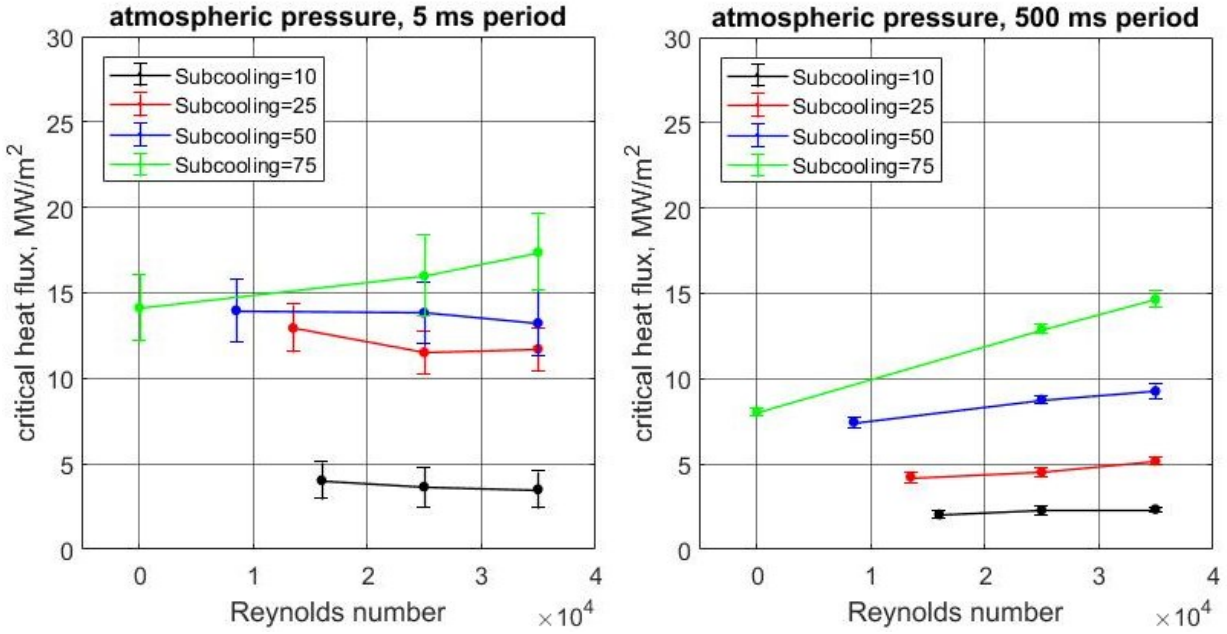

a) b)

Figure 12. CHF values for 5 ms (a) and 500 ms (b) periods

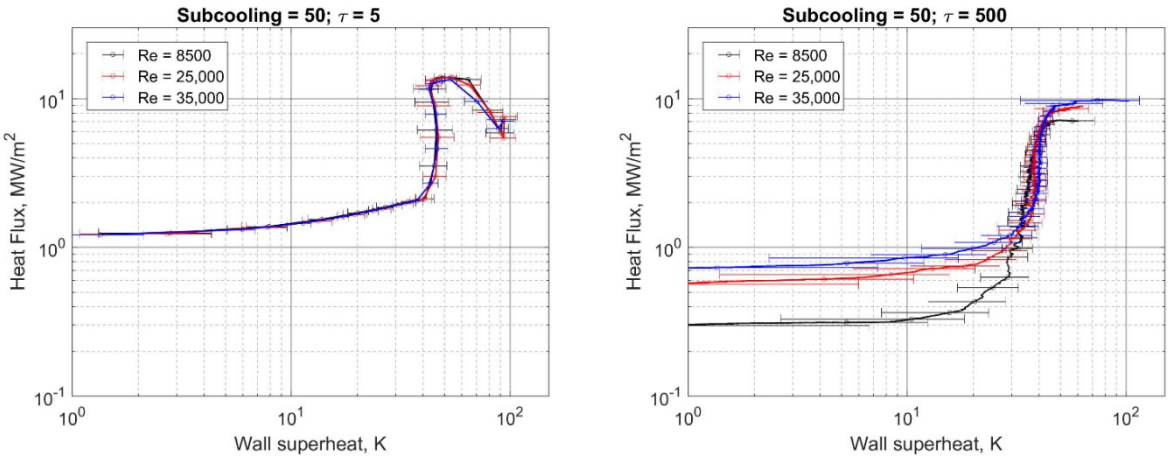

a) b)

Figure 13. Boiling curves for 5 (a) and 500 (b) ms periods. Subcooling is 50 K

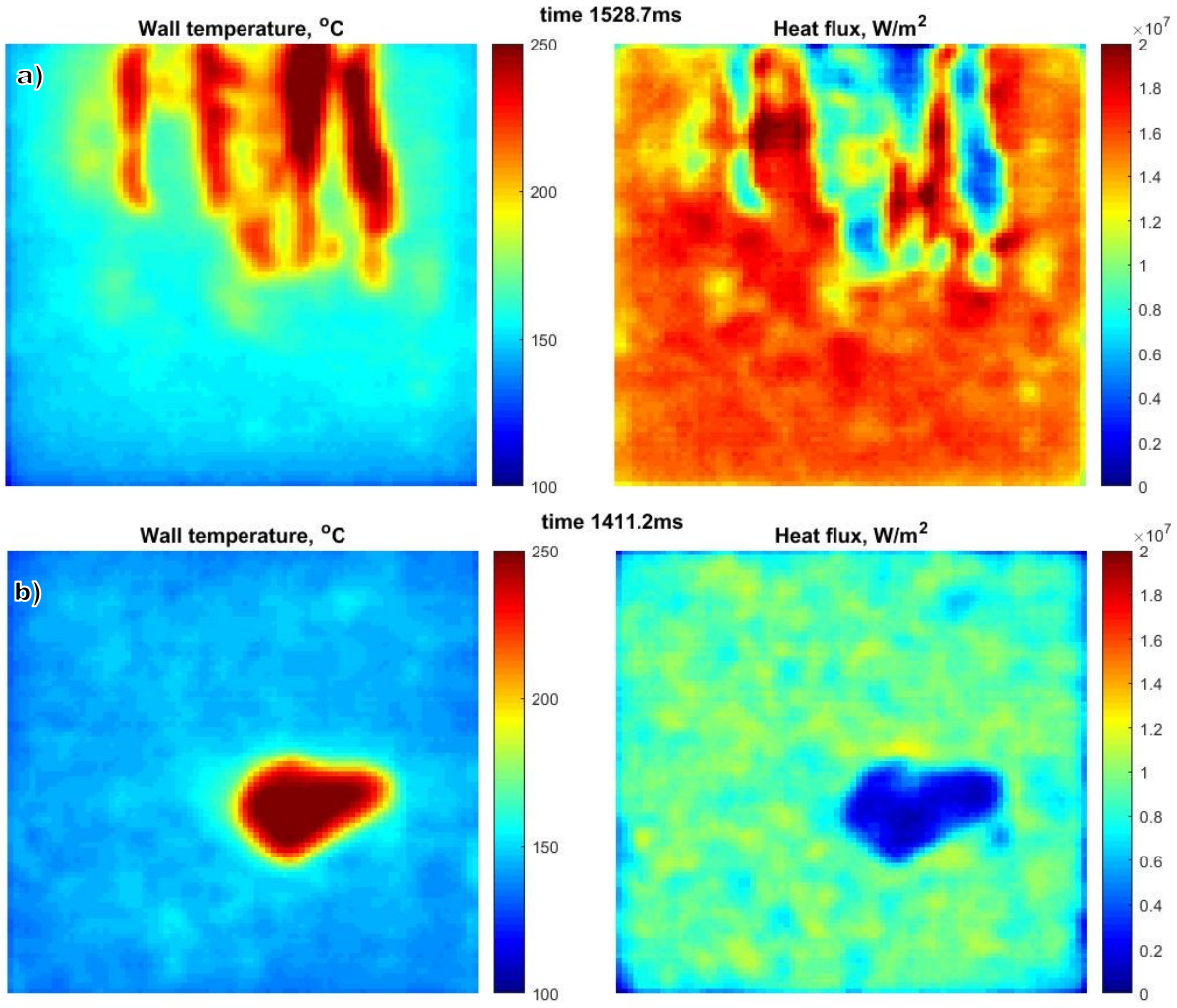

Figure 14. Dry spot shape for Re = 35,000 (a, top figures) and Re = 0 (b, bottom figures). Subcooling is 75 K. Period is 200 ms

3.2. Influence of the power escalation period

Figure 15 shows the dependence of CHF on the escalation period. It was found that CHF is almost independent of the escalation period for values larger than 100 ms. Note that data points taken in the absence of forced flow (Figure 15 left, Re = 0) follow the same asymptotic behavior as cases with high Reynolds numbers. It is most likely caused by the development of a stable natural circulation flow at long periods. For shorter periods, the CHF increases substantially as the period decreases. Escalation period has a significant effect on irreversible dry spots formation. At long periods dry spots are localized as they tend to form at certain locations (Figure 16 a). Specifically, dry spots are usually observed in the upper part of the heater which has lower local subcooling and higher local void fraction. On the other hand, at short periods the heat flux is increasing so fast that all the active area of the heater is susceptible to irreversible dry spot formation, as the temperature and heat flux distribution on the heater surface are quite uniform, with minimal effect of the flow. Eventually, multiple dry spots are formed all over the heater surface, which combined with a rapidly growing heat flux accelerates the net dry area growth (Figure 16 b).

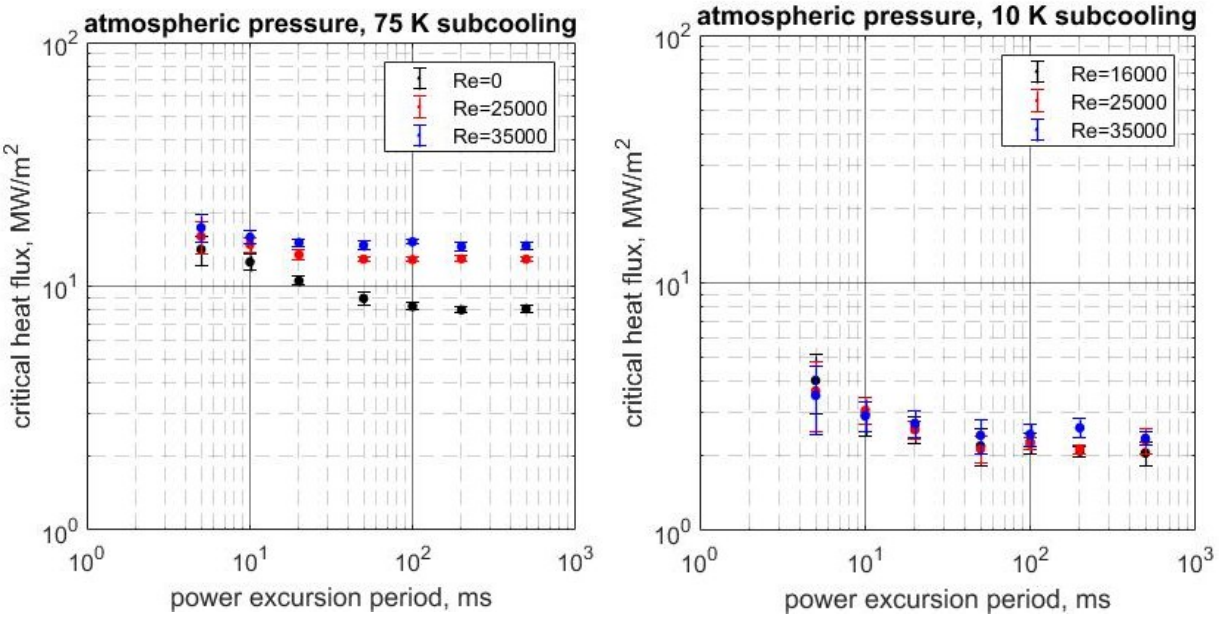

a) b)

Figure 15. CHF values for 75 K (a) and 10 K (b) subcoolings

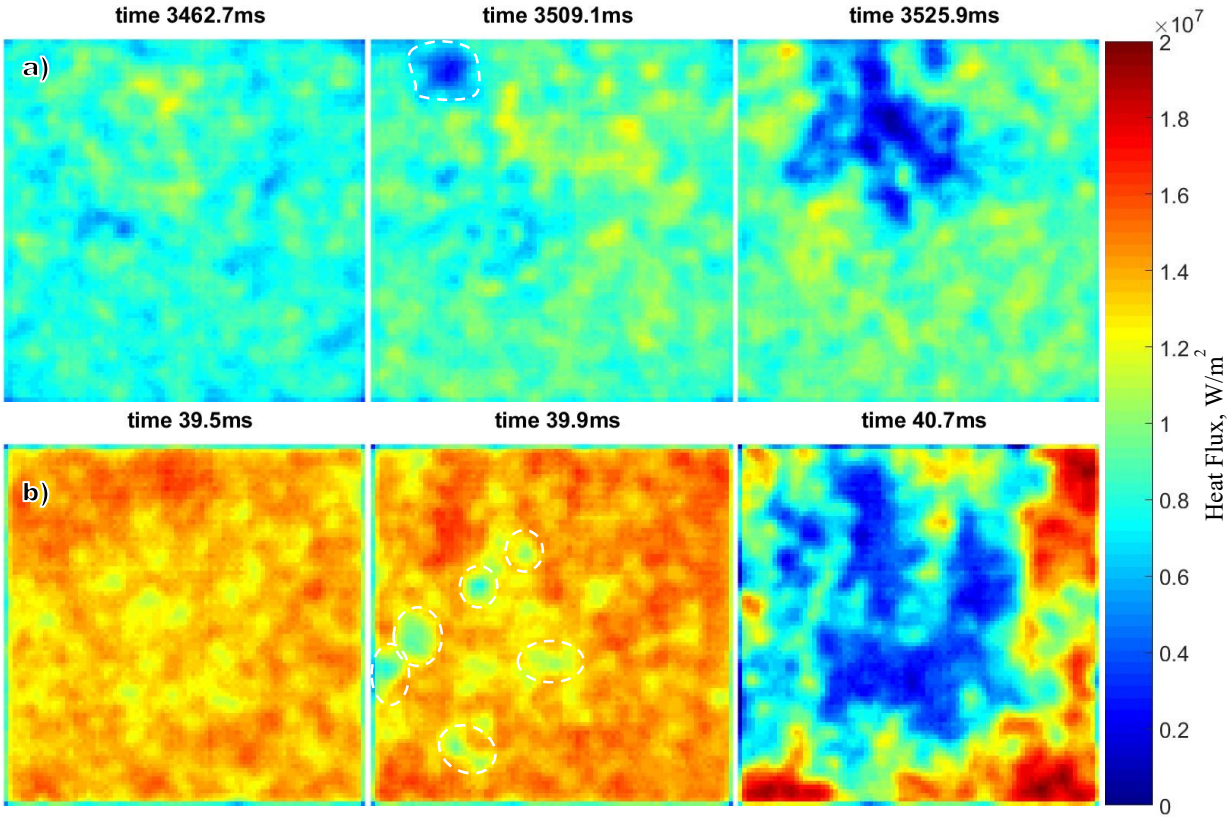

Figure 16. Progression of CHF for τ = 500 ms (a, top figures) and τ = 5 ms (b, bottom figures). Initial dry spots are outlined. Subcooling is 50 K; Reynolds number is 25,000

3.3. Influence of the subcooling

For long periods, subcooling has a similar effect on CHF as it would have in the steady state boiling. Highly subcooled flow enhances single phase heat transfer mechanisms such as forced convection and transient conduction. This delays both the ONB and CHF because more heat can be removed for each bubble life cycle. Additionally, subcooling reduces the thickness of the superheated liquid layer. This results in a rapid condensation of nucleating bubbles, preventing them from growing to large diameters and coalescing. This allows areas with small nucleation cavities to reach a sufficient ONB superheat without being suppressed by big bubbles. Finally, this leads to a much larger nucleation site density resulting in multiple small bubbles covering the boiling surface. Overall, such conditions make it much harder for the dry spot to form, leading to high values of CHF. The difference in bubble size between high and low subcooling is shown in Figure 17. Note that both images correspond to a 1x1 cm^2 area.

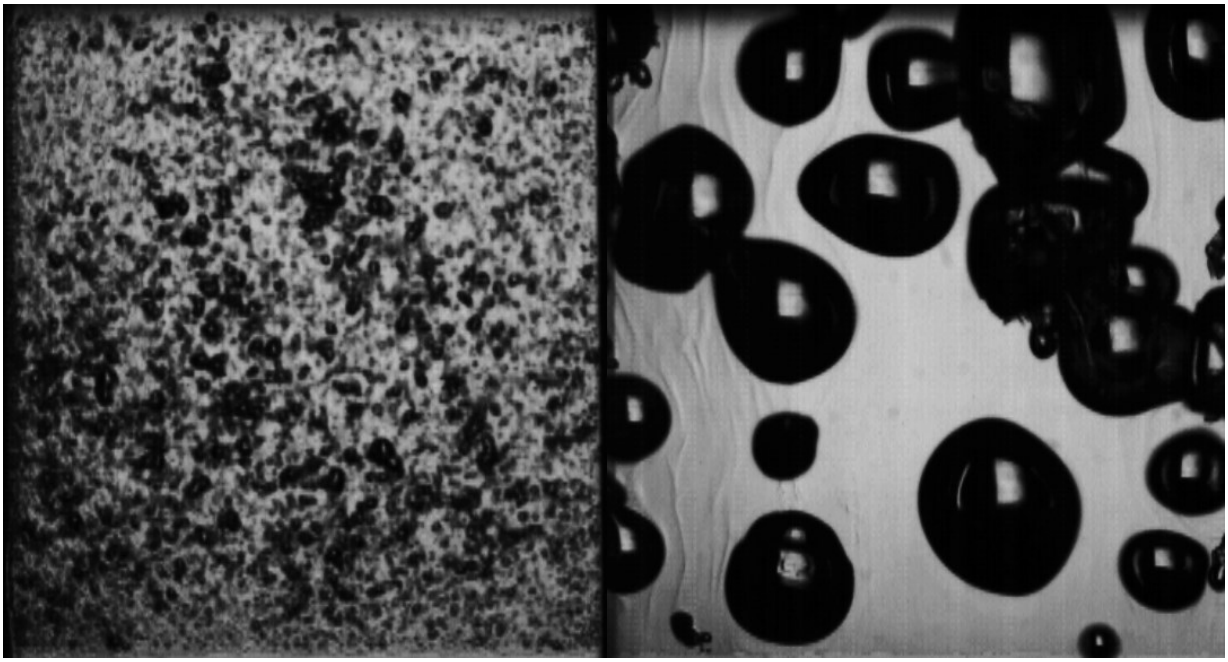

a) b)

Figure 17. Visualization of the boiling process for 75 K (a) and 10 K (b) subcoolings

Figure 18 shows the variation of CHF with subcooling. For periods larger than 20 ms CHF is a linear function of the subcooling. It increases with the subcooling, which supports the above discussion. However, at short periods a change of slope is observed when the curve is passing through 25 K subcooling. We found that the CHF mechanism is different for low subcoolings and short periods. At those conditions bubbles are growing so fast that they coalesce immediately, interrupting the liquid supply to the boiling surface. Therefore, the first generation of bubbles forms irreversible dry spots as their microlayers are fully evaporated. In other words, this means that heat fluxes at ONB and CHF are very close, and only differ due to the time lag between the nucleation and the complete growth (including microlayer evaporation) of the bubble footprint on the heated surface. Such behavior results in a sharp drop in CHF between 25 and 10 K subcooling. Figure 19 illustrates the process by showing heat flux distributions and HSV visualization side by side. Similar ONB to CHF transition also occurs at 25 K subcooling (Figure 20). However, the dry spot that is formed right after the ONB (Figure 20, 40.0 ms) is then quenched (42 ms) before the real CHF occurs. A posteriori, such behavior can be observed by examining boiling curves for 25 K subcooling (Figure 21). These boiling curves show a reversible “boiling crisis”, followed by rapid quenching and final CHF. Because the dry spot created during the first localized “boiling crisis” is almost entirely quenched, only the second dry spot was identified as a real CHF for 25 K subcooling.

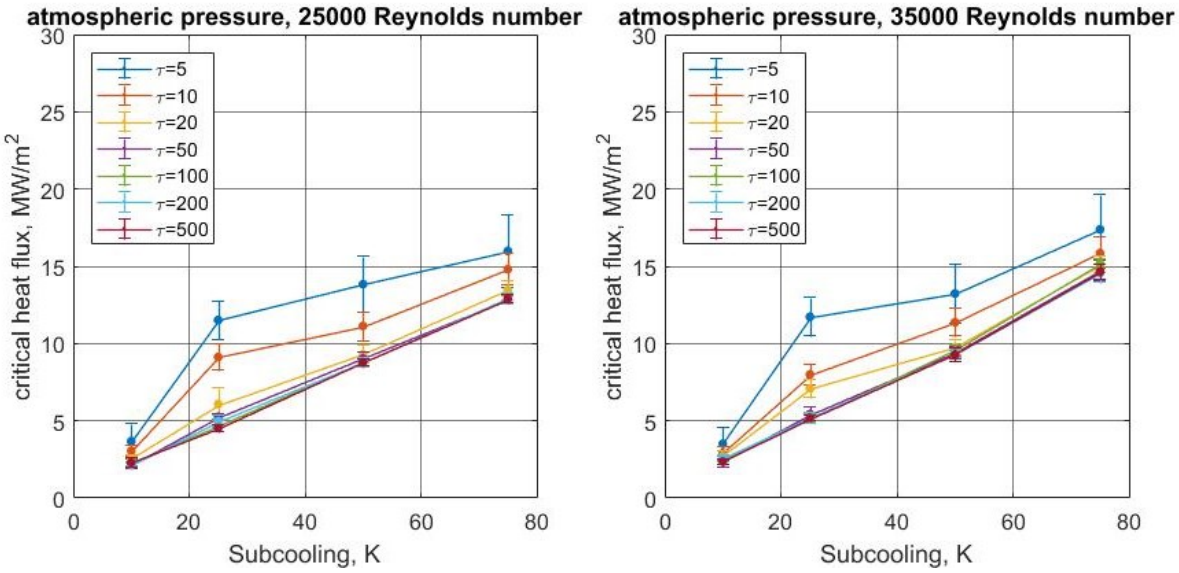

a) b)

Figure 18. CHF values for 25,000 (a) and 35,000 (b) Reynolds numbers

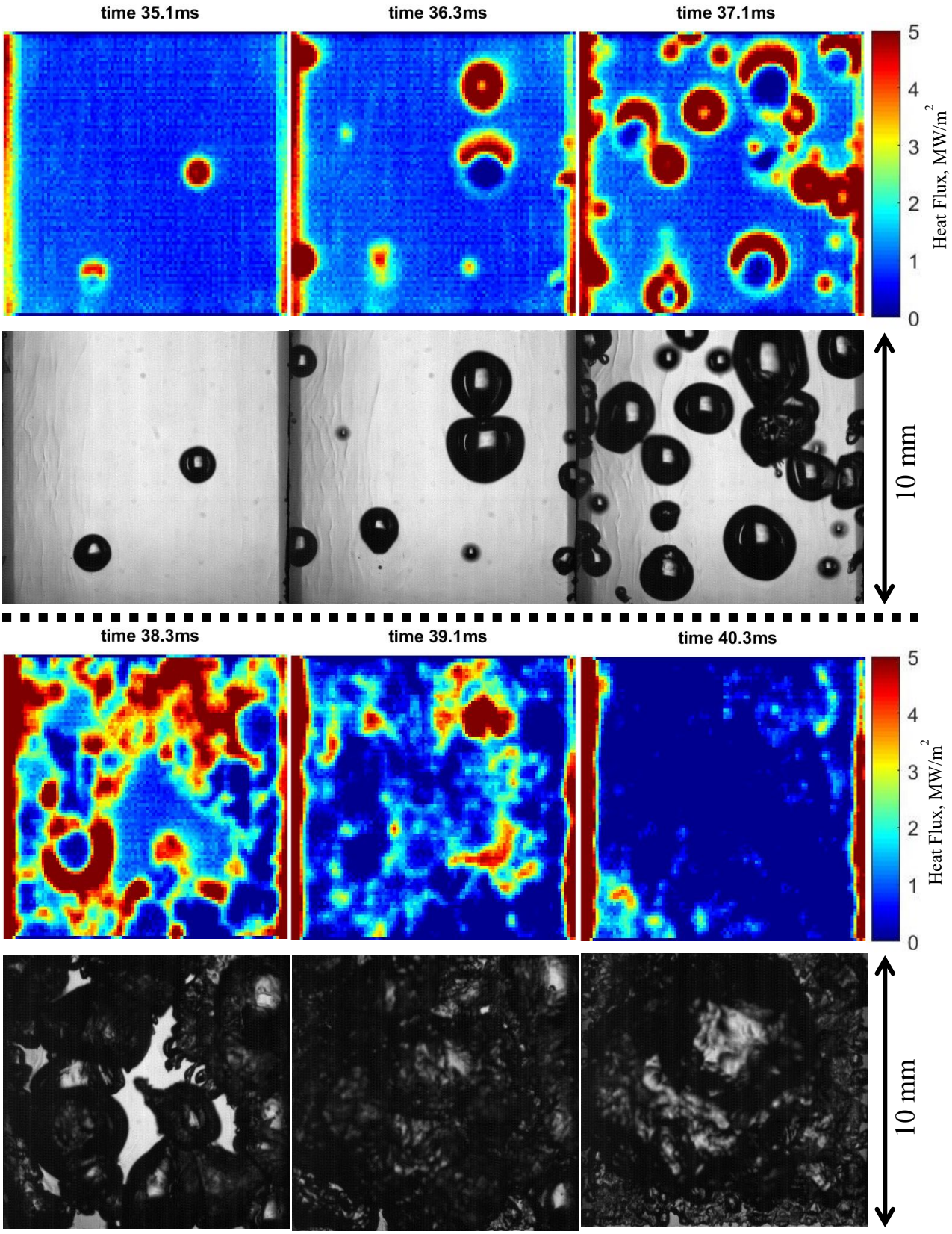

Figure 19. Progression of CHF at 10 K subcooling, 35,000 Reynolds number and 5 ms period

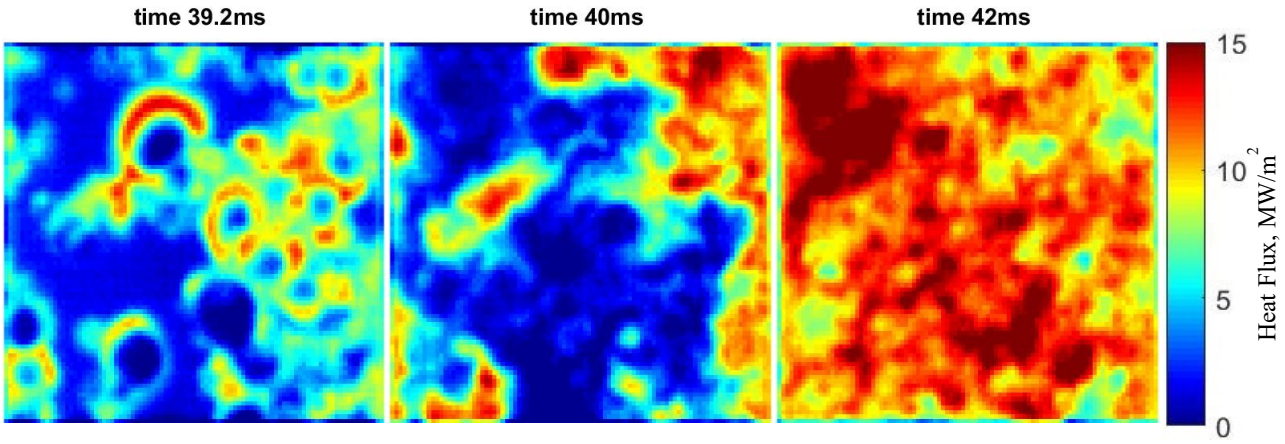

Figure 20. Illustration of the unstable reversible dry spot that forms on the boiling surface after ONB. Subcooling is 25 K; Reynolds number is 13,500; period is 5 ms

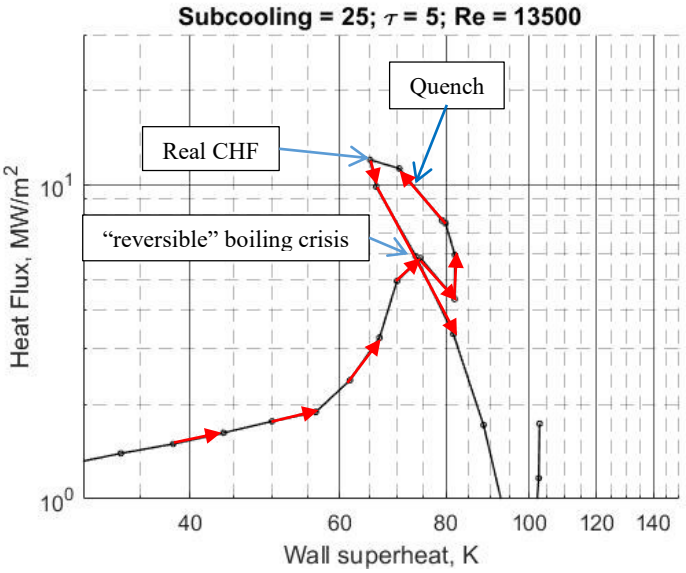

Figure 21. Boiling curve for 25 K subcooling, 35,000 Reynolds number and 5 ms period

In highly subcooled cases, multiple generations of bubbles precede CHF. The transition between ONB and DNB in such cases is best illustrated with the HSV recording (Figure 22). As the single-phase regime (frame 755) transitions to FDNB (frames 782 and 797) an explosive activation of multiple nucleation sites is observed. Notably, bubbles created during the first generation are significantly larger than the following generations. This could be explained by considering the amount of energy that is stored in the superheated liquid layer prior to ONB. This energy allows the first generation of bubbles to grow to large sizes before they recondense. The disturbance of the thermal boundary layer caused by nucleating bubbles as well as the quenching process that follows bubble recondensation lowers the total energy available for the next generation to grow. This can be observed on frame 807 which depicts the beginning of FDNB regime. As transient proceeds, the amount of bubbles as well as their sizes are increased (frame 830). Eventually, swarms of bubbles start to interact with each other and form vapor blankets at certain areas of the heater leading to dry spots formation (frame 879, vapor blankets are outlined).

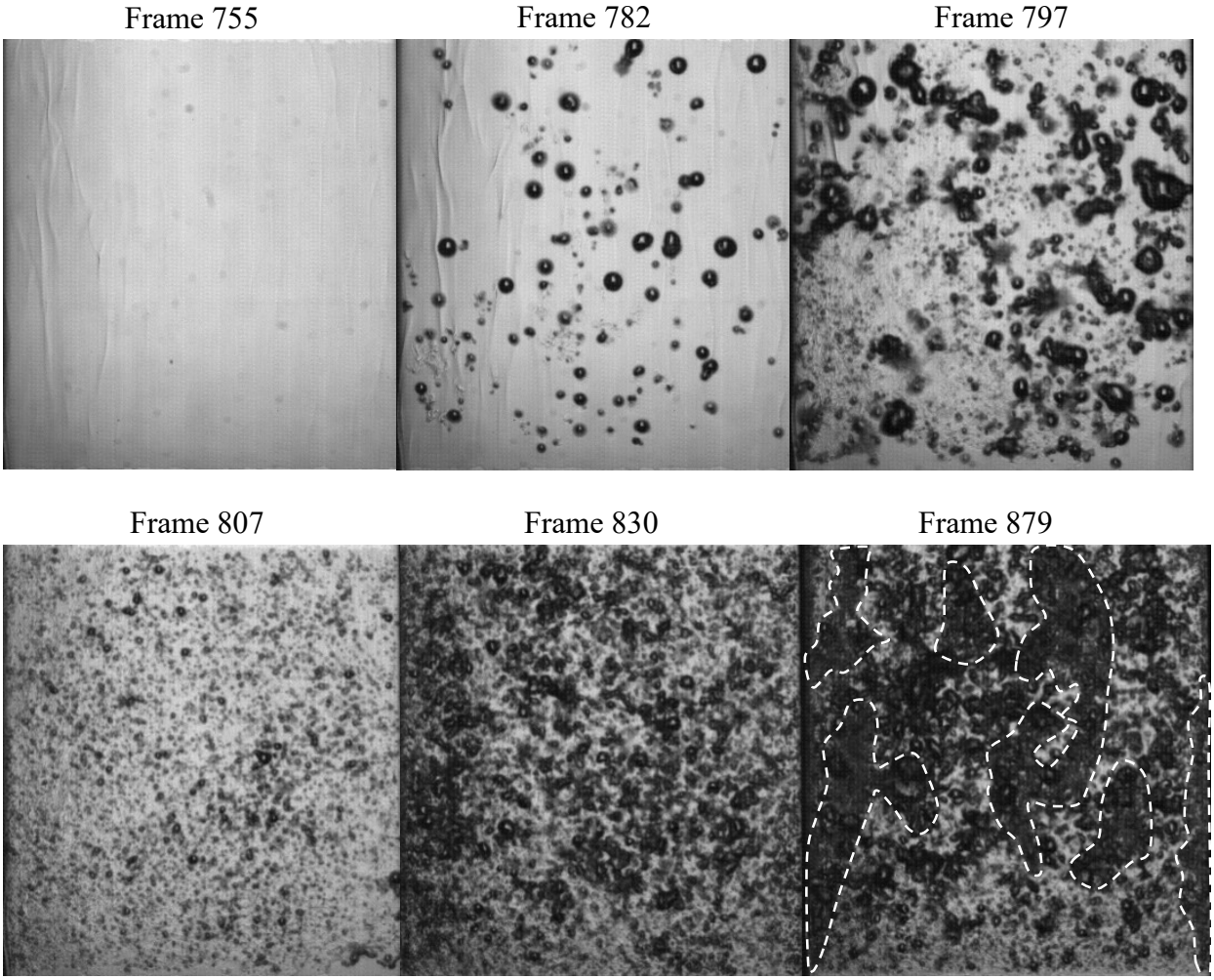

Figure 22. Progression of CHF at 75 K subcooling, 25,000 Reynolds number and 5 ms period

3.4. Influence of the coastdown

In our experiments the power was rapidly decreased right after the peak of the escalation was reached. However, in real RIA the coastdown may take a period of time similar to the escalation. Therefore, there is a risk that CHF may happen during the coastdown when the power level is still high. In order to investigate this possibility we performed several tests with the coastdown of the same period as the escalation. Experimental conditions were set at 75 K subcooling, 35,000 Reynolds number, atmospheric pressure and several short escalation periods (5, 10, 20 and 50 ms). The peak power was increased in small steps until the first irreversible dry spot was observed. In all tests CHF was happening exactly at the peak of power and was never observed during the coastdown.

4. Conclusion and Future Work

The thesis describes the investigation of the transient flow boiling CHF. The explored test matrix includes four subcoolings (10, 25, 50 and 75 K), three Reynolds numbers (as low as possible, 25000, 35000) and 7 power escalation periods (5, 10, 20, 50, 100, 200 and 500 ms). During each experiment the power of the heater was increased exponentially and different boiling regimes including CHF were observed. Each test was repeated three times to improve statistics. Outputs of the current study include:

- 252 sets of temporally and spatially resolved heat flux and temperature distributions on the boiling surface;
- 84 high speed video visualizations of the boiling process
- 252 measured CHF values

It was found that for short periods CHF does not depend on Reynolds number (at least for the range of Reynolds numbers explored in the current study). For escalation periods longer than 100 ms, CHF does not depend on escalation period. For escalation periods shorter than 100 ms CHF increases with decreasing period. The maximum CHF measured in the current study was 17.50 MW/m^2, in the test at 75 K subcooling, 35,000 Reynolds number and 5 ms period. CHF increases with subcooling for all conditions. Two different CHF mechanisms were observed depending on the subcooling. For cases with high subcooling (50 and 75 K) CHF resulted from the crowding of tiny pulsating bubbles. Amount and sizes of these bubbles grew during the FDNB regime, until they began to coalesce, leading to CHF. These observations were independent of power escalation period. A different CHF mechanism was observed at low subcoolings (10 K) and short periods (below 20 ms). In those conditions the first generation of bubbles was growing fast enough to quickly coalesce with each other and form a CHF dry spot right after the point of ONB. Finally, it was shown that long coast downs do not have any effect on the CHF initiation and progression when high subcoolings and short periods are concerned.

The current study was limited to atmospheric pressure tests. Therefore, future work should be focused on the effect of pressure on transient boiling phenomena. Moreover, it will be important to decrease the uncertainty of CHF measurements, as the temporal uncertainty associated with the limited frame rate of the HSIR camera becomes large at short escalation periods. In such conditions the heat flux rise between two consecutive IR frames is of the order of 1 MW/m^2. Additionally, the uncertainty on the measured values of the electrical power should be reduced. In the current study, this uncertainty contribution ranges between 0.1 and 0.4 MW/m^2. In the future the data presented here could be reduced using the dimensional analysis. This approach could provide a better understanding of the influence that multiple experimental conditions have on transient CHF.

Only a relatively small fraction of the data is presented in the main body of the thesis. The rest of the test matrix is reported in the appendices. Appendix B contains the power curves that were used as inputs in the current study. Appendix C presents the boiling curves that were measured in the current study. Appendix D has CHF values in graphical as well as tabulated form. Finally, Appendix E describes the uncertainty quantification.

References

[1] Nuclear Energy Agency, *Nuclear Fuel Behaviour Under Reactivity-initiated Accident (RIA) Conditions*, no. 6847. 2010.

[2] J. R. Lamarsh, "Introduction to Nuclear Reactor Theory." Addison-Wesley, pp. 1–581, 1996.

[3] J. R. Lamarsh, "Introduction to Nuclear Reactor Theory." Addison-Wesley Publishing Company, pp. 1–581, 1972.

[4] P. Van Uffelen, R. J. M. Konings, C. Vitanza, and J. Tulenko, "Analysis of Reactor Fuel Rod Behavior," *Handb. Nucl. Eng.*, 2010.

[5] V. Bessiron, "Modelling of clad-to-coolant heat transfer for RIA applications," *J. Nucl. Sci. Technol.*, vol. 44, no. 2, pp. 211–221, 2007.

[6] M. W. Rosenthal and R. L. Miller, "An experimental study of transient boiling," Oak Ridge, Tennesee, 1957.

[7] M. Soliman and H. A. Johnson, "Transient Heat Transfer for Forced Convection Flow over a Flat Plate of Appreciable Thermal Capacity and Containing an Exponential Time-Dependent Heat Source," *Int. J. Heat Mass Transf.*, vol. 11, pp. 27–38, 1968.

[8] I. Kataoka, A. Serizawa, and A. Sakurai, "Transient boiling heat transfer under forced convection," *Int. J. Heat Mass Transf.*, vol. 26, no. 4, pp. 583–595, 1983.

[9] G. Y. Su, M. Bucci, T. McKrell, and J. Buongiorno, "Transient boiling of water under exponentially escalating heat inputs. Part II: Flow boiling," *Int. J. Heat Mass Transf.*, vol. 96, pp. 685–698, 2016.

[10] H. A. Johnson, "Transient boiling heat transfer to water," *Int. J. Heat Mass Transf.*, vol. 14, no. 1, pp. 67–82, 1971.

[11] A. Sakurai, *Mechanisms of transitions to film boiling at CHFs in subcooled and pressurized liquids due to steady and increasing heat inputs*, vol. 197, no. 3. 2000.

[12] G.-Y. Su, M. Bucci, T. Mckrell, and J. Buongiorno, "Transient boiling of water under exponentially escalating heat inputs. Part I: Pool boiling," *Int. J. Heat Mass Transf.*, vol. 96, pp. 667–684, 2016.

[13] A. Sakurai and M. Shiotsu, "Transient Pool Boiling Heat Transfer. Part1: Incipient Boiling Superheat," *J. Heat Transfer*, vol. 99, no. November 1977, pp. 547–553, 1977.

[14] V. P. Carey, *Liquid-Vapor Phase-Change Phenomena*, 2nd ed. New York: Taylor & Francis Group, 2008.

[15] A. Serizawa, "Theoretical prediction of maximum heat flux in power transients," *Int. J. Heat Mass Transf.*, 1983.

[16] K. O. Pasamehmetoglu, R. A. Nelson, and F. S. Gunnerson, "Critical Heat Flux modeling in Forced Convection Boiling During Power Transients," *J. Heat Transfer*, vol. 112, pp. 1058–1062, 1990.

[17] Y. Haramura and Y. Katto, "A new hydrodynamic model of critical heat flux, applicable

widely to both pool and forced convection boiling on submerged bodies in saturated liquids," *Int. J. Heat Mass Transf.*, vol. 26, no. 3, pp. 389–399, 1983.

[18] M. Bucci, A. Richenderfer, G.-Y. Su, T. Mckrell, and J. Buongiorno, "A mechanistic IR calibration technique for boiling heat transfer investigations," *Int. J. Multiph. Flow*, vol. 83, pp. 115–127, 2016.

Appendix A. Temperature distribution in the substrate

To explore the resistance of the selected heater design to high thermal stresses and high temperatures, a test on a sacrificial heater was performed. The heater that has been used in the test consisted of a 250 μm thick sapphire substrate coated with an electrically conductive layer of stainless steel. An exponential power input with a 5 ms period was supplied to the heater. The coast down of the power escalation followed the same period. The peak value of the escalation was gradually increased until the breakdown of the heater occurred. Figure A1 (a) illustrates the maximum power achieved before the heater was damaged. Figure A1 (b) illustrates the power input during a normal run. Note that only the electrical connection which was made by means of silver epoxy was damaged, while the substrate stayed intact. Notably, the heater eventually used in the experiments is four times thicker and does not use silver epoxy; the electrical connections have been realized by mechanical clamping.

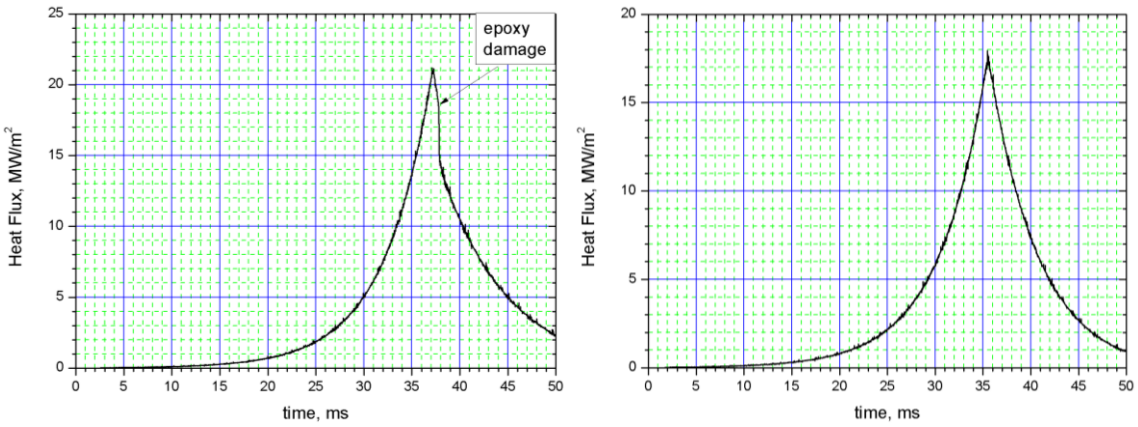

a) b)

Figure A1. Exponential power inputs. (a) – maximum power achieved. Note the time at which silver epoxy got damaged during the coast down. (b) – successful run with no damage

To investigate the risk of thermal stress in the heater, a heat transfer simulation was performed. The power input from the normal run (Figure A1(b)) was used as a shape function for the power source. Period and magnitude of the power input were changed in order to analyze a wide range of parameters. It is not clear whether or not CHF will occur upon escalation or the coast down of the power. Therefore, it was assumed that the coast down follows the same period as escalation even for long periods[3]. The simulation features a simple 1D finite difference code which solves the transient conduction equation

[3] For long periods the power coast down can add significant heat to the heater. In the actual tests we will be able to reduce the power much faster and avoid the coast down phase altogether.

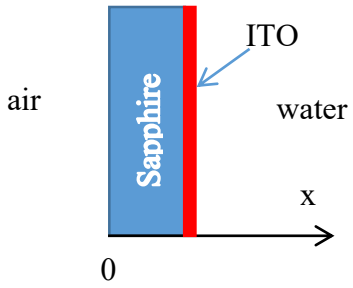

$$\frac{\partial T(x,t)}{\partial t} = a_s \cdot \frac{\partial^2 T(x,t)}{\partial x^2}, \tag{A1}$$

where T is temperature of the sapphire, x is coordinate of the point of interest, t is the time from the beginning of the escalation and a_s is thermal diffusivity of sapphire. The adiabatic boundary condition is assumed on the air side[4]

$$-k_s \cdot \left.\frac{dT(x,t)}{dx}\right|_{x=0} = 0, \tag{A2}$$

where k_s is thermal conductivity of the sapphire. On the water side the difference between heat addition from the escalation and heat removal by water is applied as a boundary condition

$$-k_s \cdot \left.\frac{dT(x,t)}{dx}\right|_{x=L} = -q''(t) + h_w(t) \cdot \left[T(L,t) - T_{bulk}\right] \tag{A3}$$

where L = 1 mm is the substrate thickness; $q''(t)$ is the heat flux supplied by the power escalation, $h_w(t)$ the heat transfer coefficient between ITO and water and T_{bulk} is the bulk temperature of water. The heat transfer coefficient (HTC) has different values depending on the heat transfer regime. For the single-phase heat transfer the direct experimental data for HTC was taken from the previous experiments [Su2016b].

$$h_{sf} = const \tag{A4}$$

A simplified assumption was made that the change from single phase to boiling heat transfer occurs when the predicted boiling heat flux exceeds the single-phase heat flux, i.e.

$$C \cdot \left[T(L,t) - T_{sat}\right]^4 > h_{sf} \cdot \left[T(L,t) - T_{bulk}\right], \tag{A5}$$

where T_{sat} is the saturation temperature of water C is an empirical constant which depends on subcooling [Su2016b], and h_{sf} is the single-phase HTC. The HTC for boiling regime was calculated as follows

$$h_{FDNB} = \frac{C \cdot \left[T(L,t) - T_{sat}\right]^4}{\left[T(L,t) - T_{bulk}\right]}. \tag{A6}$$

[4] Even if natural convection boundary condition is assumed it brings negligible change

Finally, it was assumed that CHF occurs exactly at the power peak of the escalation and the heat transfer coefficient goes to zero

$$h_{CHF} = 0 \tag{A7}$$

The initial condition consists in a uniform temperature distribution across the substrate

$$\forall x, \quad T(x,0) = T_{bulk} \tag{A8}$$

As a result of the simulation we get a temperature distribution across the sapphire at any time of the escalation. Figure A2 illustrates an example of such simulation. Knowing the temperature distribution, we can find the maximum value of the temperature drop over the sapphire thickness ΔT_s, and evaluate accordingly what is the risk of thermal shock, as defined in Table A.1. The maximum value is usually achieved shortly after CHF. Table A1 gives the definitions of terms used in Tables Table 2 and Table 3 of the report.

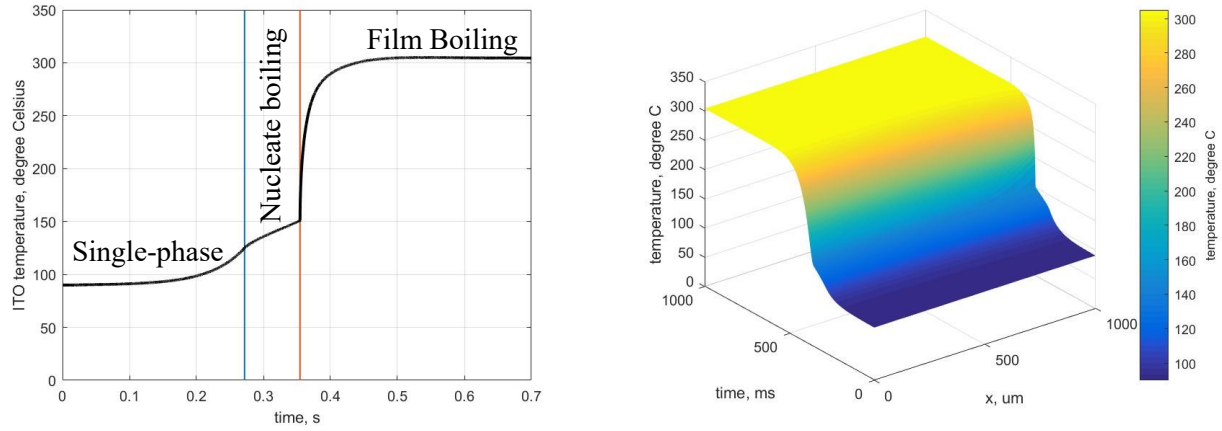

a) b)

Figure A2. Results of the simulation for the 50 ms period, 10 K subcooling and peak heat flux of 10 MW/m^2; ITO temperature (a) and temperature distribution in sapphire (b)

Table A1 Definitions for terms used in the report

Term	Definition
"Single-phase"	The peak value of the heat flux is not high enough to initiate boiling, i.e. Eq. A5 was not satisfied at any time.
"Good"	Nucleate boiling was initiated. Additionally a value of thermal stress for the maximum $\Delta T_{s,max}$ was calculated using the following equation $f = \alpha \cdot E \cdot \Delta T_{s,\max}$, where α is the thermal expansion coefficient of sapphire and E is the sapphire Young's modulus. If this value is less than the tensile strength of the sapphire, the condition was marked as "Good".
"Risk of thermal shock"	The thermal stress is higher than the tensile strength of the sapphire.

Appendix B. Power inputs

Recorded curves of the total applied heat flux (sum of the heat flux to water and to sapphire) versus the escalation period are shown below. Each plot represents a unique combination of subcooling and escalation period. Because each test was repeated three times, distinct plots for three different "trials" are given.

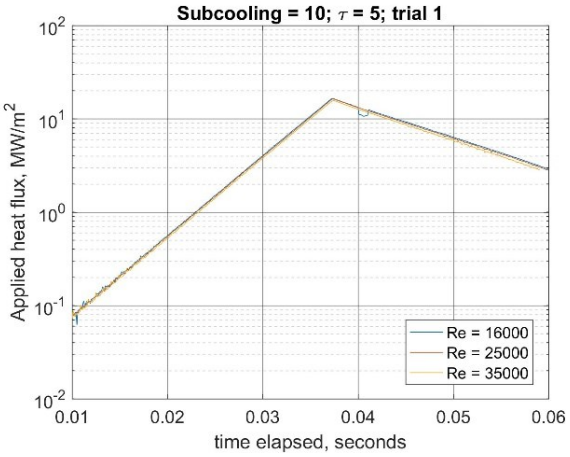

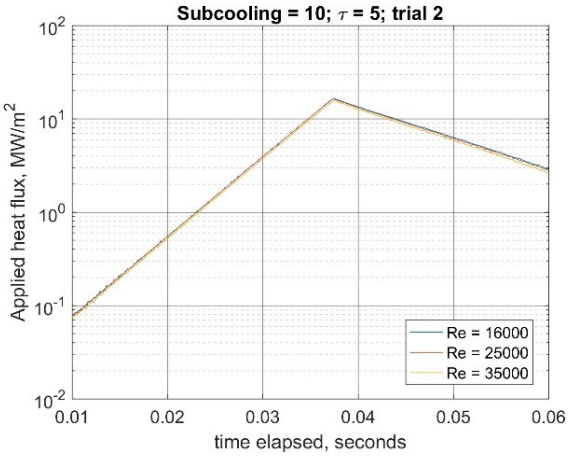

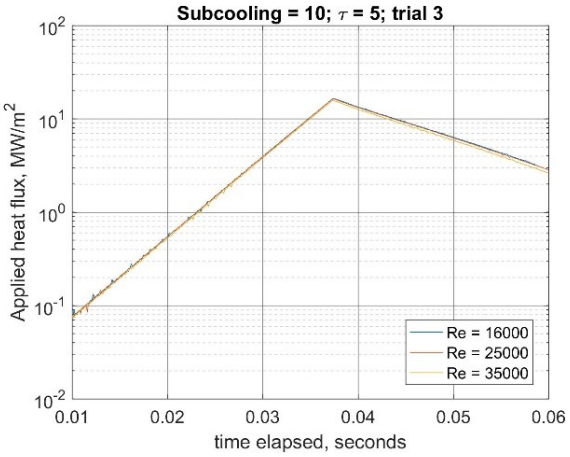

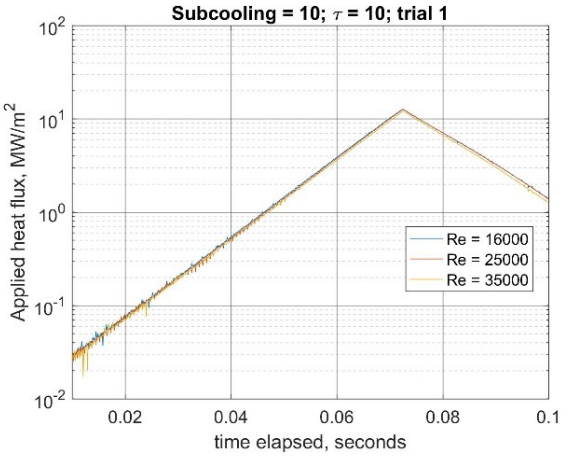

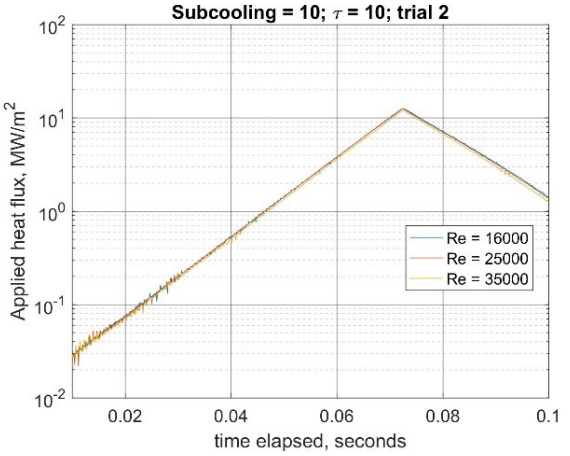

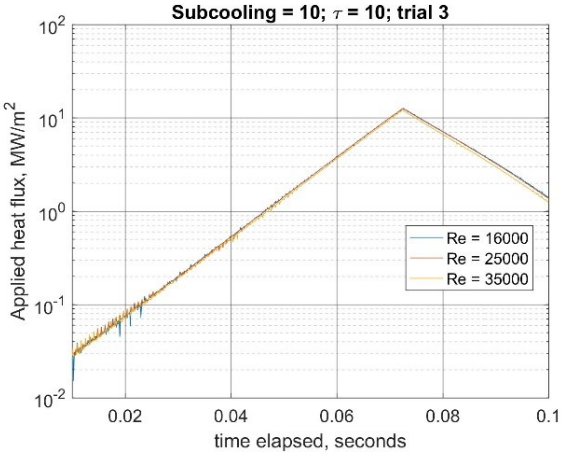

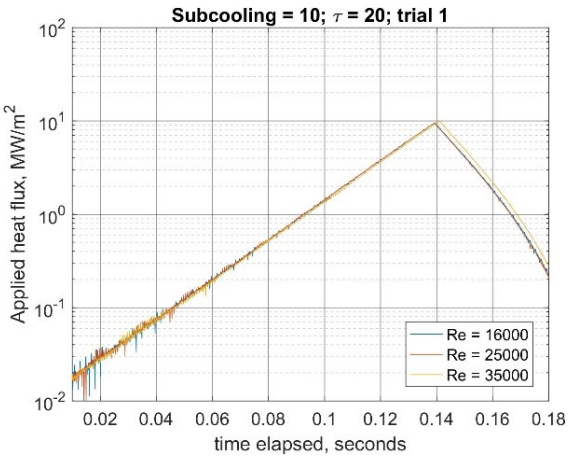
Subcooling = 10; τ = 20; trial 1
Applied heat flux, MW/m2
time elapsed, seconds
Re = 16000
Re = 25000
Re = 35000

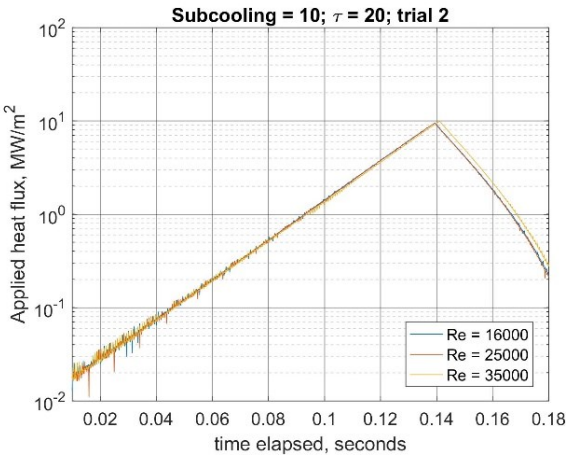
Subcooling = 10; τ = 20; trial 2
Applied heat flux, MW/m2
time elapsed, seconds
Re = 16000
Re = 25000
Re = 35000

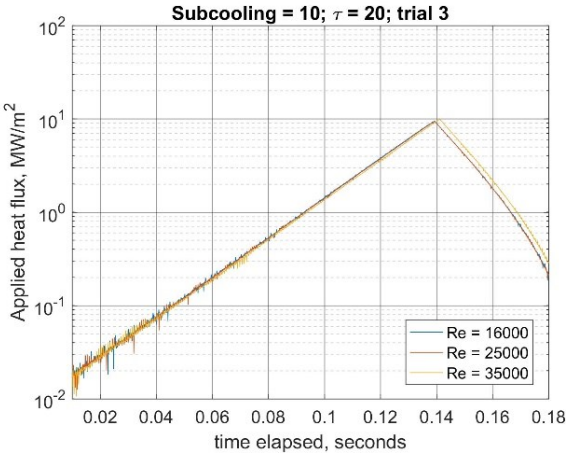
Subcooling = 10; τ = 20; trial 3
Applied heat flux, MW/m2
time elapsed, seconds
Re = 16000
Re = 25000
Re = 35000

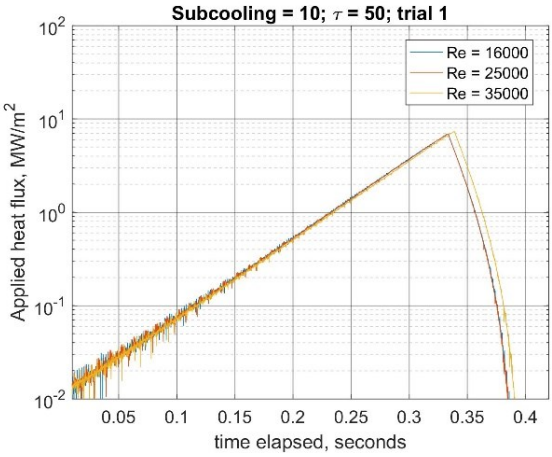
Subcooling = 10; τ = 50; trial 1
Applied heat flux, MW/m2
time elapsed, seconds
Re = 16000
Re = 25000
Re = 35000

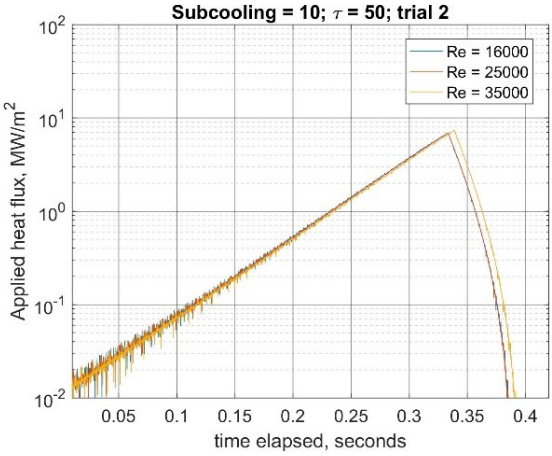
Subcooling = 10; τ = 50; trial 2
Applied heat flux, MW/m2
time elapsed, seconds
Re = 16000
Re = 25000
Re = 35000

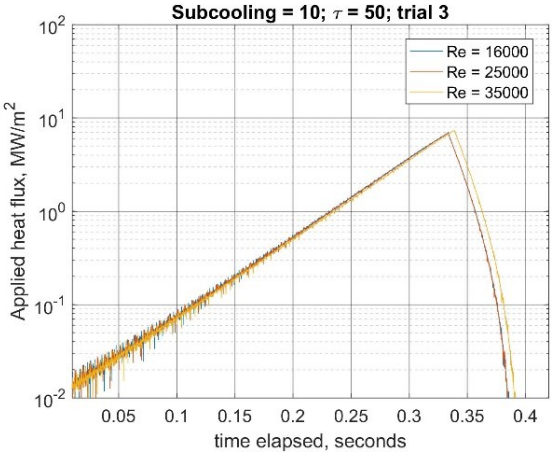
Subcooling = 10; τ = 50; trial 3
Applied heat flux, MW/m2
time elapsed, seconds
Re = 16000
Re = 25000
Re = 35000

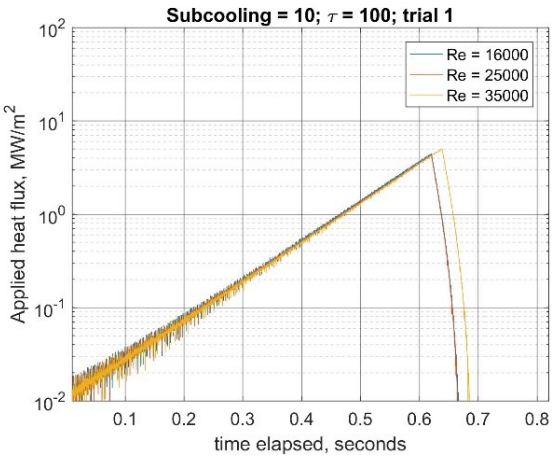
Subcooling = 10; τ = 100; trial 1
Re = 16000
Re = 25000
Re = 35000
Applied heat flux, MW/m2
time elapsed, seconds

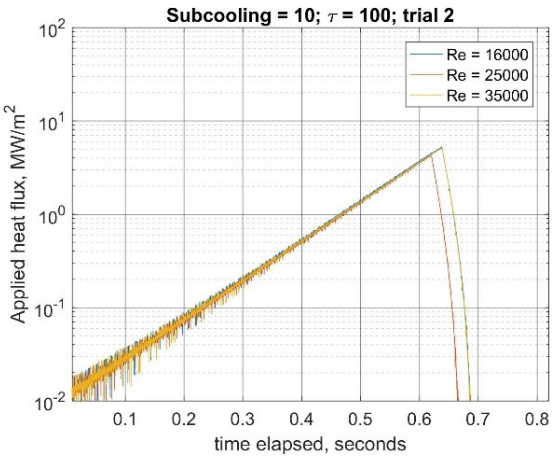
Subcooling = 10; τ = 100; trial 2
Re = 16000
Re = 25000
Re = 35000
Applied heat flux, MW/m2
time elapsed, seconds

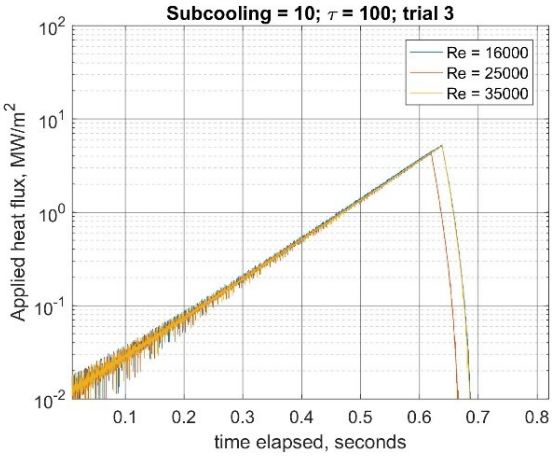
Subcooling = 10; τ = 100; trial 3
Re = 16000
Re = 25000
Re = 35000
Applied heat flux, MW/m2
time elapsed, seconds

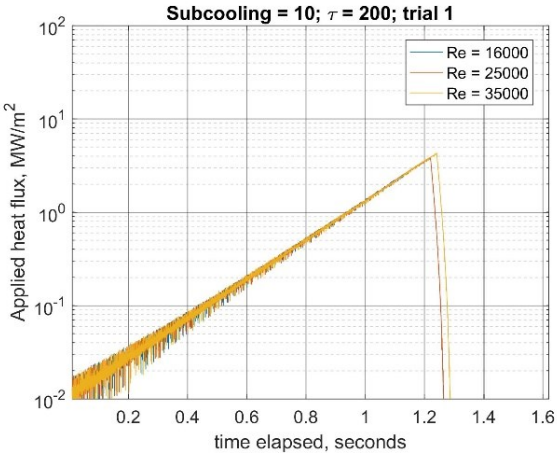
Subcooling = 10; τ = 200; trial 1
Re = 16000
Re = 25000
Re = 35000
Applied heat flux, MW/m2
time elapsed, seconds

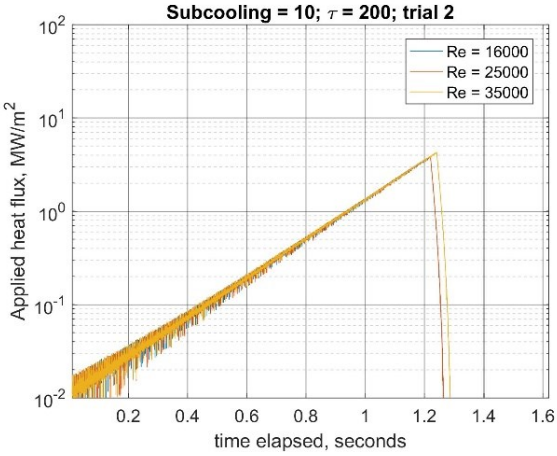
Subcooling = 10; τ = 200; trial 2
Re = 16000
Re = 25000
Re = 35000
Applied heat flux, MW/m2
time elapsed, seconds

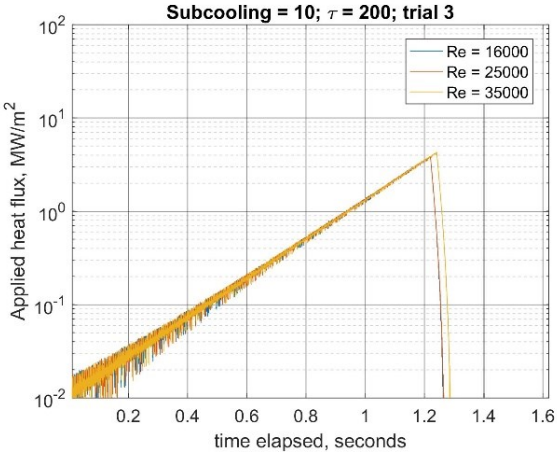
Subcooling = 10; τ = 200; trial 3
Re = 16000
Re = 25000
Re = 35000
Applied heat flux, MW/m2
time elapsed, seconds

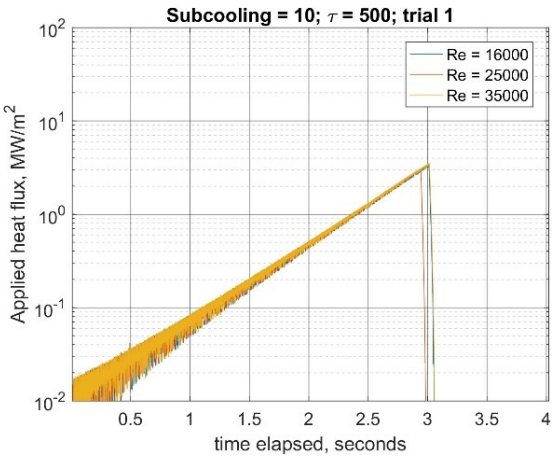
Subcooling = 10; τ = 500; trial 1
Re = 16000
Re = 25000
Re = 35000
Applied heat flux, MW/m^2
time elapsed, seconds

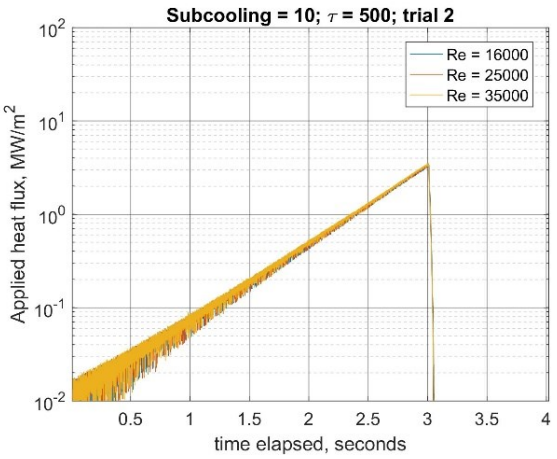
Subcooling = 10; τ = 500; trial 2
Re = 16000
Re = 25000
Re = 35000
Applied heat flux, MW/m^2
time elapsed, seconds

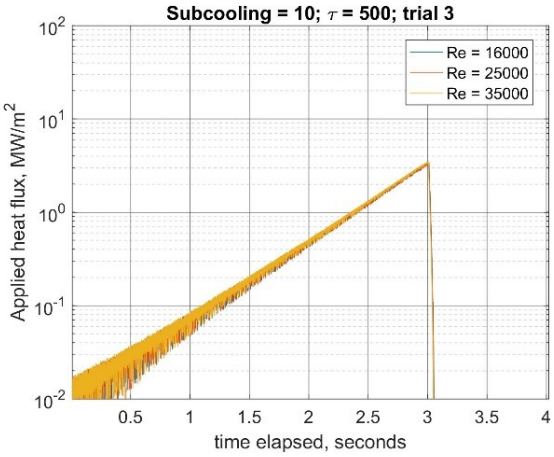
Subcooling = 10; τ = 500; trial 3
Re = 16000
Re = 25000
Re = 35000
Applied heat flux, MW/m^2
time elapsed, seconds

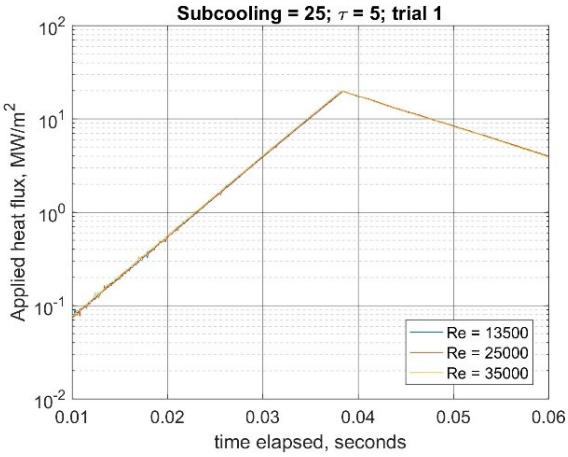
Subcooling = 25; τ = 5; trial 1
Re = 13500
Re = 25000
Re = 35000
Applied heat flux, MW/m^2
time elapsed, seconds

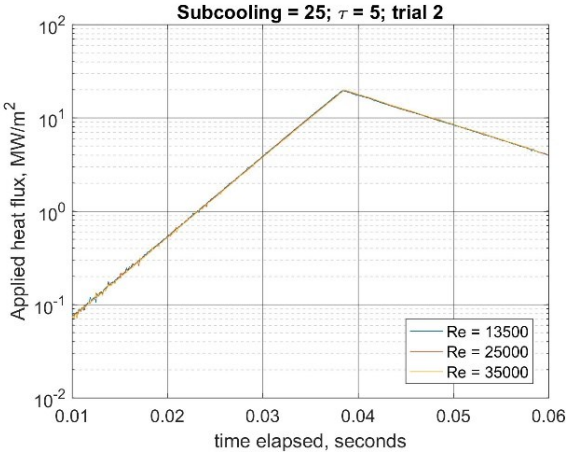
Subcooling = 25; τ = 5; trial 2
Re = 13500
Re = 25000
Re = 35000
Applied heat flux, MW/m^2
time elapsed, seconds

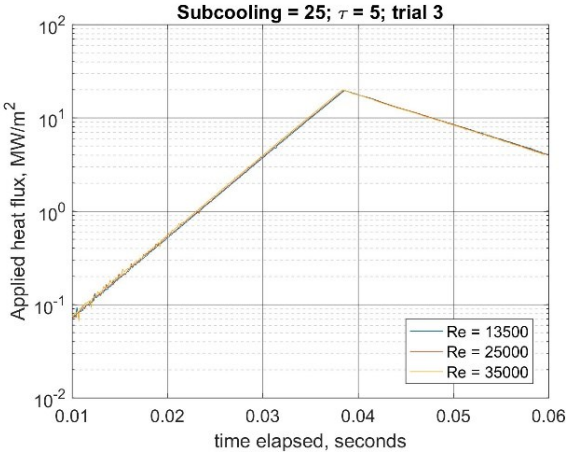
Subcooling = 25; τ = 5; trial 3
Re = 13500
Re = 25000
Re = 35000
Applied heat flux, MW/m^2
time elapsed, seconds

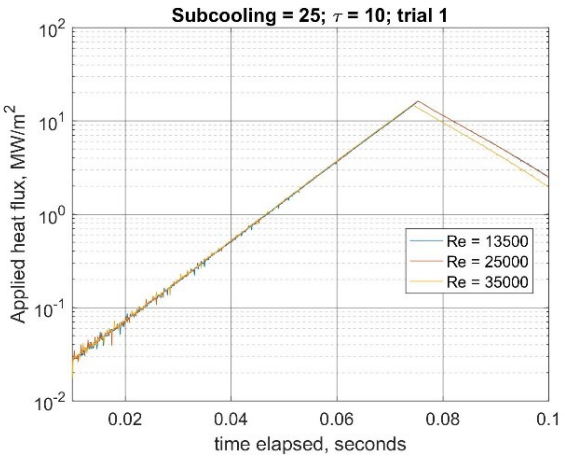
Subcooling = 25; τ = 10; trial 1
Applied heat flux, MW/m^2
time elapsed, seconds
Re = 13500
Re = 25000
Re = 35000

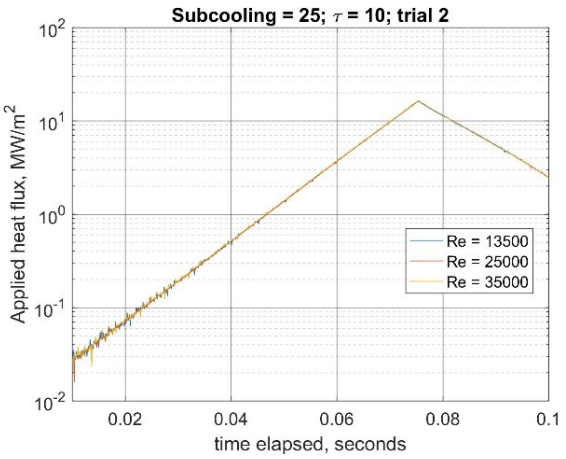
Subcooling = 25; τ = 10; trial 2
Applied heat flux, MW/m^2
time elapsed, seconds
Re = 13500
Re = 25000
Re = 35000

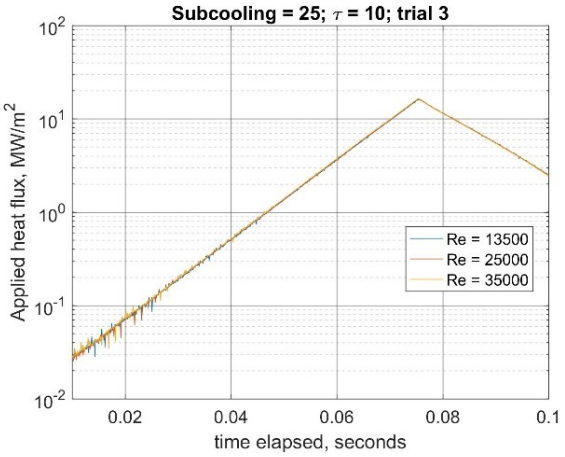
Subcooling = 25; τ = 10; trial 3
Applied heat flux, MW/m^2
time elapsed, seconds
Re = 13500
Re = 25000
Re = 35000

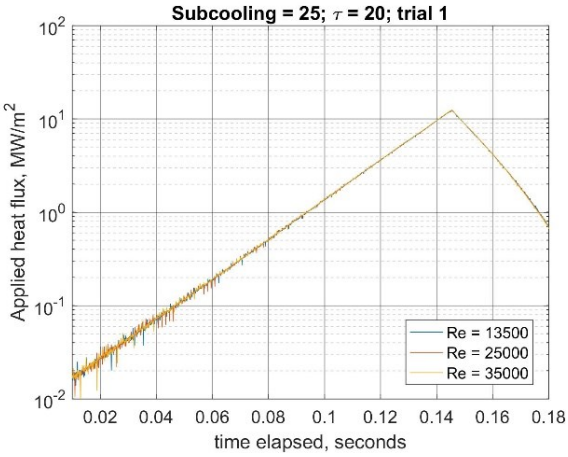
Subcooling = 25; τ = 20; trial 1
Applied heat flux, MW/m^2
time elapsed, seconds
Re = 13500
Re = 25000
Re = 35000

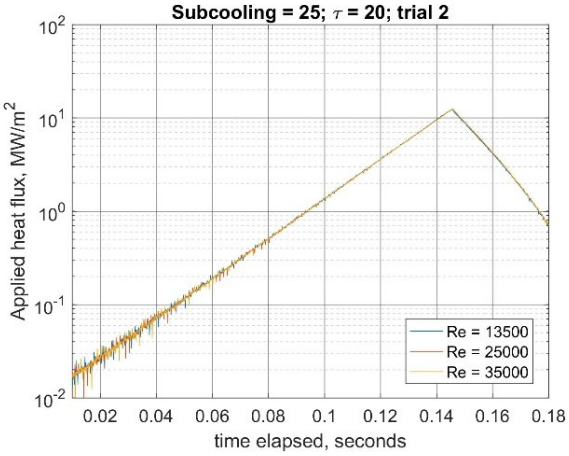
Subcooling = 25; τ = 20; trial 2
Applied heat flux, MW/m^2
time elapsed, seconds
Re = 13500
Re = 25000
Re = 35000

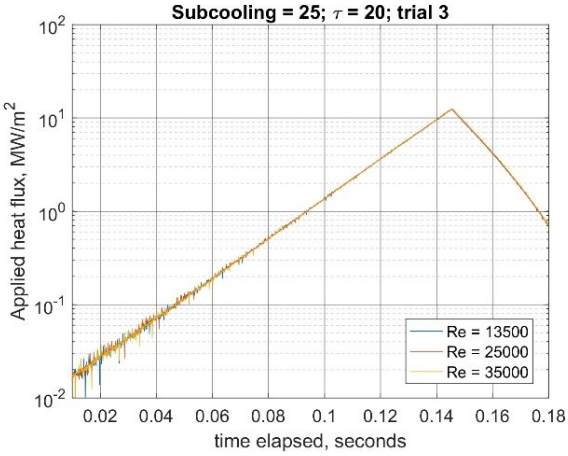
Subcooling = 25; τ = 20; trial 3
Applied heat flux, MW/m^2
time elapsed, seconds
Re = 13500
Re = 25000
Re = 35000

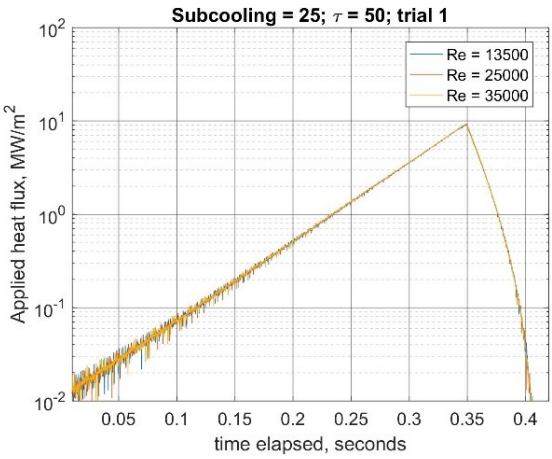
Subcooling = 25; τ = 50; trial 1
Re = 13500
Re = 25000
Re = 35000
Applied heat flux, MW/m2
time elapsed, seconds

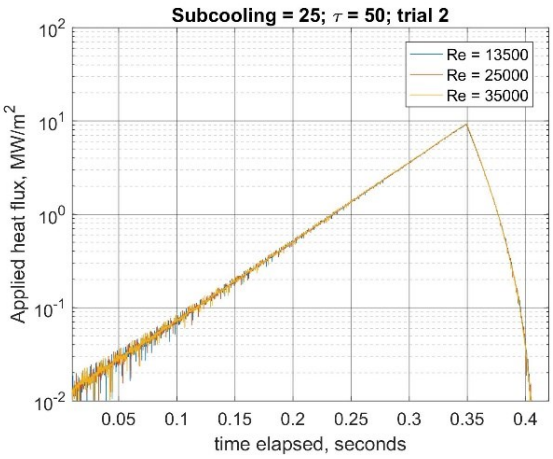
Subcooling = 25; τ = 50; trial 2
Re = 13500
Re = 25000
Re = 35000
Applied heat flux, MW/m2
time elapsed, seconds

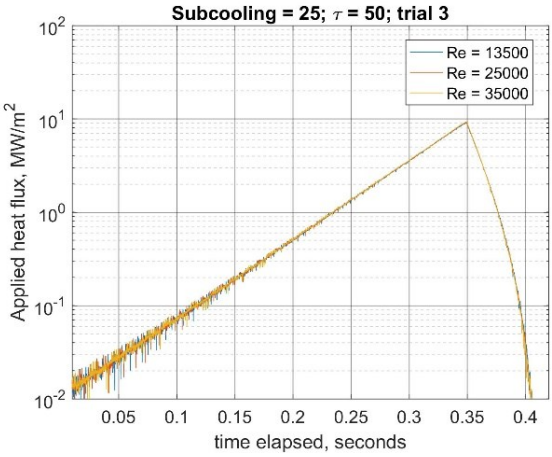
Subcooling = 25; τ = 50; trial 3
Re = 13500
Re = 25000
Re = 35000
Applied heat flux, MW/m2
time elapsed, seconds

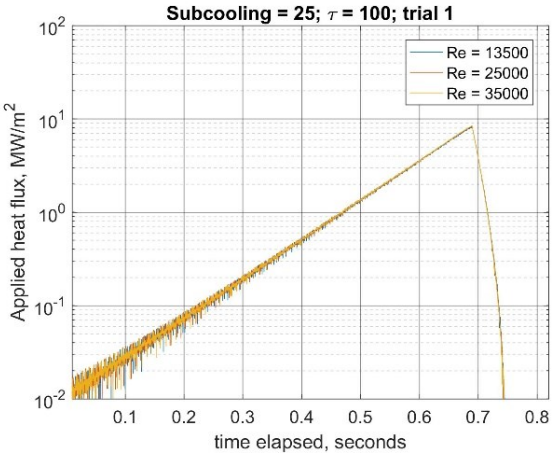
Subcooling = 25; τ = 100; trial 1
Re = 13500
Re = 25000
Re = 35000
Applied heat flux, MW/m2
time elapsed, seconds

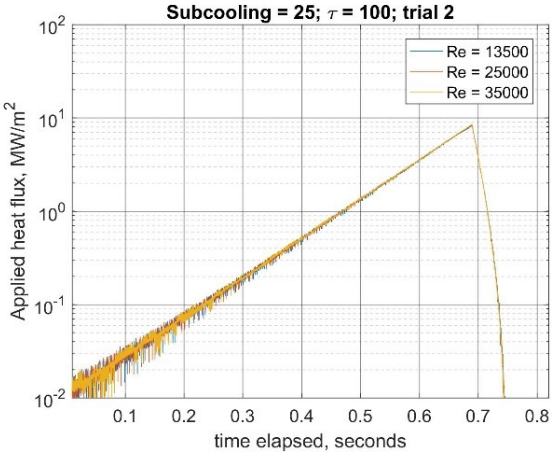
Subcooling = 25; τ = 100; trial 2
Re = 13500
Re = 25000
Re = 35000
Applied heat flux, MW/m2
time elapsed, seconds

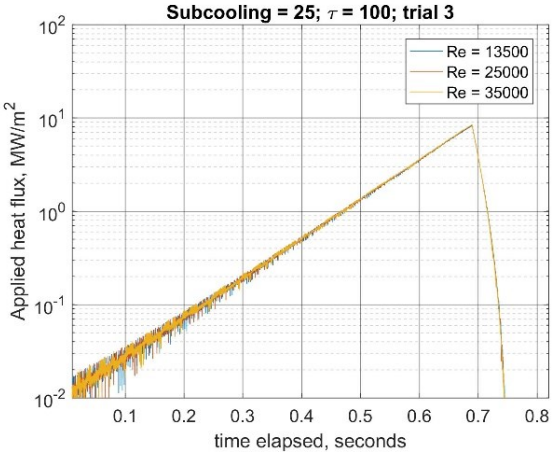
Subcooling = 25; τ = 100; trial 3
Re = 13500
Re = 25000
Re = 35000
Applied heat flux, MW/m2
time elapsed, seconds

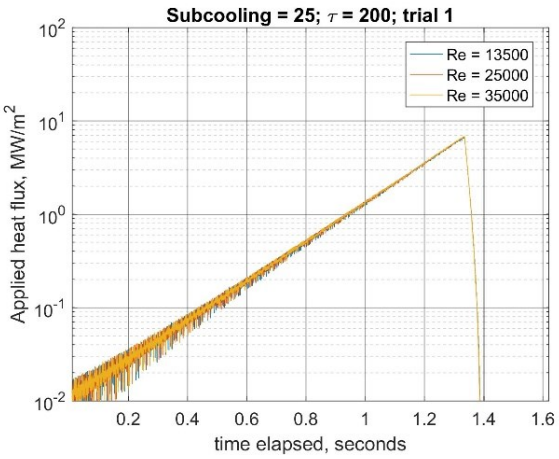
Subcooling = 25; τ = 200; trial 1
Re = 13500
Re = 25000
Re = 35000
Applied heat flux, MW/m2
time elapsed, seconds

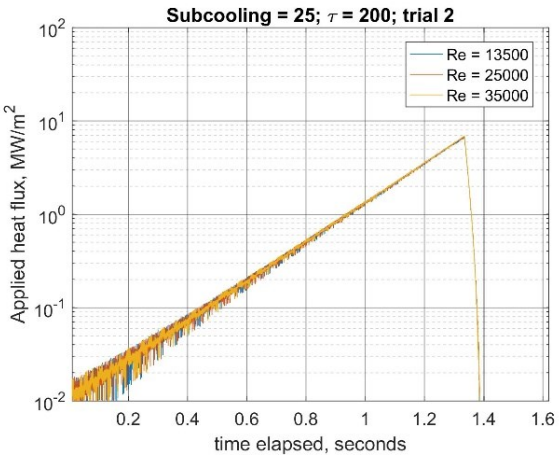
Subcooling = 25; τ = 200; trial 2
Re = 13500
Re = 25000
Re = 35000
Applied heat flux, MW/m2
time elapsed, seconds

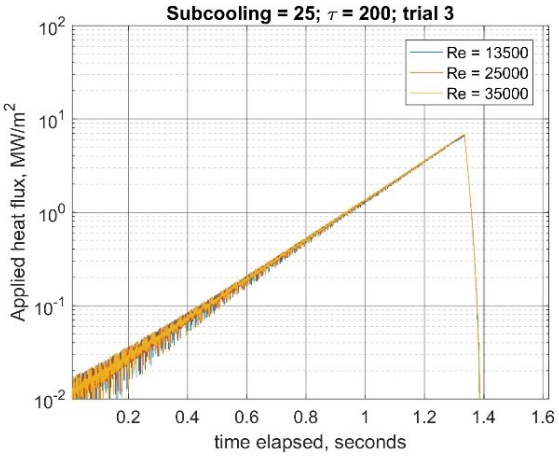
Subcooling = 25; τ = 200; trial 3
Re = 13500
Re = 25000
Re = 35000
Applied heat flux, MW/m2
time elapsed, seconds

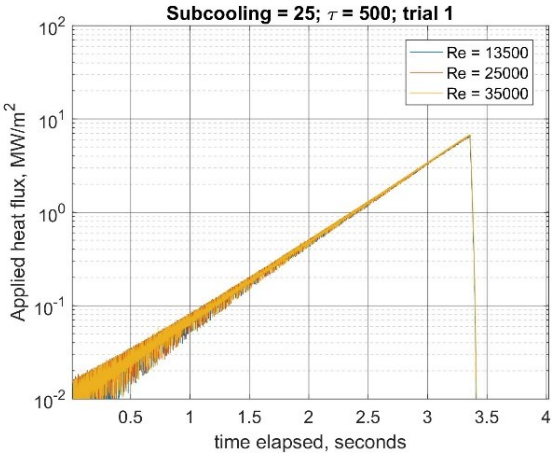
Subcooling = 25; τ = 500; trial 1
Re = 13500
Re = 25000
Re = 35000
Applied heat flux, MW/m2
time elapsed, seconds

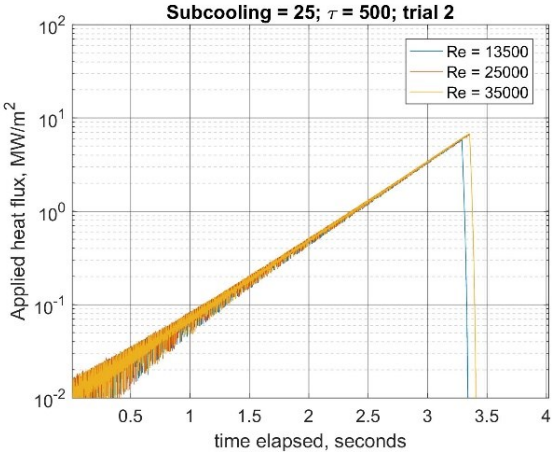
Subcooling = 25; τ = 500; trial 2
Re = 13500
Re = 25000
Re = 35000
Applied heat flux, MW/m2
time elapsed, seconds

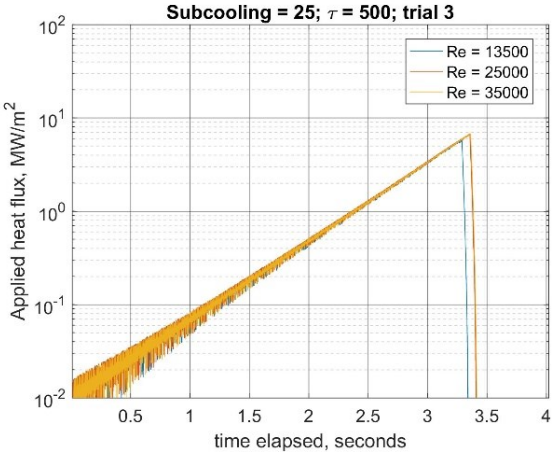
Subcooling = 25; τ = 500; trial 3
Re = 13500
Re = 25000
Re = 35000
Applied heat flux, MW/m2
time elapsed, seconds

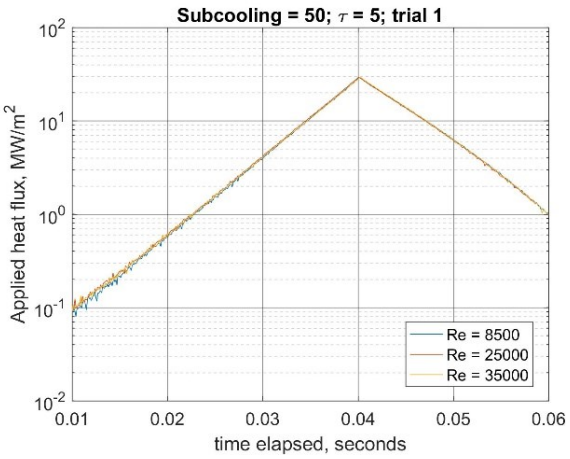
Subcooling = 50; τ = 5; trial 1
Applied heat flux, MW/m^2
time elapsed, seconds
Re = 8500
Re = 25000
Re = 35000

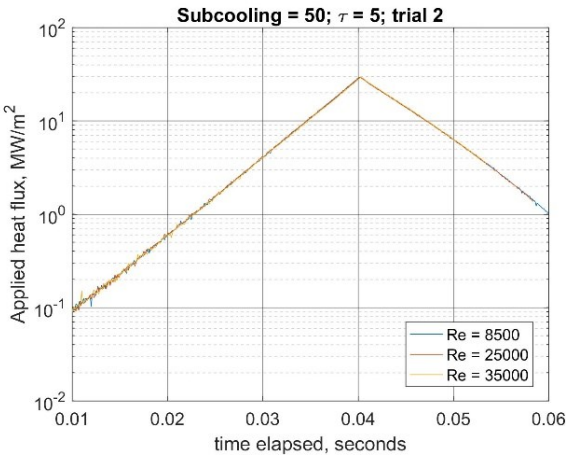
Subcooling = 50; τ = 5; trial 2
Applied heat flux, MW/m^2
time elapsed, seconds
Re = 8500
Re = 25000
Re = 35000

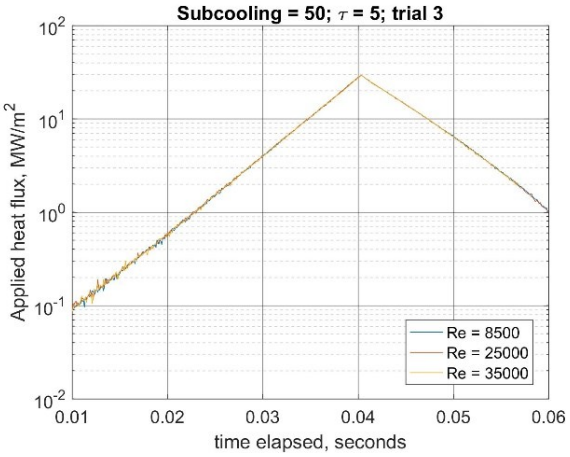
Subcooling = 50; τ = 5; trial 3
Applied heat flux, MW/m^2
time elapsed, seconds
Re = 8500
Re = 25000
Re = 35000

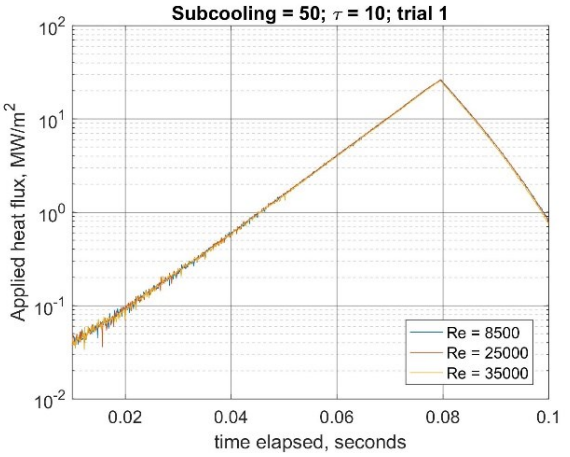
Subcooling = 50; τ = 10; trial 1
Applied heat flux, MW/m^2
time elapsed, seconds
Re = 8500
Re = 25000
Re = 35000

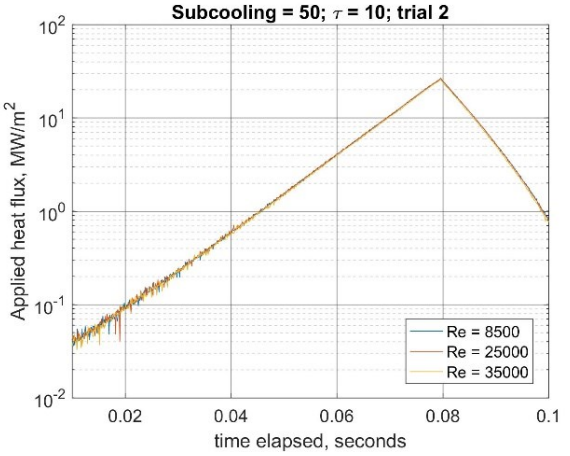
Subcooling = 50; τ = 10; trial 2
Applied heat flux, MW/m^2
time elapsed, seconds
Re = 8500
Re = 25000
Re = 35000

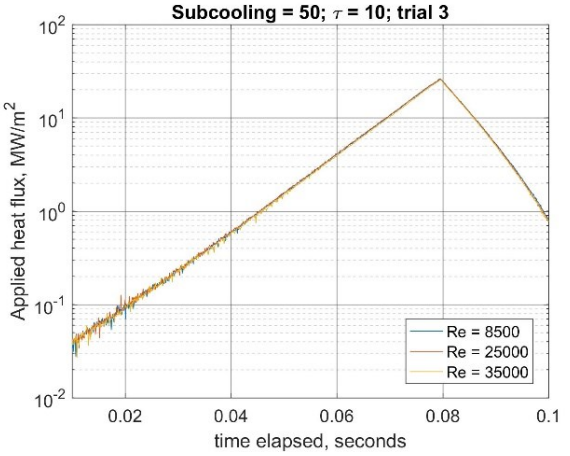
Subcooling = 50; τ = 10; trial 3
Applied heat flux, MW/m^2
time elapsed, seconds
Re = 8500
Re = 25000
Re = 35000

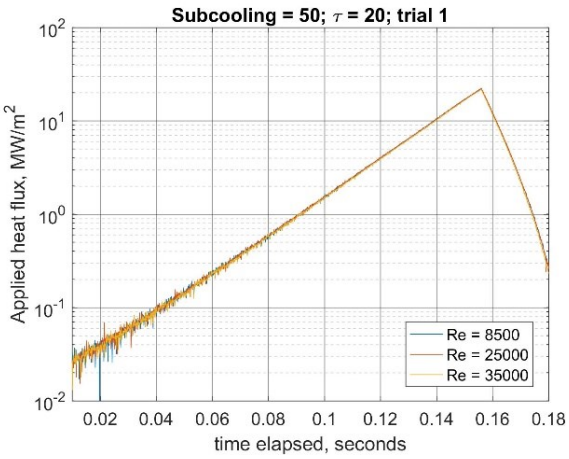
Subcooling = 50; τ = 20; trial 1
Applied heat flux, MW/m^2
time elapsed, seconds
Re = 8500
Re = 25000
Re = 35000

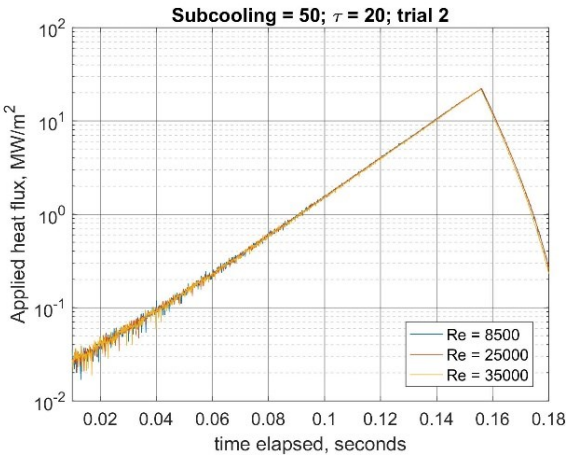
Subcooling = 50; τ = 20; trial 2
Applied heat flux, MW/m^2
time elapsed, seconds
Re = 8500
Re = 25000
Re = 35000

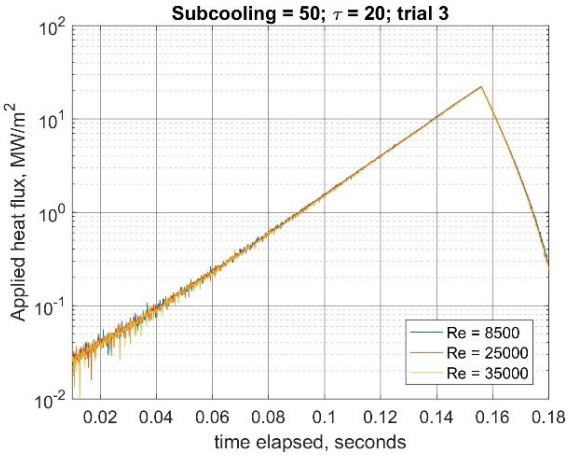
Subcooling = 50; τ = 20; trial 3
Applied heat flux, MW/m^2
time elapsed, seconds
Re = 8500
Re = 25000
Re = 35000

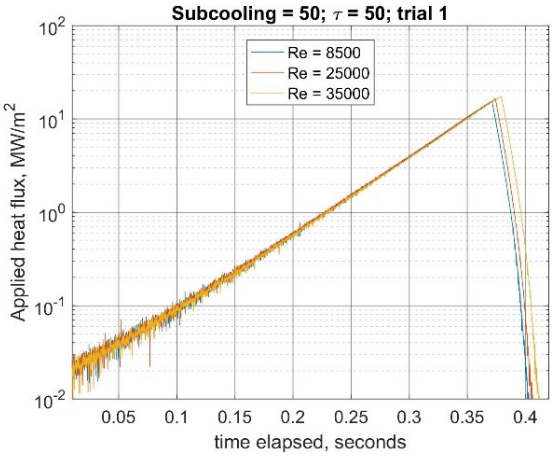
Subcooling = 50; τ = 50; trial 1
Applied heat flux, MW/m^2
time elapsed, seconds
Re = 8500
Re = 25000
Re = 35000

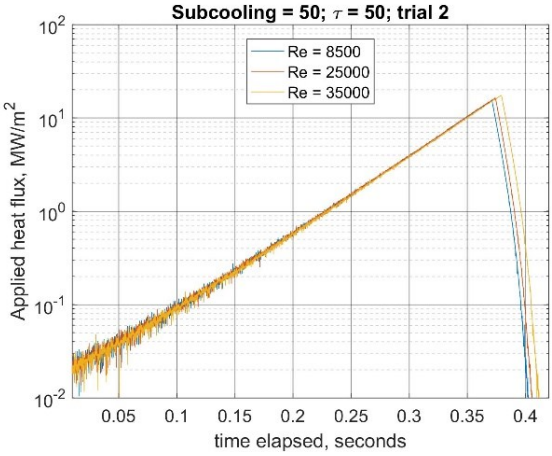
Subcooling = 50; τ = 50; trial 2
Applied heat flux, MW/m^2
time elapsed, seconds
Re = 8500
Re = 25000
Re = 35000

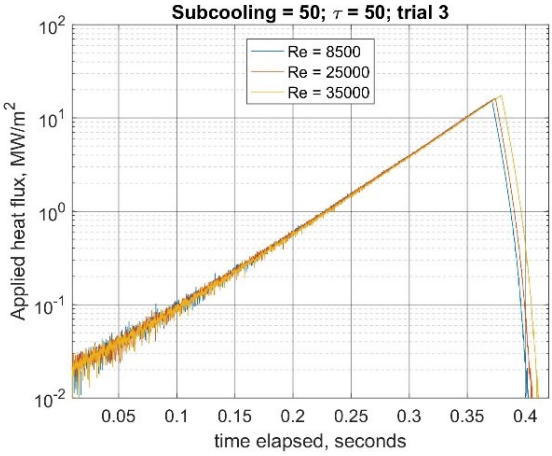
Subcooling = 50; τ = 50; trial 3
Applied heat flux, MW/m^2
time elapsed, seconds
Re = 8500
Re = 25000
Re = 35000

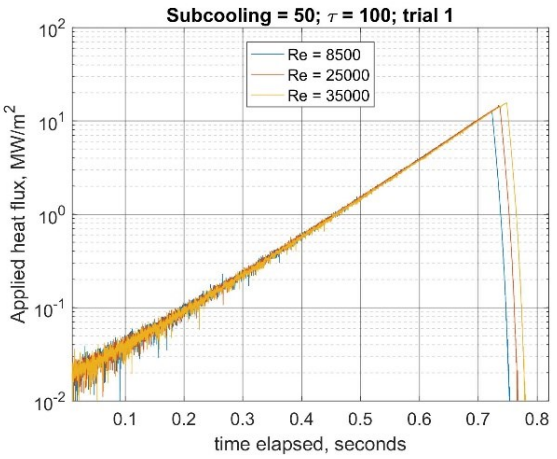
Subcooling = 50; τ = 100; trial 1
Re = 8500
Re = 25000
Re = 35000
Applied heat flux, MW/m2
time elapsed, seconds

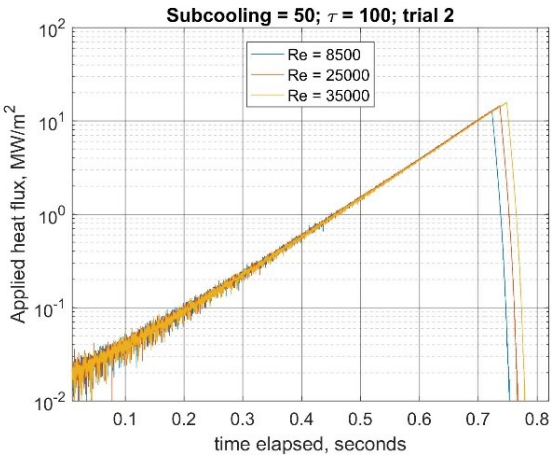
Subcooling = 50; τ = 100; trial 2
Re = 8500
Re = 25000
Re = 35000
Applied heat flux, MW/m2
time elapsed, seconds

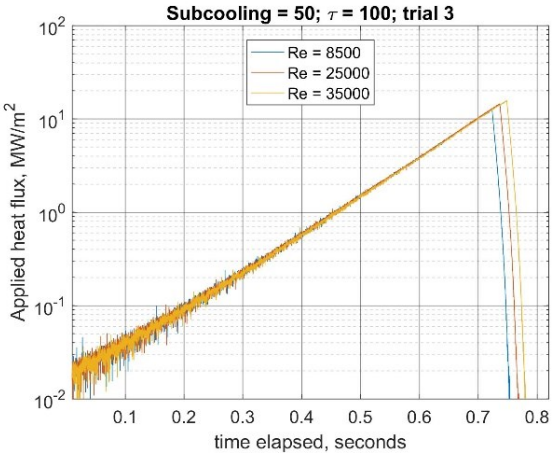
Subcooling = 50; τ = 100; trial 3
Re = 8500
Re = 25000
Re = 35000
Applied heat flux, MW/m2
time elapsed, seconds

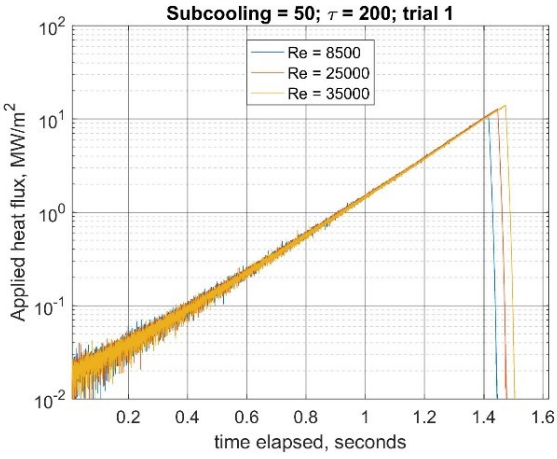
Subcooling = 50; τ = 200; trial 1
Re = 8500
Re = 25000
Re = 35000
Applied heat flux, MW/m2
time elapsed, seconds

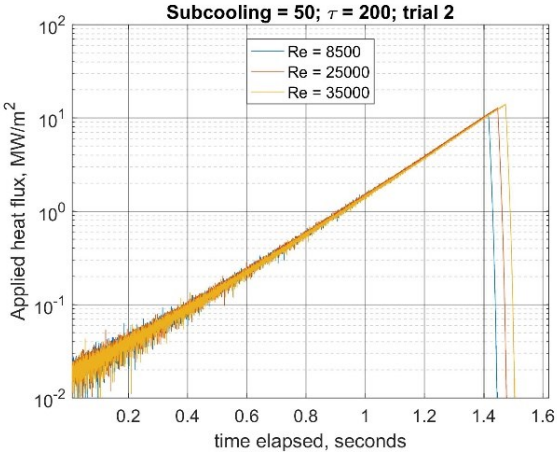
Subcooling = 50; τ = 200; trial 2
Re = 8500
Re = 25000
Re = 35000
Applied heat flux, MW/m2
time elapsed, seconds

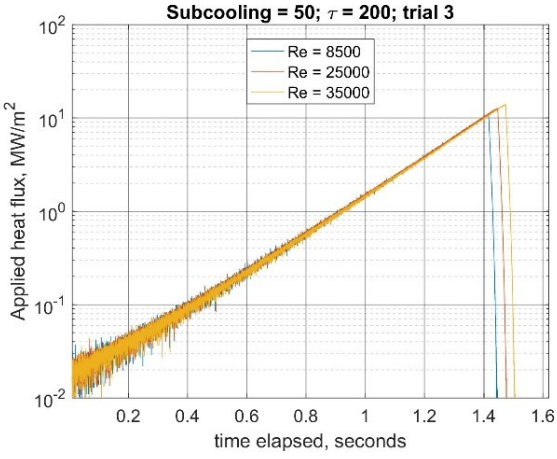
Subcooling = 50; τ = 200; trial 3
Re = 8500
Re = 25000
Re = 35000
Applied heat flux, MW/m2
time elapsed, seconds

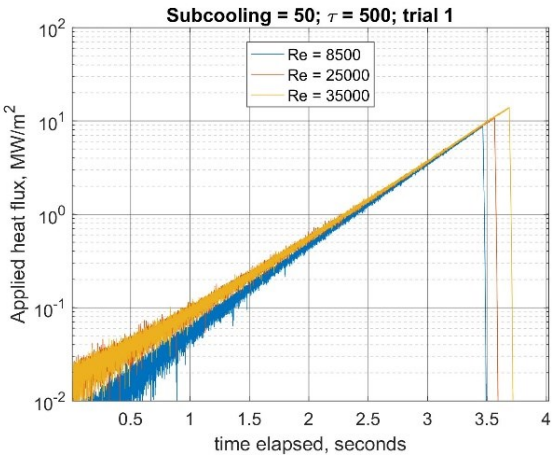
Subcooling = 50; τ = 500; trial 1
Re = 8500
Re = 25000
Re = 35000
Applied heat flux, MW/m^2
time elapsed, seconds

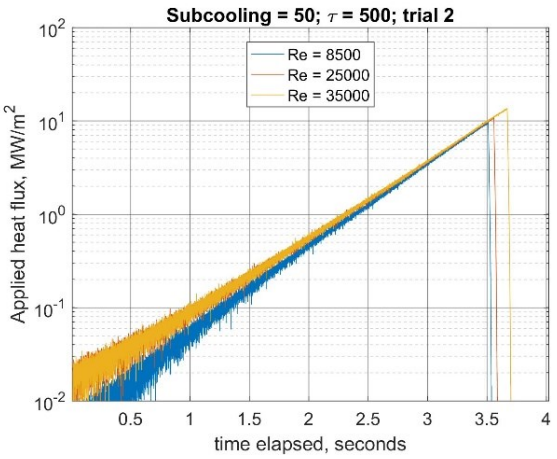
Subcooling = 50; τ = 500; trial 2
Re = 8500
Re = 25000
Re = 35000
Applied heat flux, MW/m^2
time elapsed, seconds

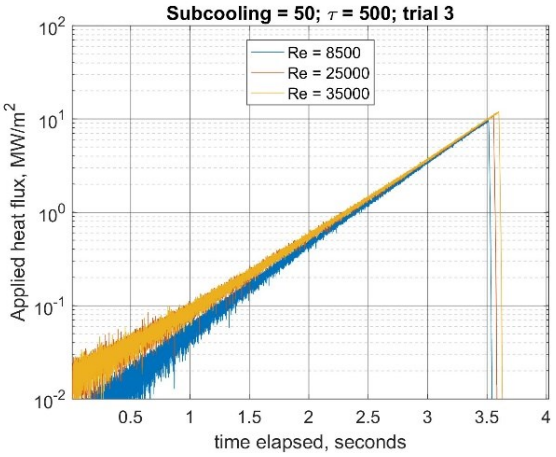
Subcooling = 50; τ = 500; trial 3
Re = 8500
Re = 25000
Re = 35000
Applied heat flux, MW/m^2
time elapsed, seconds

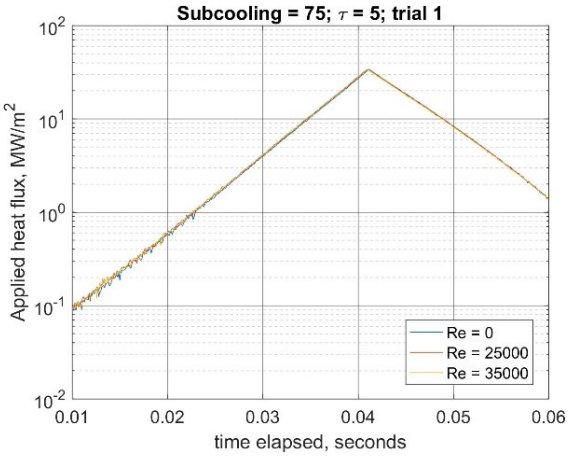
Subcooling = 75; τ = 5; trial 1
Re = 0
Re = 25000
Re = 35000
Applied heat flux, MW/m^2
time elapsed, seconds

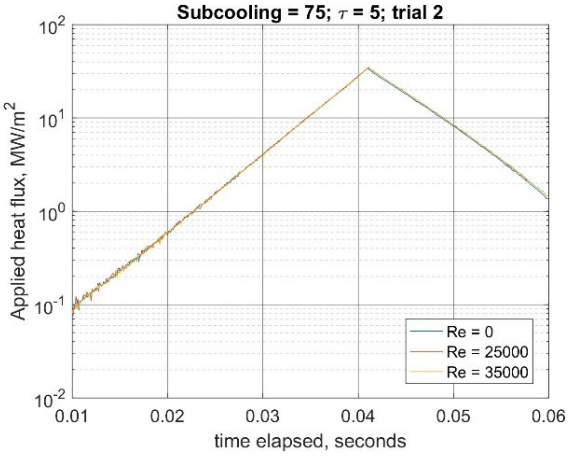
Subcooling = 75; τ = 5; trial 2
Re = 0
Re = 25000
Re = 35000
Applied heat flux, MW/m^2
time elapsed, seconds

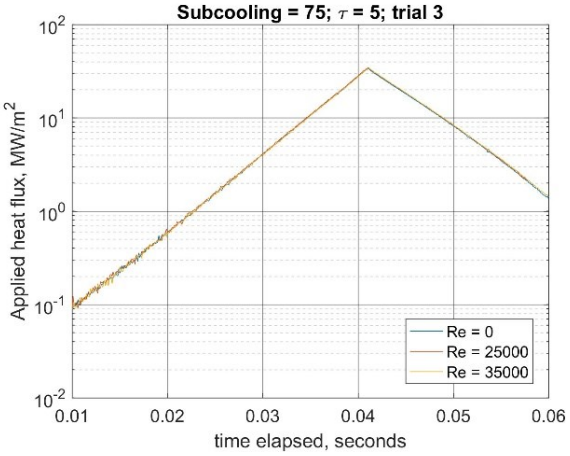
Subcooling = 75; τ = 5; trial 3
Re = 0
Re = 25000
Re = 35000
Applied heat flux, MW/m^2
time elapsed, seconds

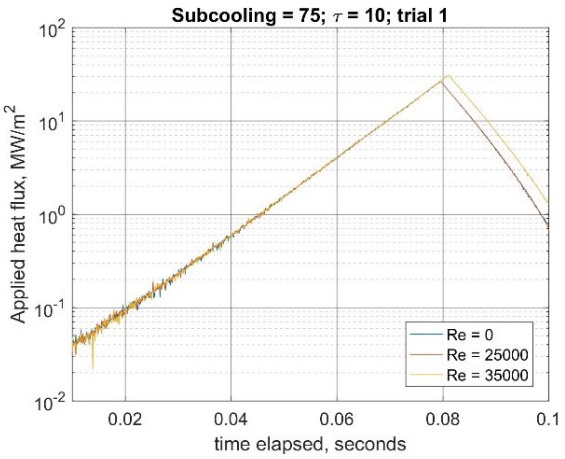
Subcooling = 75; τ = 10; trial 1
Applied heat flux, MW/m2
time elapsed, seconds
Re = 0
Re = 25000
Re = 35000

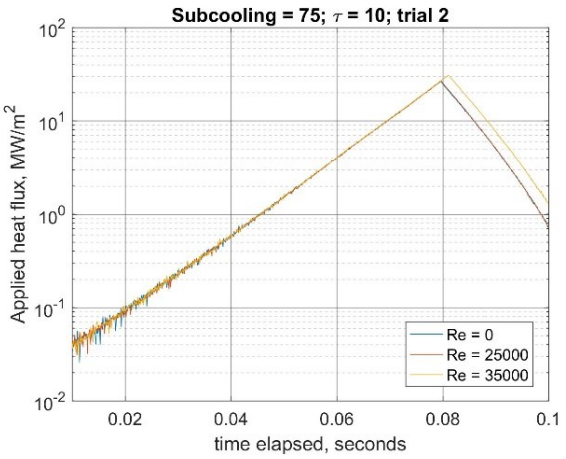
Subcooling = 75; τ = 10; trial 2
Applied heat flux, MW/m2
time elapsed, seconds
Re = 0
Re = 25000
Re = 35000

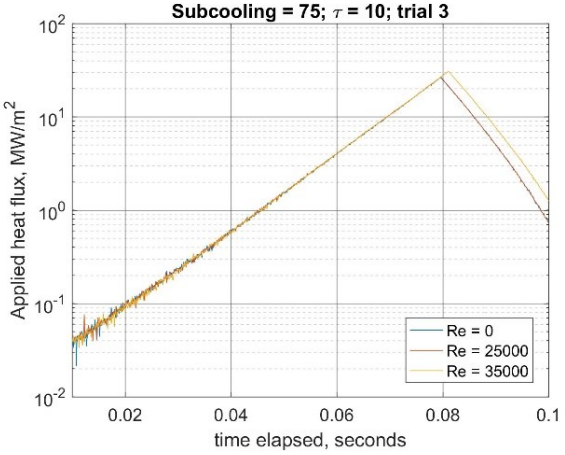
Subcooling = 75; τ = 10; trial 3
Applied heat flux, MW/m2
time elapsed, seconds
Re = 0
Re = 25000
Re = 35000

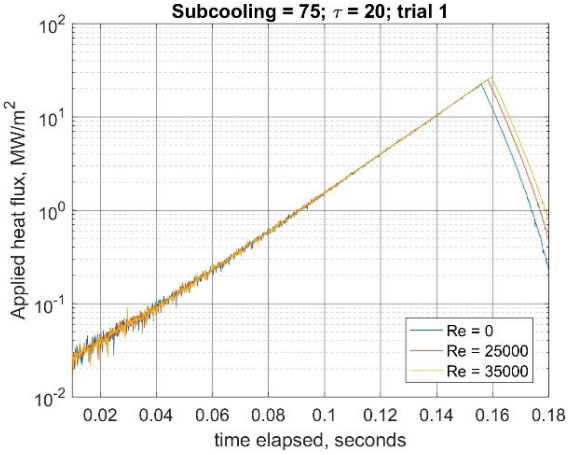
Subcooling = 75; τ = 20; trial 1
Applied heat flux, MW/m2
time elapsed, seconds
Re = 0
Re = 25000
Re = 35000

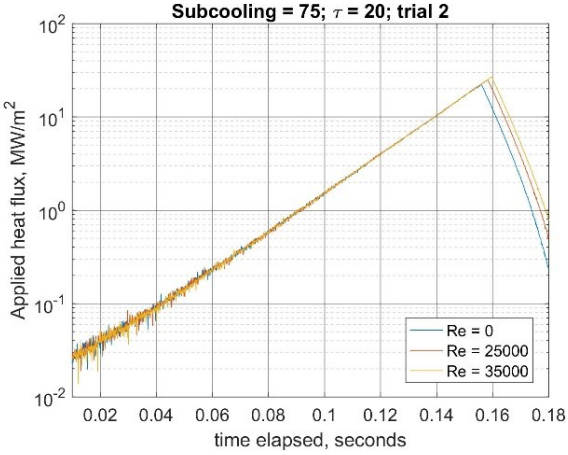
Subcooling = 75; τ = 20; trial 2
Applied heat flux, MW/m2
time elapsed, seconds
Re = 0
Re = 25000
Re = 35000

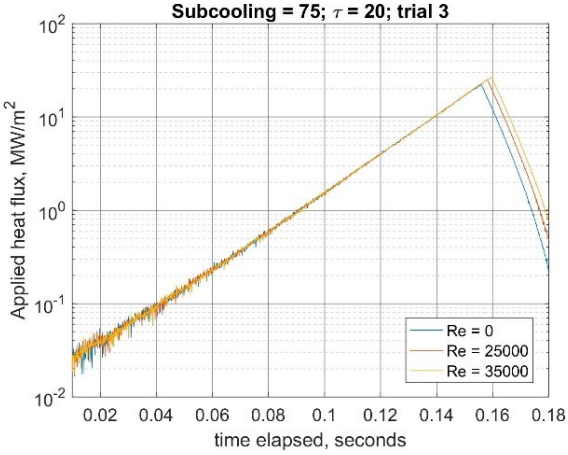
Subcooling = 75; τ = 20; trial 3
Applied heat flux, MW/m2
time elapsed, seconds
Re = 0
Re = 25000
Re = 35000

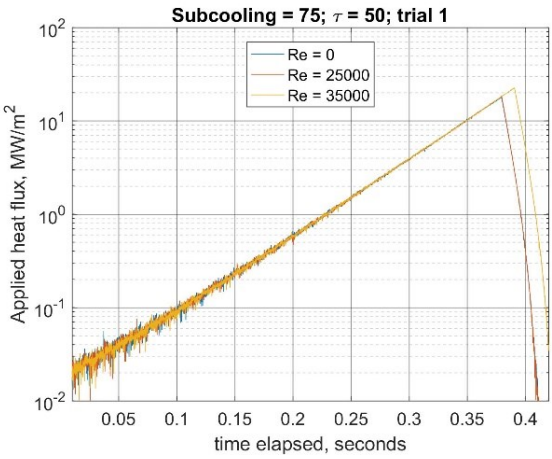
Subcooling = 75; τ = 50; trial 1
Re = 0
Re = 25000
Re = 35000
Applied heat flux, MW/m2
time elapsed, seconds

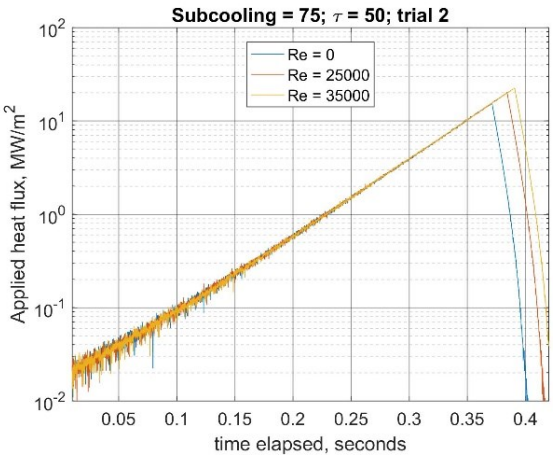
Subcooling = 75; τ = 50; trial 2
Re = 0
Re = 25000
Re = 35000
Applied heat flux, MW/m2
time elapsed, seconds

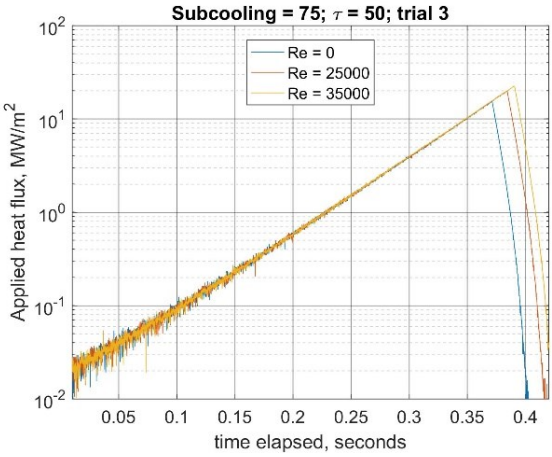
Subcooling = 75; τ = 50; trial 3
Re = 0
Re = 25000
Re = 35000
Applied heat flux, MW/m2
time elapsed, seconds

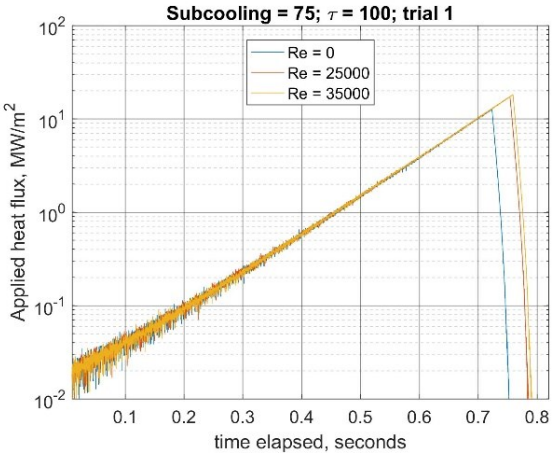
Subcooling = 75; τ = 100; trial 1
Re = 0
Re = 25000
Re = 35000
Applied heat flux, MW/m2
time elapsed, seconds

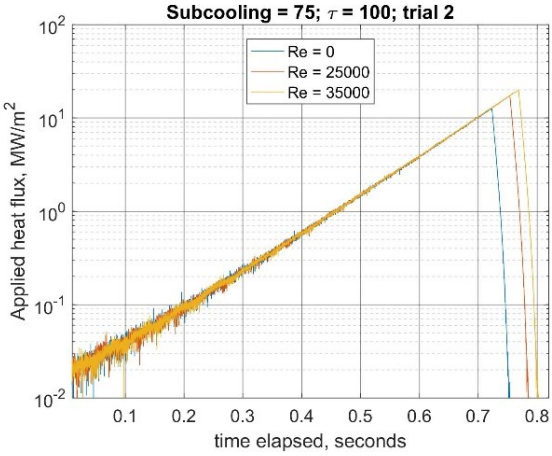
Subcooling = 75; τ = 100; trial 2
Re = 0
Re = 25000
Re = 35000
Applied heat flux, MW/m2
time elapsed, seconds

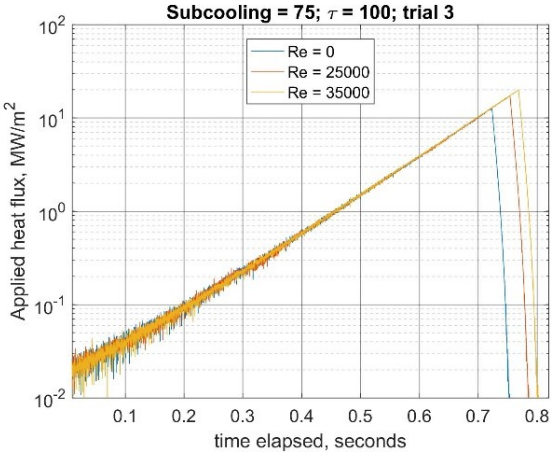
Subcooling = 75; τ = 100; trial 3
Re = 0
Re = 25000
Re = 35000
Applied heat flux, MW/m2
time elapsed, seconds

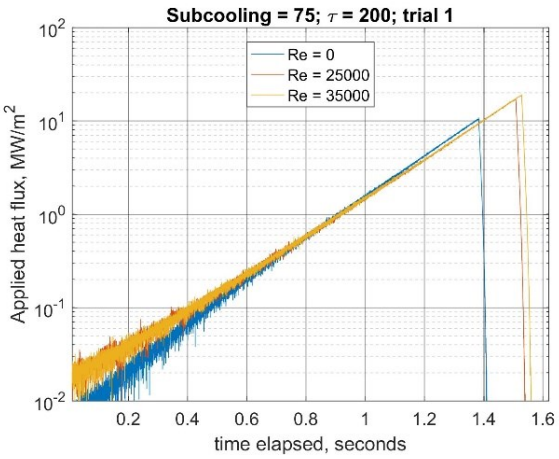
Subcooling = 75; τ = 200; trial 1
Re = 0
Re = 25000
Re = 35000
Applied heat flux, MW/m2
time elapsed, seconds

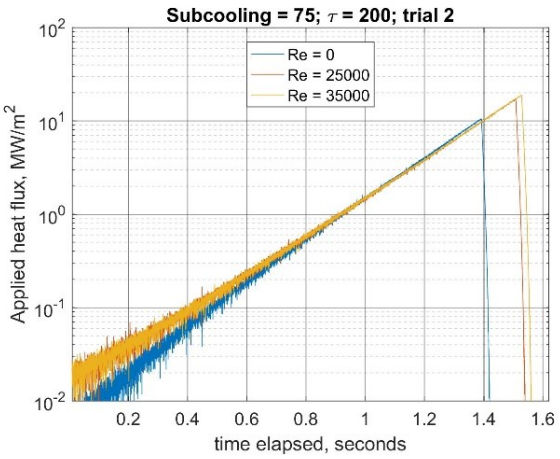
Subcooling = 75; τ = 200; trial 2
Re = 0
Re = 25000
Re = 35000
Applied heat flux, MW/m2
time elapsed, seconds

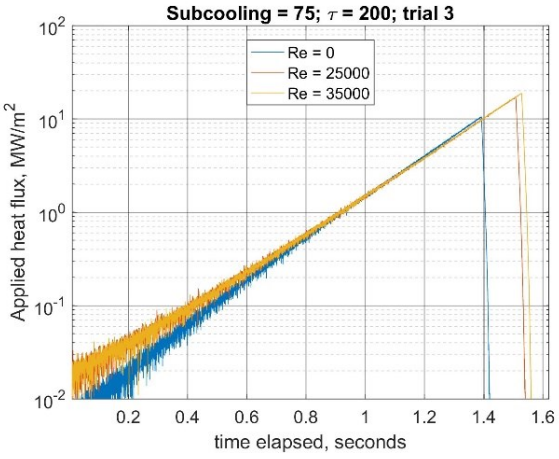
Subcooling = 75; τ = 200; trial 3
Re = 0
Re = 25000
Re = 35000
Applied heat flux, MW/m2
time elapsed, seconds

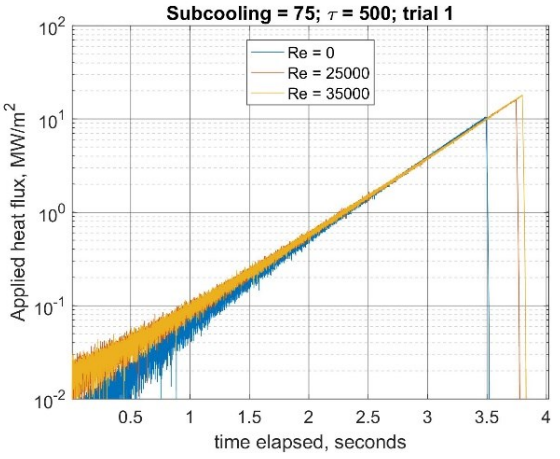
Subcooling = 75; τ = 500; trial 1
Re = 0
Re = 25000
Re = 35000
Applied heat flux, MW/m2
time elapsed, seconds

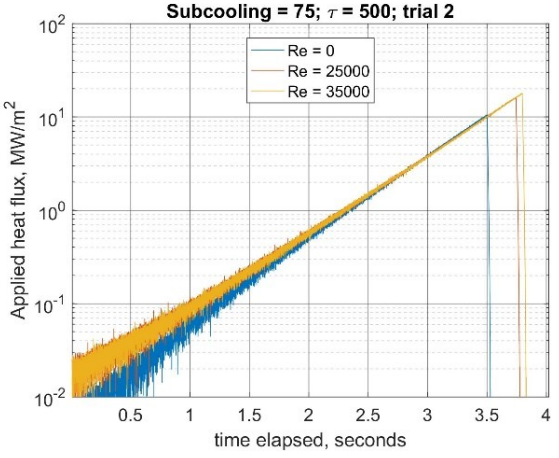
Subcooling = 75; τ = 500; trial 2
Re = 0
Re = 25000
Re = 35000
Applied heat flux, MW/m2
time elapsed, seconds

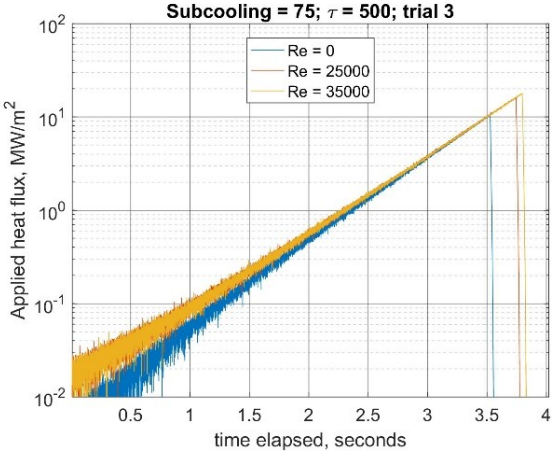
Subcooling = 75; τ = 500; trial 3
Re = 0
Re = 25000
Re = 35000
Applied heat flux, MW/m2
time elapsed, seconds

Appendix C. Boiling curves

Boiling curves (heat flux to water vs. wall superheat) for all tests are presented below. Each plot represents a unique combination of subcooling and escalation period. Because each test was repeated three times, distinct plots for three different "trials" are given.

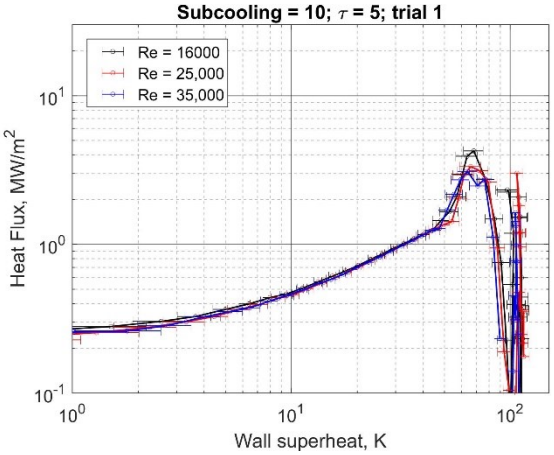

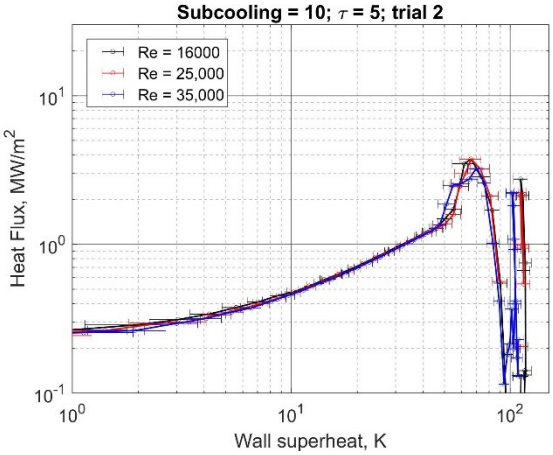

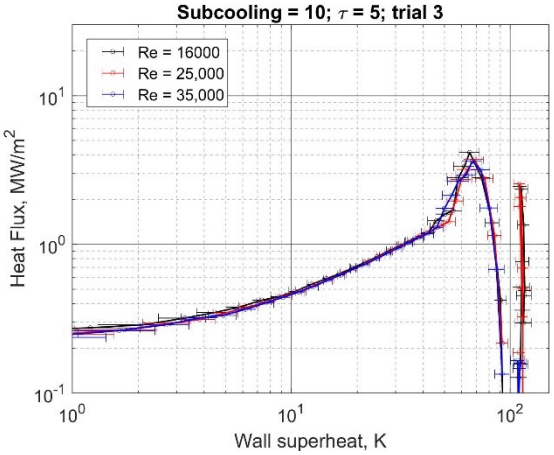

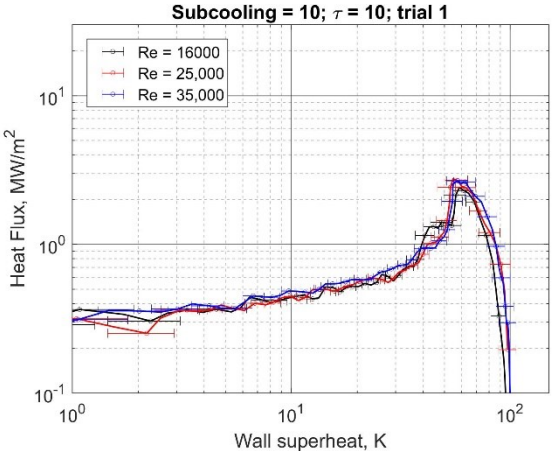

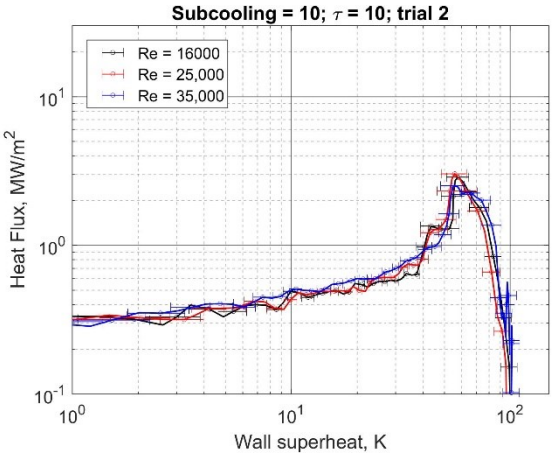

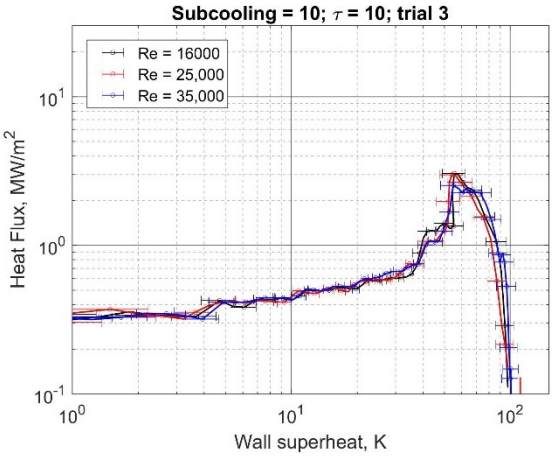

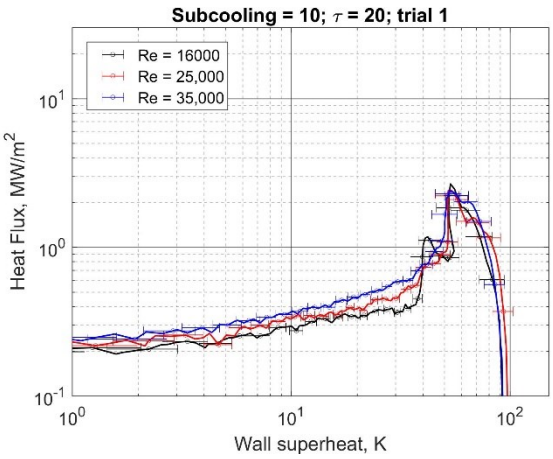
Subcooling = 10; τ = 20; trial 1
Re = 16000
Re = 25,000
Re = 35,000
Heat Flux, MW/m2
Wall superheat, K

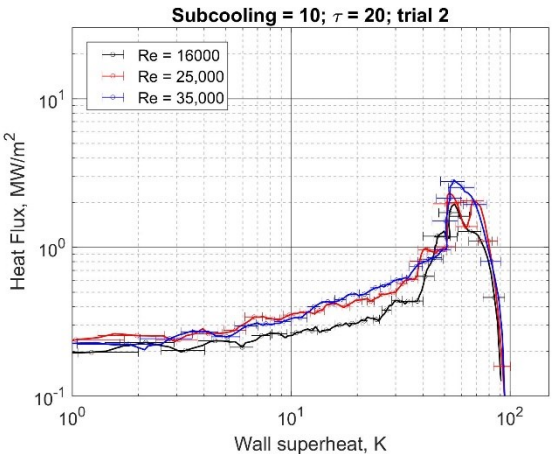
Subcooling = 10; τ = 20; trial 2
Re = 16000
Re = 25,000
Re = 35,000
Heat Flux, MW/m2
Wall superheat, K

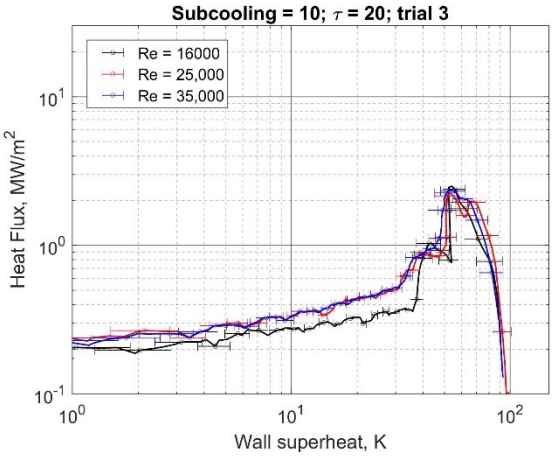
Subcooling = 10; τ = 20; trial 3
Re = 16000
Re = 25,000
Re = 35,000
Heat Flux, MW/m2
Wall superheat, K

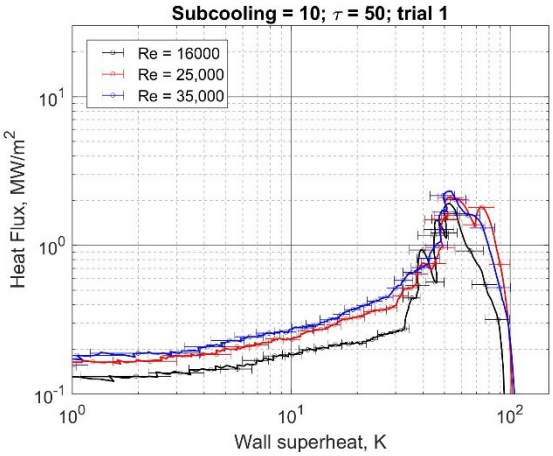
Subcooling = 10; τ = 50; trial 1
Re = 16000
Re = 25,000
Re = 35,000
Heat Flux, MW/m2
Wall superheat, K

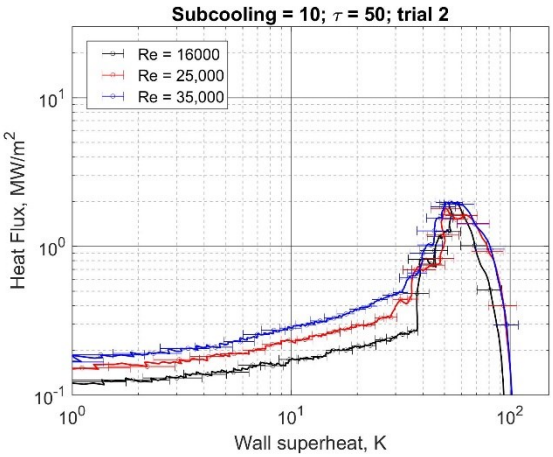
Subcooling = 10; τ = 50; trial 2
Re = 16000
Re = 25,000
Re = 35,000
Heat Flux, MW/m2
Wall superheat, K

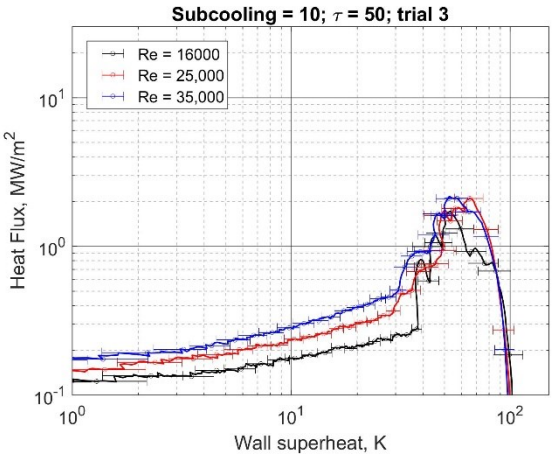
Subcooling = 10; τ = 50; trial 3
Re = 16000
Re = 25,000
Re = 35,000
Heat Flux, MW/m2
Wall superheat, K

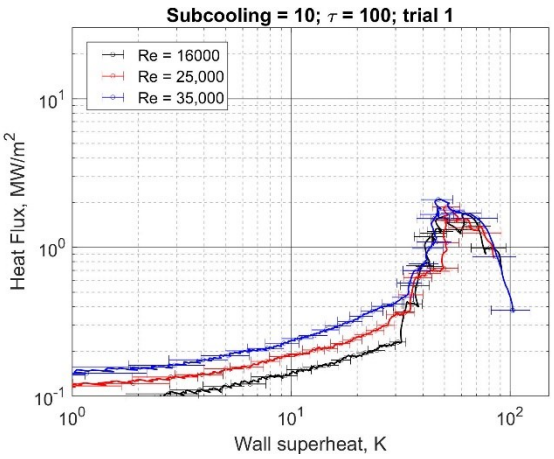
Subcooling = 10; τ = 100; trial 1
Re = 16000
Re = 25,000
Re = 35,000
Heat Flux, MW/m2
Wall superheat, K

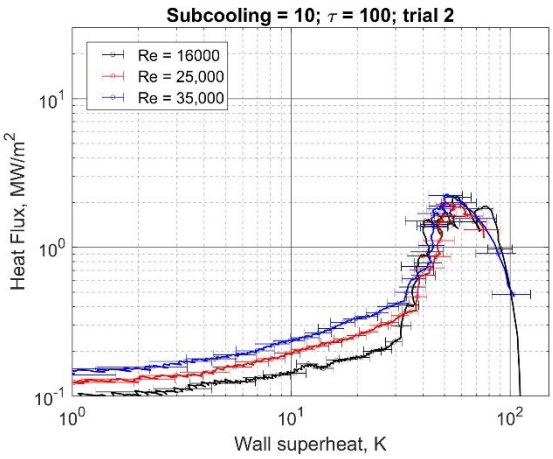
Subcooling = 10; τ = 100; trial 2
Re = 16000
Re = 25,000
Re = 35,000
Heat Flux, MW/m2
Wall superheat, K

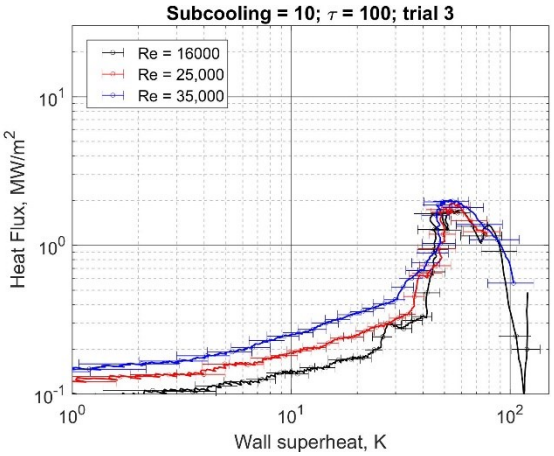
Subcooling = 10; τ = 100; trial 3
Re = 16000
Re = 25,000
Re = 35,000
Heat Flux, MW/m2
Wall superheat, K

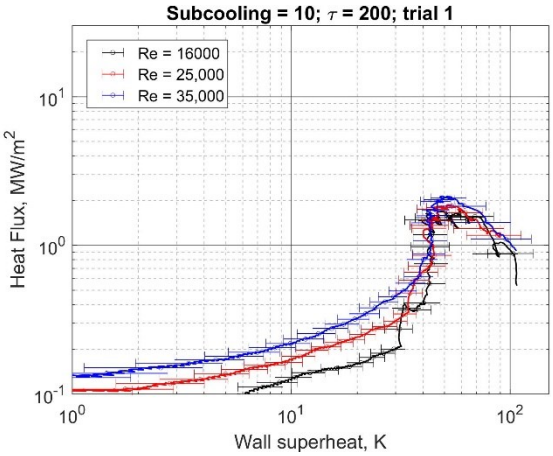
Subcooling = 10; τ = 200; trial 1
Re = 16000
Re = 25,000
Re = 35,000
Heat Flux, MW/m2
Wall superheat, K

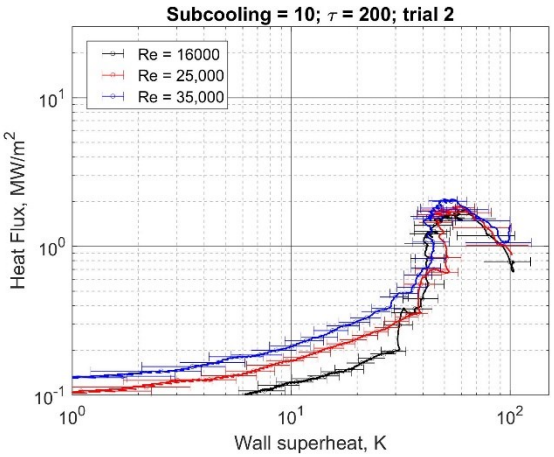
Subcooling = 10; τ = 200; trial 2
Re = 16000
Re = 25,000
Re = 35,000
Heat Flux, MW/m2
Wall superheat, K

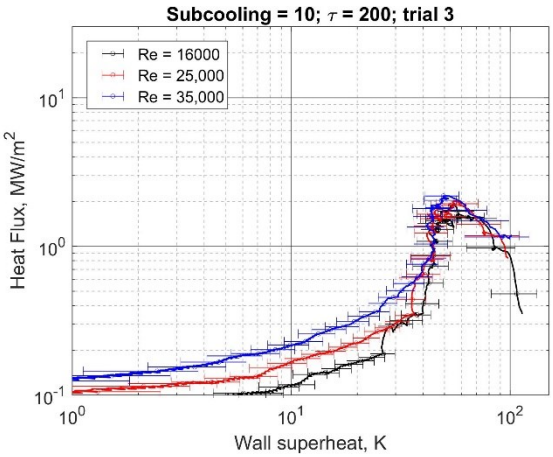
Subcooling = 10; τ = 200; trial 3
Re = 16000
Re = 25,000
Re = 35,000
Heat Flux, MW/m2
Wall superheat, K

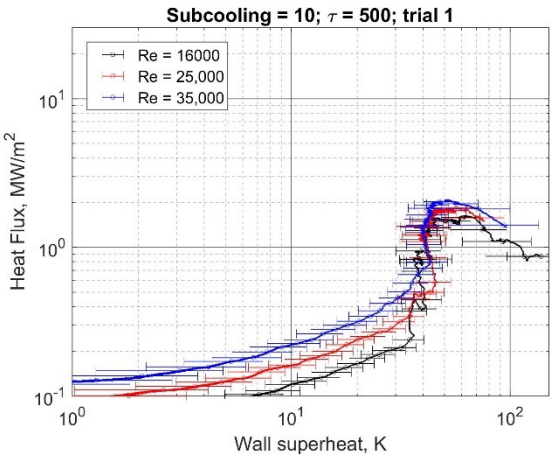
Subcooling = 10; τ = 500; trial 1
Re = 16000
Re = 25,000
Re = 35,000
Heat Flux, MW/m^2
Wall superheat, K

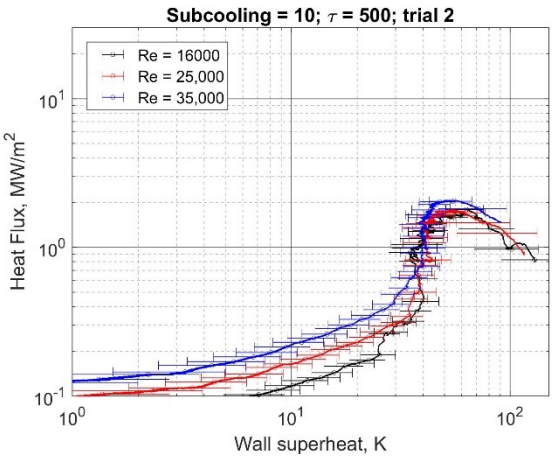
Subcooling = 10; τ = 500; trial 2
Re = 16000
Re = 25,000
Re = 35,000
Heat Flux, MW/m^2
Wall superheat, K

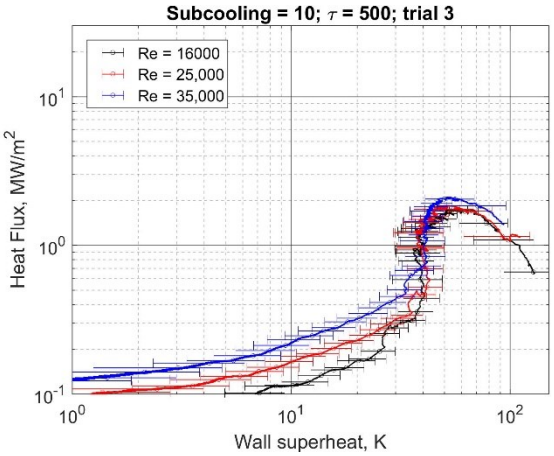
Subcooling = 10; τ = 500; trial 3
Re = 16000
Re = 25,000
Re = 35,000
Heat Flux, MW/m^2
Wall superheat, K

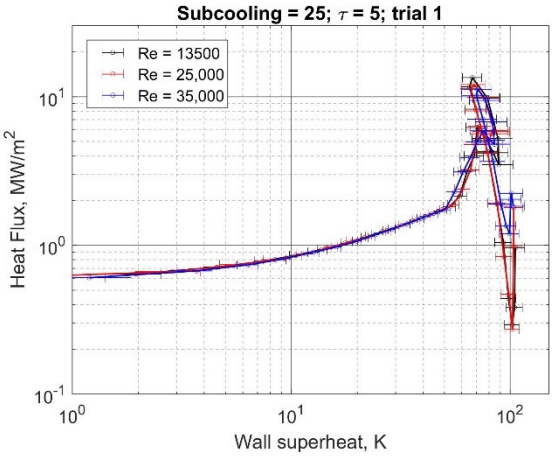
Subcooling = 25; τ = 5; trial 1
Re = 13500
Re = 25,000
Re = 35,000
Heat Flux, MW/m^2
Wall superheat, K

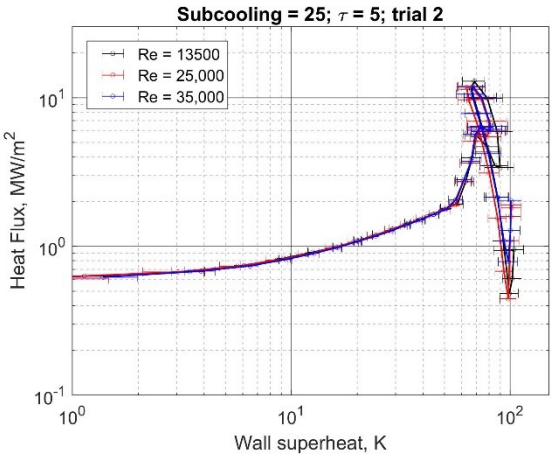
Subcooling = 25; τ = 5; trial 2
Re = 13500
Re = 25,000
Re = 35,000
Heat Flux, MW/m^2
Wall superheat, K

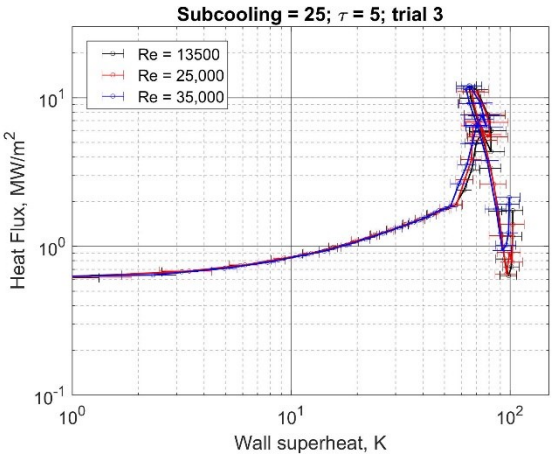
Subcooling = 25; τ = 5; trial 3
Re = 13500
Re = 25,000
Re = 35,000
Heat Flux, MW/m^2
Wall superheat, K

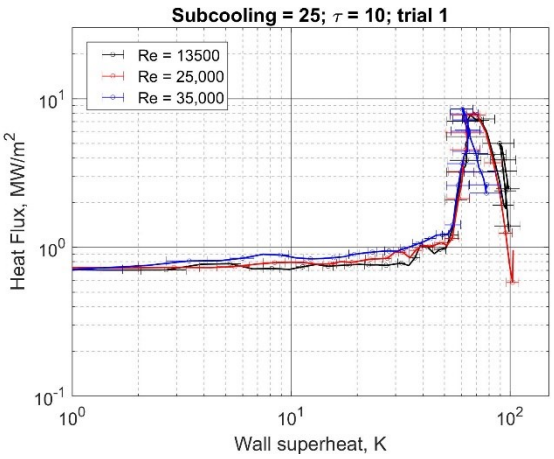
Subcooling = 25; τ = 10; trial 1
Re = 13500
Re = 25,000
Re = 35,000
Heat Flux, MW/m2
Wall superheat, K

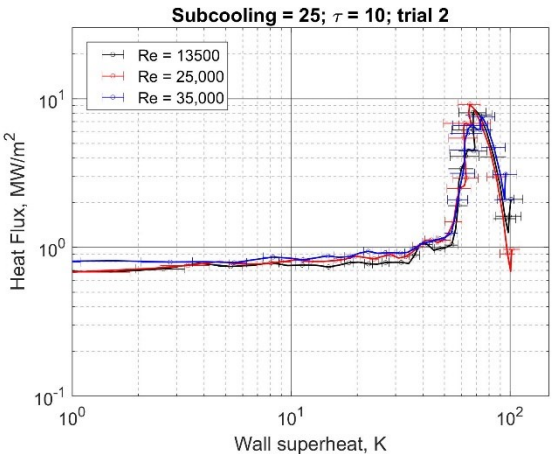
Subcooling = 25; τ = 10; trial 2
Re = 13500
Re = 25,000
Re = 35,000
Heat Flux, MW/m2
Wall superheat, K

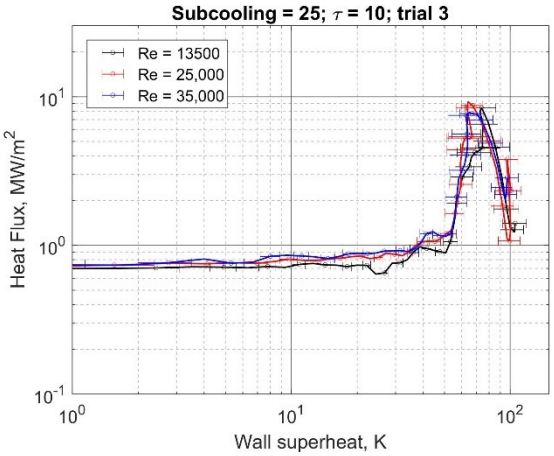
Subcooling = 25; τ = 10; trial 3
Re = 13500
Re = 25,000
Re = 35,000
Heat Flux, MW/m2
Wall superheat, K

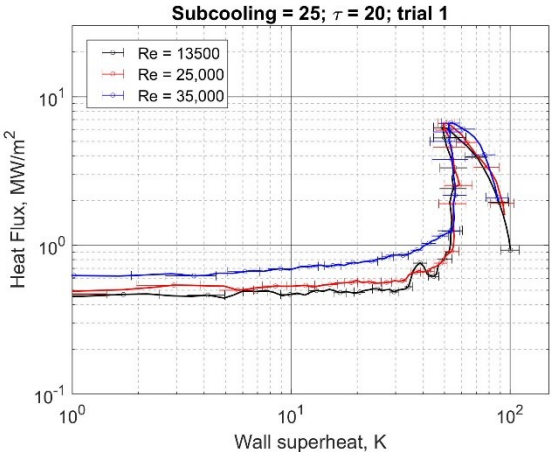
Subcooling = 25; τ = 20; trial 1
Re = 13500
Re = 25,000
Re = 35,000
Heat Flux, MW/m2
Wall superheat, K

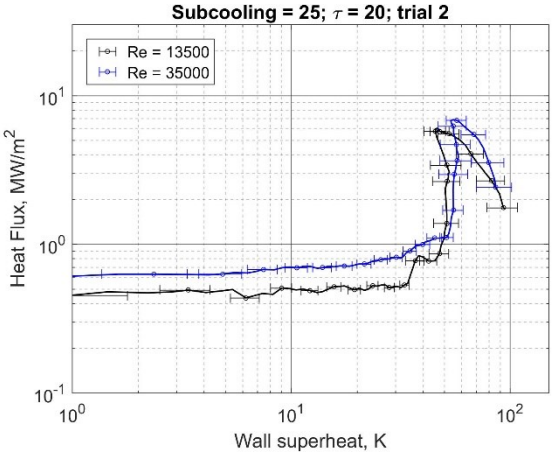
Subcooling = 25; τ = 20; trial 2
Re = 13500
Re = 35000
Heat Flux, MW/m2
Wall superheat, K

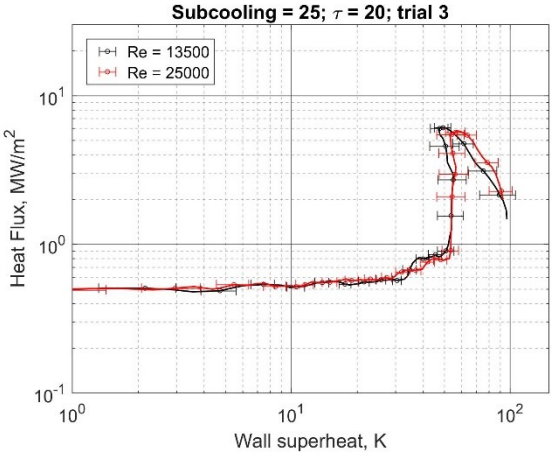
Subcooling = 25; τ = 20; trial 3
Re = 13500
Re = 25000
Heat Flux, MW/m2
Wall superheat, K

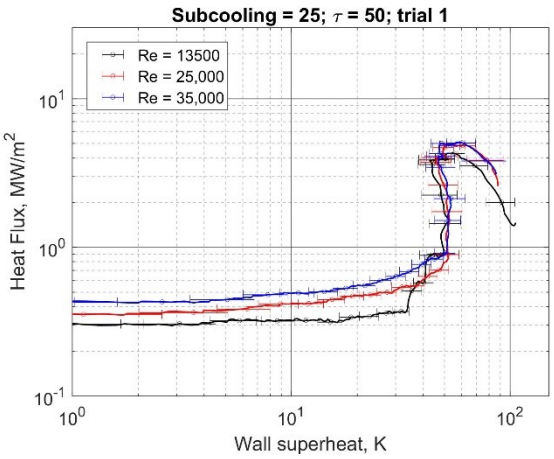
Subcooling = 25; τ = 50; trial 1
Re = 13500
Re = 25,000
Re = 35,000
Heat Flux, MW/m2
Wall superheat, K

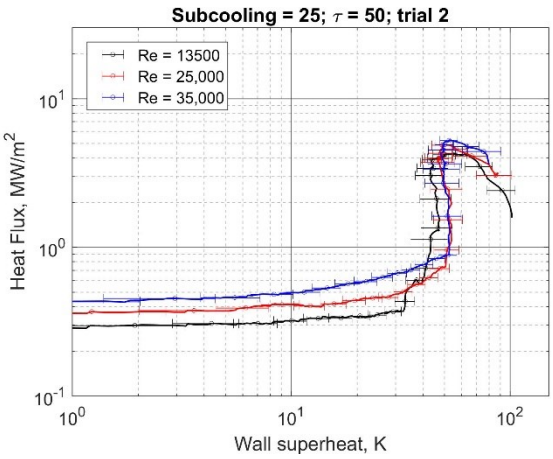
Subcooling = 25; τ = 50; trial 2
Re = 13500
Re = 25,000
Re = 35,000
Heat Flux, MW/m2
Wall superheat, K

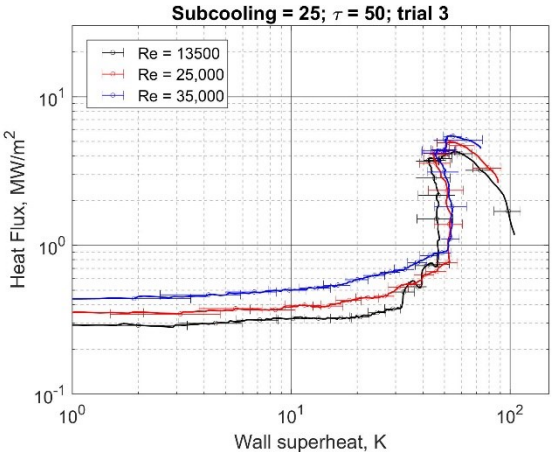
Subcooling = 25; τ = 50; trial 3
Re = 13500
Re = 25,000
Re = 35,000
Heat Flux, MW/m2
Wall superheat, K

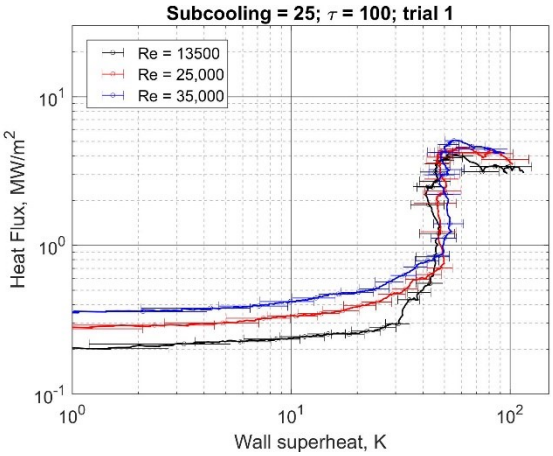
Subcooling = 25; τ = 100; trial 1
Re = 13500
Re = 25,000
Re = 35,000
Heat Flux, MW/m2
Wall superheat, K

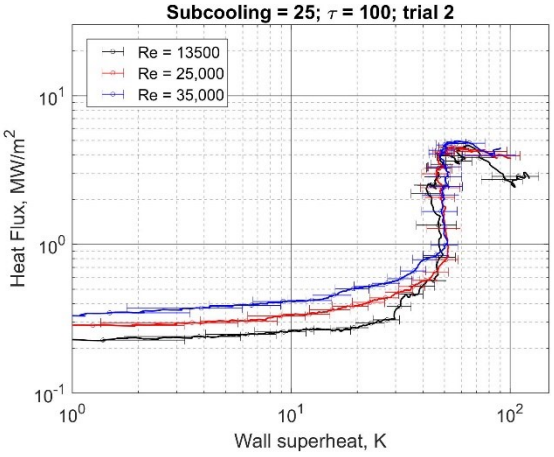
Subcooling = 25; τ = 100; trial 2
Re = 13500
Re = 25,000
Re = 35,000
Heat Flux, MW/m2
Wall superheat, K

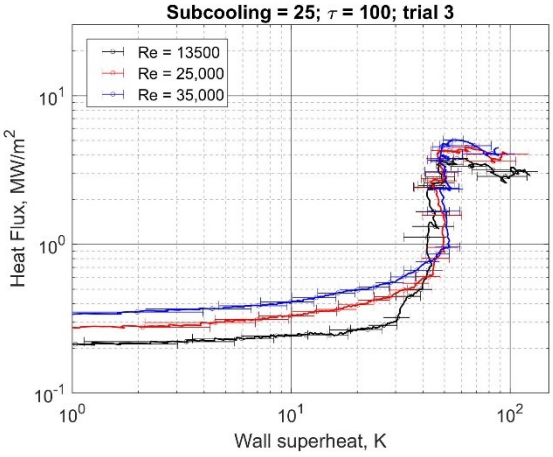
Subcooling = 25; τ = 100; trial 3
Re = 13500
Re = 25,000
Re = 35,000
Heat Flux, MW/m2
Wall superheat, K

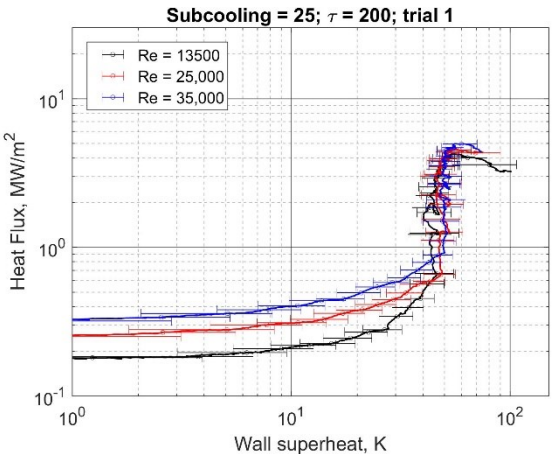
Subcooling = 25; τ = 200; trial 1
Re = 13500
Re = 25,000
Re = 35,000
Heat Flux, MW/m2
Wall superheat, K

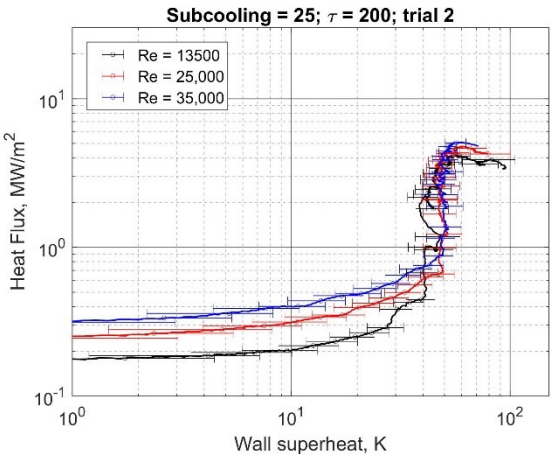
Subcooling = 25; τ = 200; trial 2
Re = 13500
Re = 25,000
Re = 35,000
Heat Flux, MW/m2
Wall superheat, K

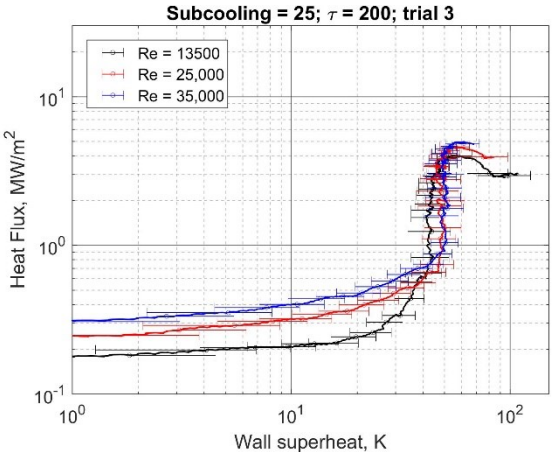
Subcooling = 25; τ = 200; trial 3
Re = 13500
Re = 25,000
Re = 35,000
Heat Flux, MW/m2
Wall superheat, K

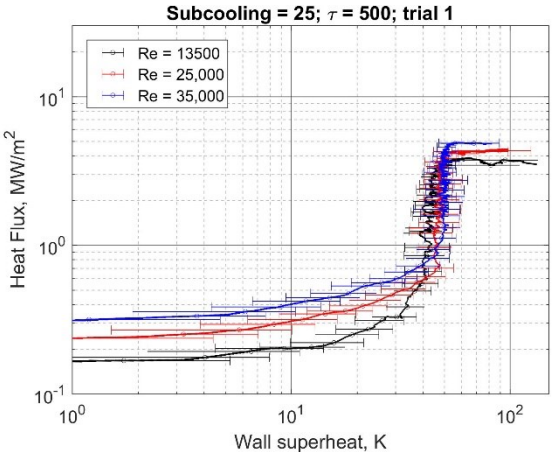
Subcooling = 25; τ = 500; trial 1
Re = 13500
Re = 25,000
Re = 35,000
Heat Flux, MW/m2
Wall superheat, K

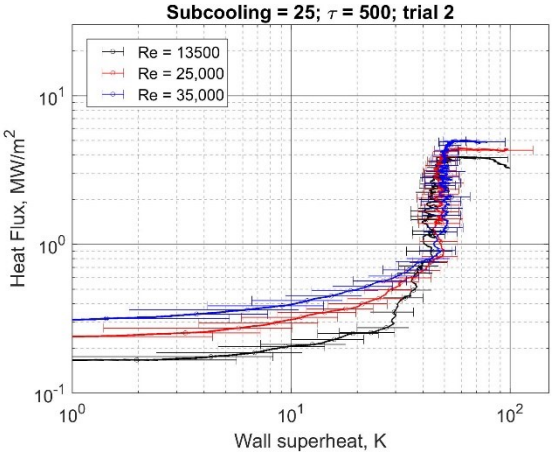
Subcooling = 25; τ = 500; trial 2
Re = 13500
Re = 25,000
Re = 35,000
Heat Flux, MW/m2
Wall superheat, K

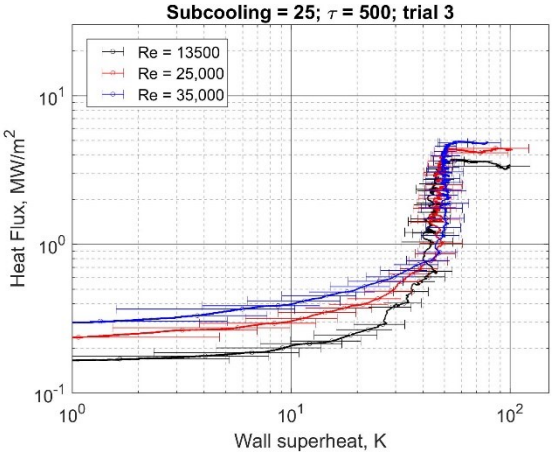
Subcooling = 25; τ = 500; trial 3
Re = 13500
Re = 25,000
Re = 35,000
Heat Flux, MW/m2
Wall superheat, K

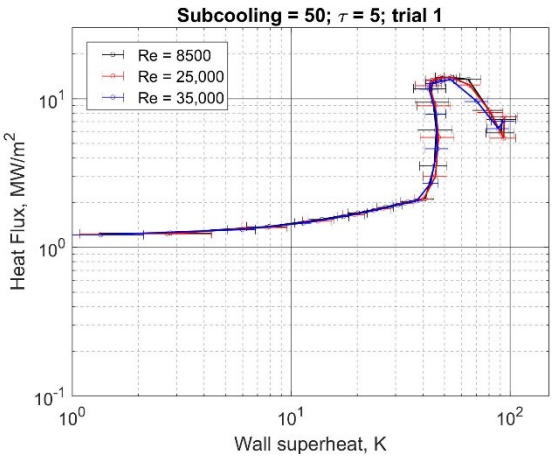
Subcooling = 50; τ = 5; trial 1
Re = 8500
Re = 25,000
Re = 35,000
Heat Flux, MW/m2
Wall superheat, K

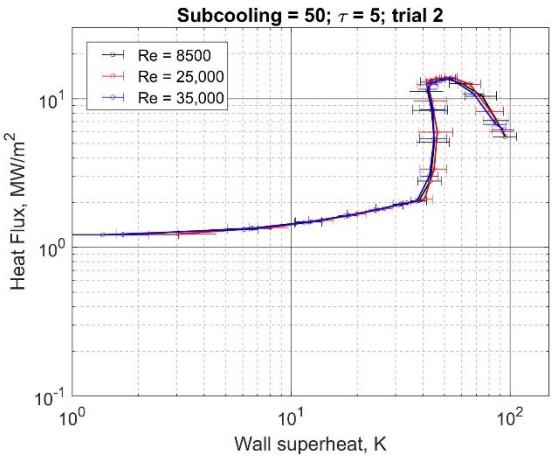
Subcooling = 50; τ = 5; trial 2
Re = 8500
Re = 25,000
Re = 35,000
Heat Flux, MW/m2
Wall superheat, K

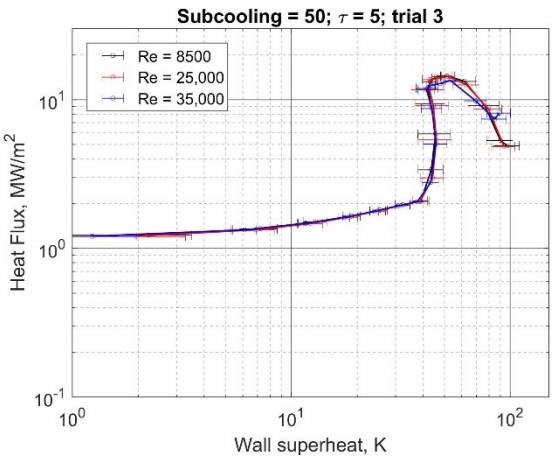
Subcooling = 50; τ = 5; trial 3
Re = 8500
Re = 25,000
Re = 35,000
Heat Flux, MW/m2
Wall superheat, K

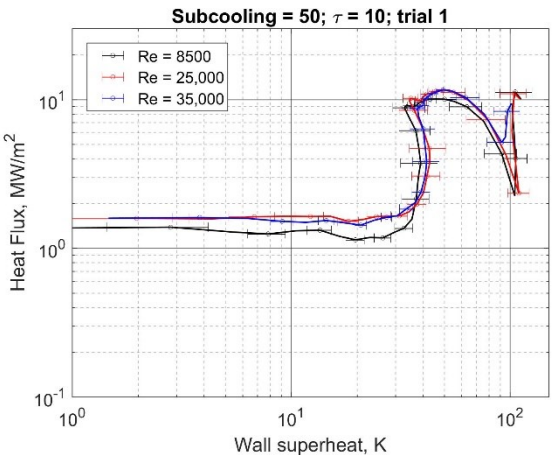
Subcooling = 50; τ = 10; trial 1
Re = 8500
Re = 25,000
Re = 35,000
Heat Flux, MW/m2
Wall superheat, K

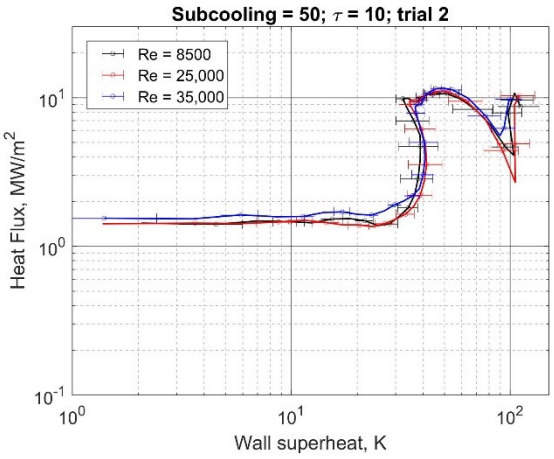
Subcooling = 50; τ = 10; trial 2
Re = 8500
Re = 25,000
Re = 35,000
Heat Flux, MW/m2
Wall superheat, K

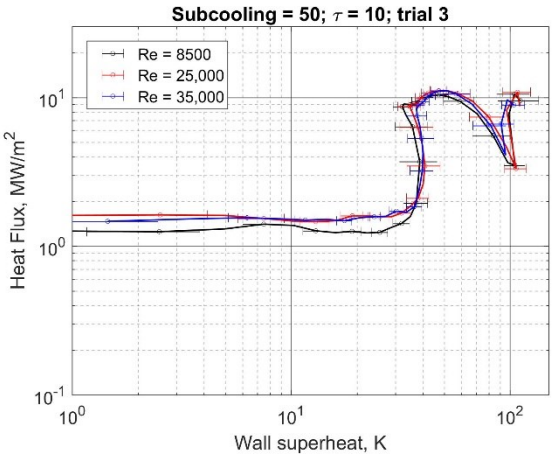
Subcooling = 50; τ = 10; trial 3
Re = 8500
Re = 25,000
Re = 35,000
Heat Flux, MW/m2
Wall superheat, K

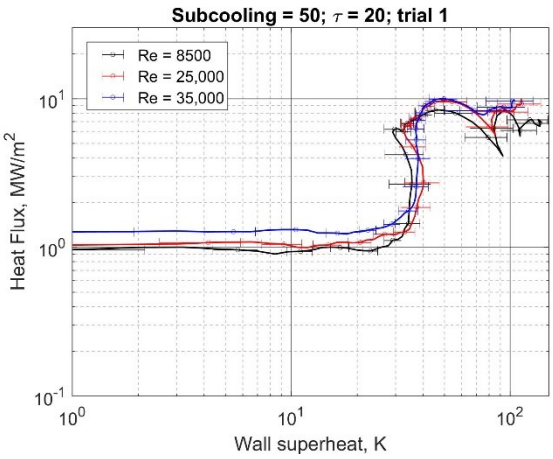
Subcooling = 50; τ = 20; trial 1
Re = 8500
Re = 25,000
Re = 35,000
Heat Flux, MW/m2
Wall superheat, K

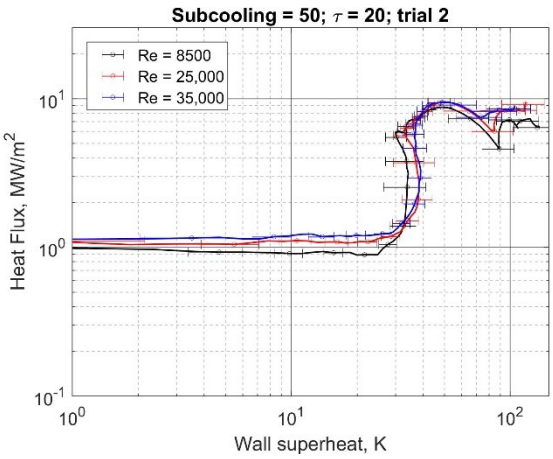
Subcooling = 50; τ = 20; trial 2
Re = 8500
Re = 25,000
Re = 35,000
Heat Flux, MW/m2
Wall superheat, K

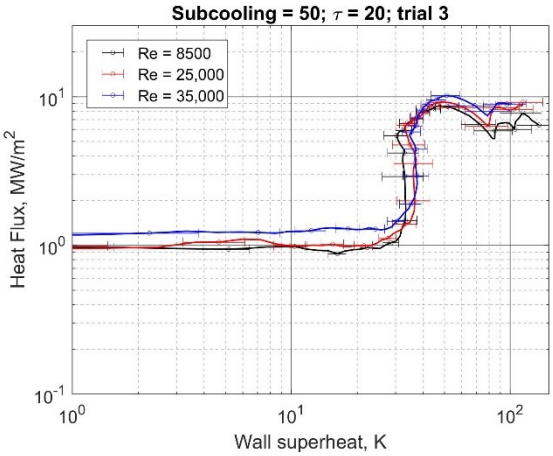
Subcooling = 50; τ = 20; trial 3
Re = 8500
Re = 25,000
Re = 35,000
Heat Flux, MW/m2
Wall superheat, K

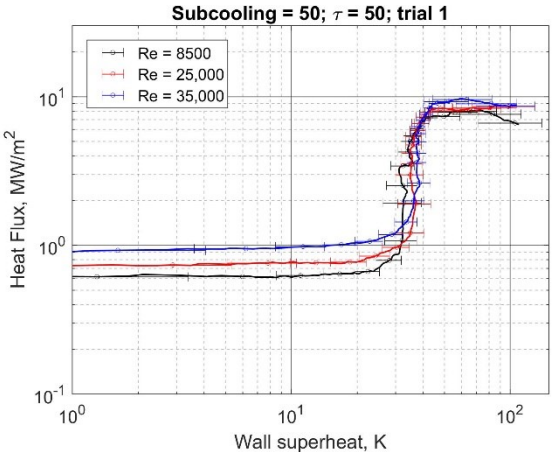
Subcooling = 50; τ = 50; trial 1
Re = 8500
Re = 25,000
Re = 35,000
Heat Flux, MW/m2
Wall superheat, K

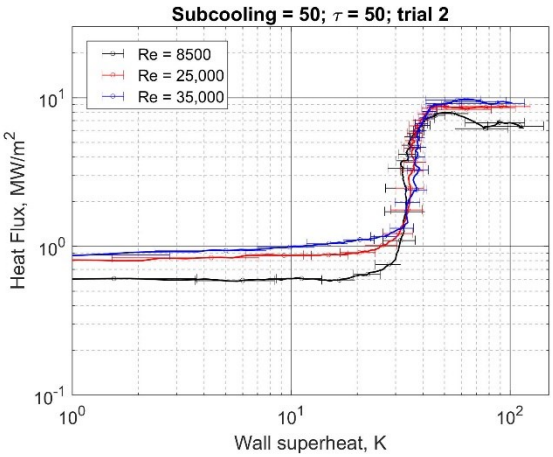
Subcooling = 50; τ = 50; trial 2
Re = 8500
Re = 25,000
Re = 35,000
Heat Flux, MW/m2
Wall superheat, K

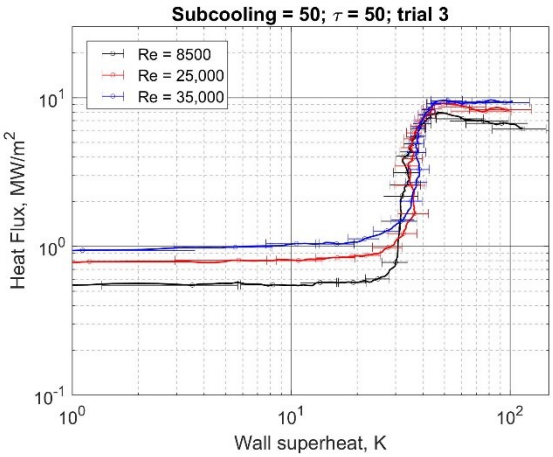
Subcooling = 50; τ = 50; trial 3
Re = 8500
Re = 25,000
Re = 35,000
Heat Flux, MW/m2
Wall superheat, K

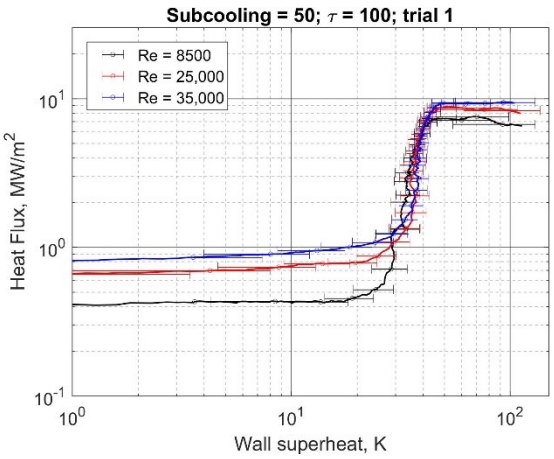
Subcooling = 50; τ = 100; trial 1
Re = 8500
Re = 25,000
Re = 35,000
Heat Flux, MW/m2
Wall superheat, K

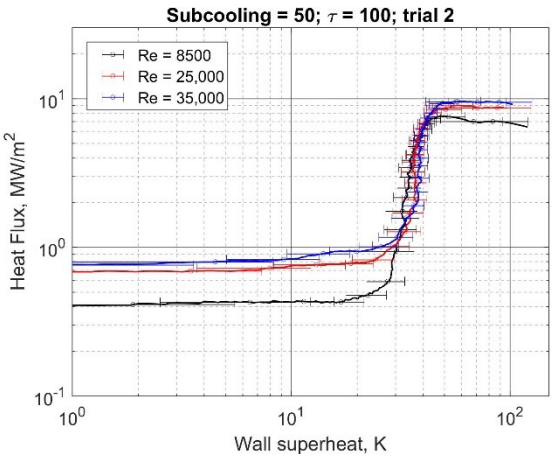
Subcooling = 50; τ = 100; trial 2
Re = 8500
Re = 25,000
Re = 35,000
Heat Flux, MW/m2
Wall superheat, K

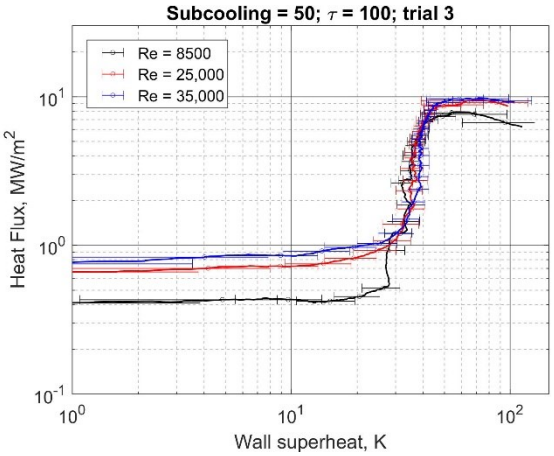
Subcooling = 50; τ = 100; trial 3
Re = 8500
Re = 25,000
Re = 35,000
Heat Flux, MW/m2
Wall superheat, K

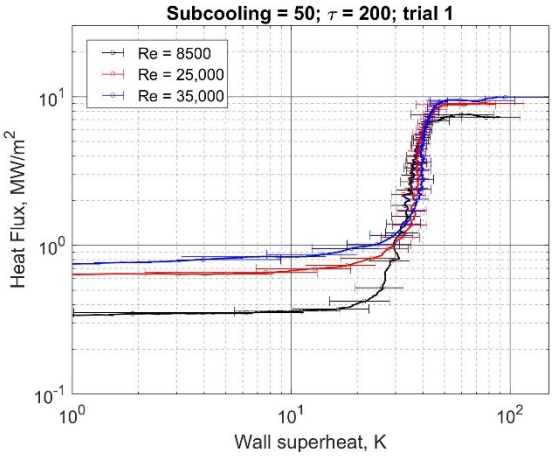
Subcooling = 50; τ = 200; trial 1
Re = 8500
Re = 25,000
Re = 35,000
Heat Flux, MW/m2
Wall superheat, K

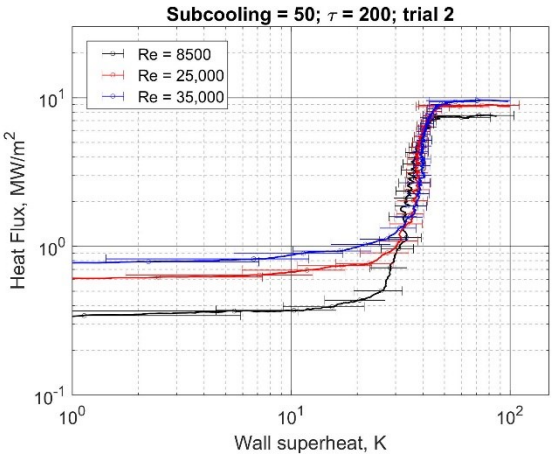
Subcooling = 50; τ = 200; trial 2
Re = 8500
Re = 25,000
Re = 35,000
Heat Flux, MW/m2
Wall superheat, K

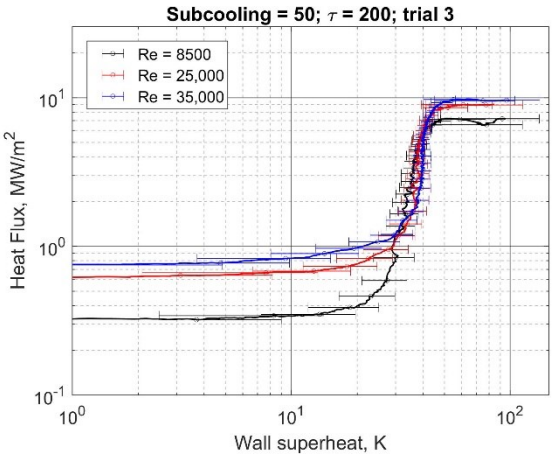
Subcooling = 50; τ = 200; trial 3
Re = 8500
Re = 25,000
Re = 35,000
Heat Flux, MW/m2
Wall superheat, K

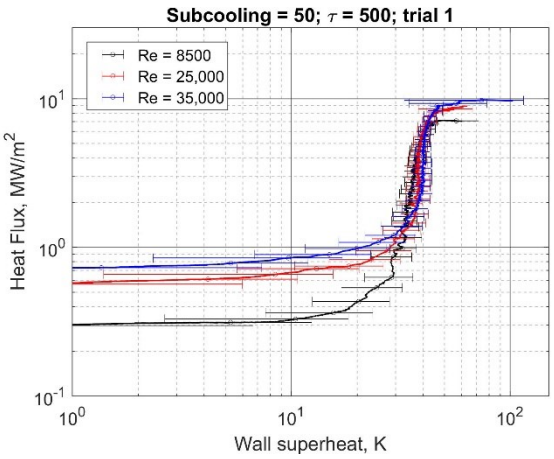
Subcooling = 50; τ = 500; trial 1
Re = 8500
Re = 25,000
Re = 35,000
Heat Flux, MW/m2
Wall superheat, K

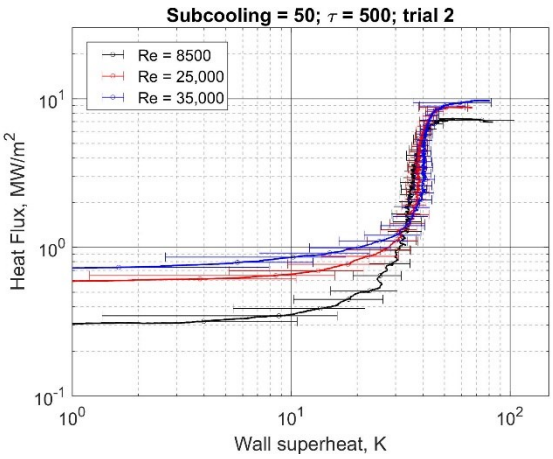
Subcooling = 50; τ = 500; trial 2
Re = 8500
Re = 25,000
Re = 35,000
Heat Flux, MW/m2
Wall superheat, K

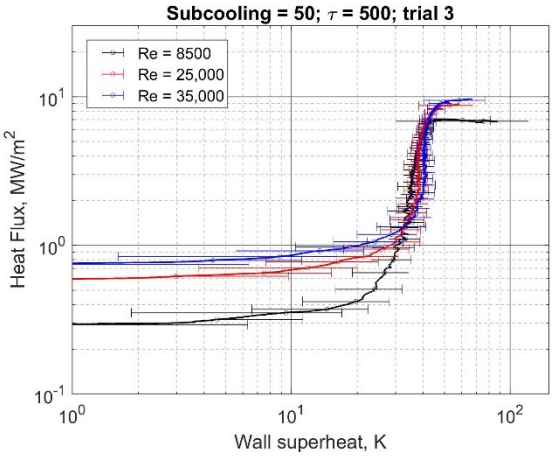
Subcooling = 50; τ = 500; trial 3
Re = 8500
Re = 25,000
Re = 35,000
Heat Flux, MW/m2
Wall superheat, K

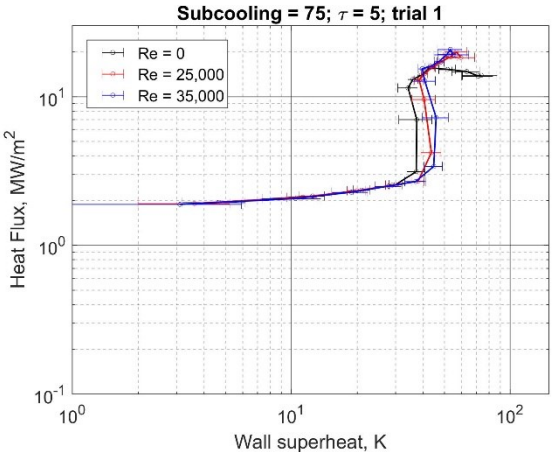
Subcooling = 75; τ = 5; trial 1
Re = 0
Re = 25,000
Re = 35,000
Heat Flux, MW/m2
Wall superheat, K

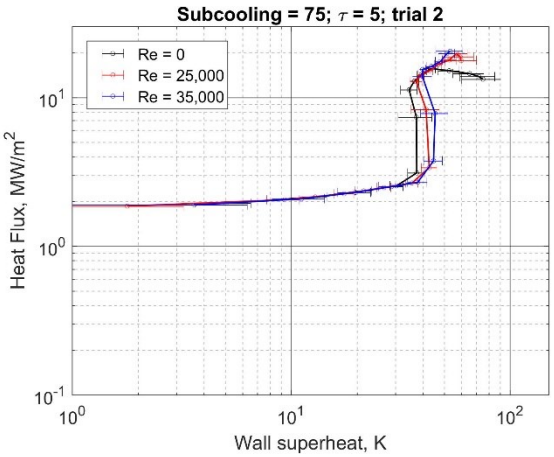
Subcooling = 75; τ = 5; trial 2
Re = 0
Re = 25,000
Re = 35,000
Heat Flux, MW/m2
Wall superheat, K

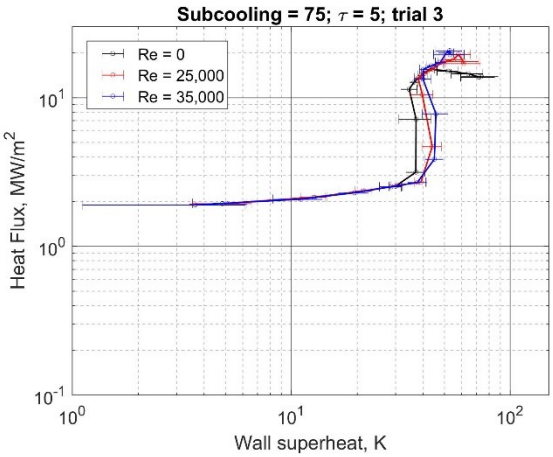
Subcooling = 75; τ = 5; trial 3
Re = 0
Re = 25,000
Re = 35,000
Heat Flux, MW/m2
Wall superheat, K

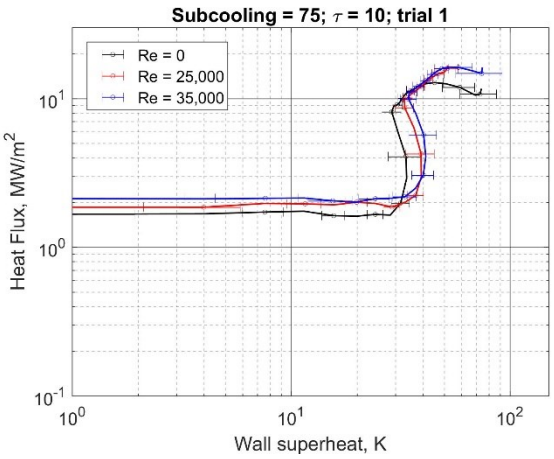
Subcooling = 75; τ = 10; trial 1
Re = 0
Re = 25,000
Re = 35,000
Heat Flux, MW/m2
Wall superheat, K

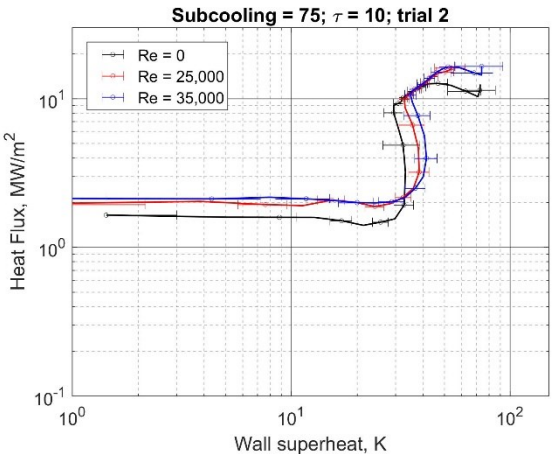
Subcooling = 75; τ = 10; trial 2
Re = 0
Re = 25,000
Re = 35,000
Heat Flux, MW/m2
Wall superheat, K

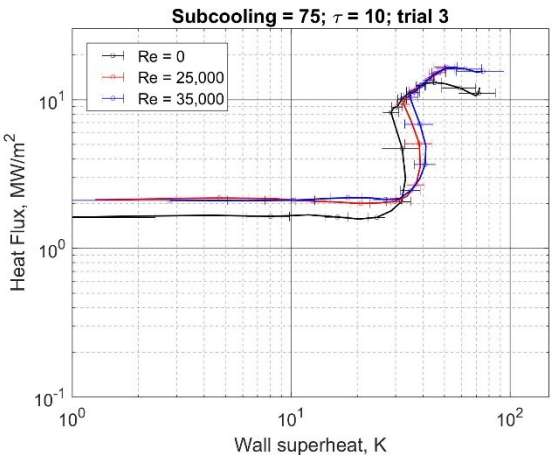
Subcooling = 75; τ = 10; trial 3
Re = 0
Re = 25,000
Re = 35,000
Heat Flux, MW/m2
Wall superheat, K

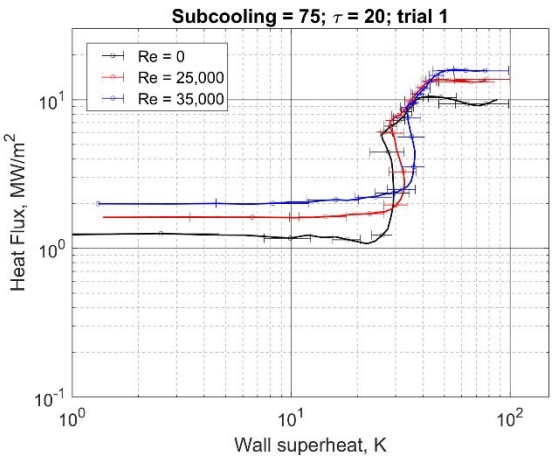
Subcooling = 75; τ = 20; trial 1
Re = 0
Re = 25,000
Re = 35,000
Heat Flux, MW/m2
Wall superheat, K

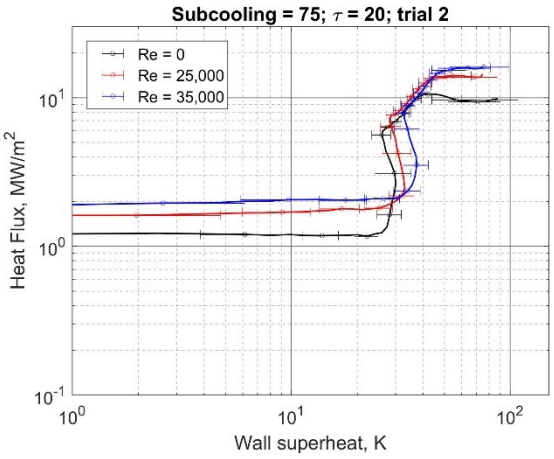
Subcooling = 75; τ = 20; trial 2
Re = 0
Re = 25,000
Re = 35,000
Heat Flux, MW/m2
Wall superheat, K

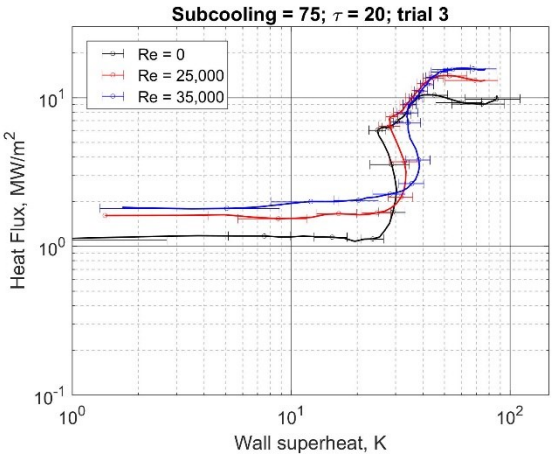
Subcooling = 75; τ = 20; trial 3
Re = 0
Re = 25,000
Re = 35,000
Heat Flux, MW/m2
Wall superheat, K

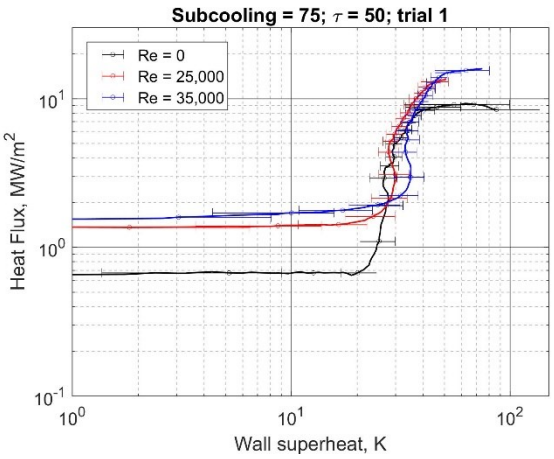
Subcooling = 75; τ = 50; trial 1
Re = 0
Re = 25,000
Re = 35,000
Heat Flux, MW/m2
Wall superheat, K

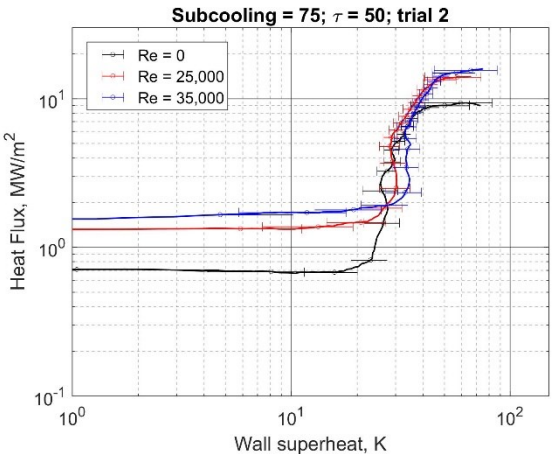
Subcooling = 75; τ = 50; trial 2
Re = 0
Re = 25,000
Re = 35,000
Heat Flux, MW/m2
Wall superheat, K

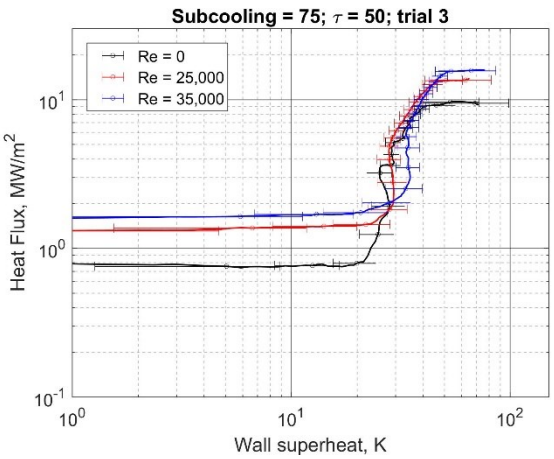
Subcooling = 75; τ = 50; trial 3
Re = 0
Re = 25,000
Re = 35,000
Heat Flux, MW/m2
Wall superheat, K

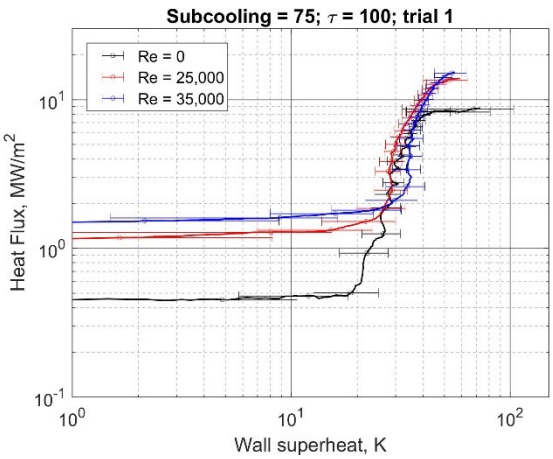
Subcooling = 75; τ = 100; trial 1
Re = 0
Re = 25,000
Re = 35,000
Heat Flux, MW/m2
Wall superheat, K

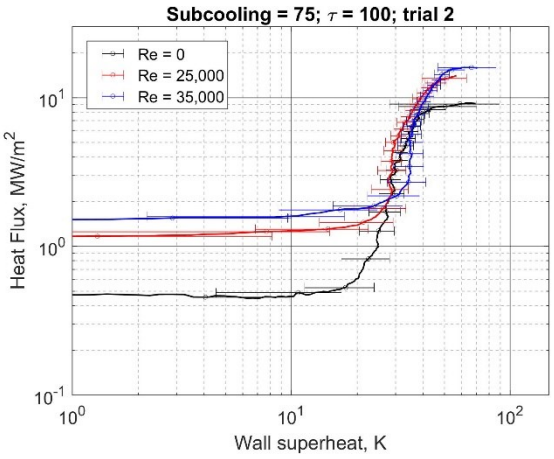
Subcooling = 75; τ = 100; trial 2
Re = 0
Re = 25,000
Re = 35,000
Heat Flux, MW/m2
Wall superheat, K

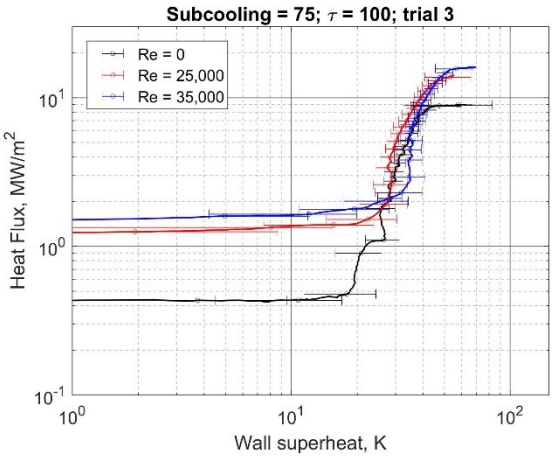
Subcooling = 75; τ = 100; trial 3
Re = 0
Re = 25,000
Re = 35,000
Heat Flux, MW/m2
Wall superheat, K

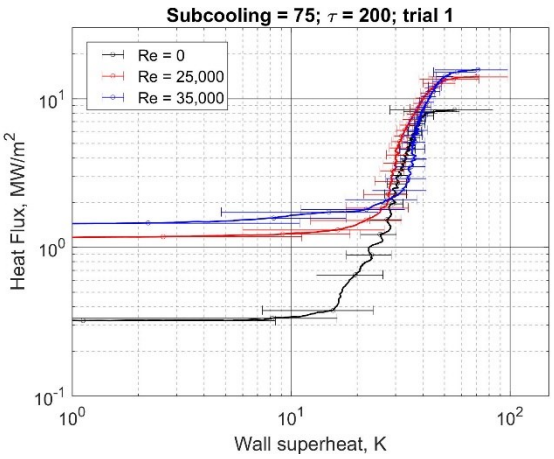
Subcooling = 75; τ = 200; trial 1
Re = 0
Re = 25,000
Re = 35,000
Heat Flux, MW/m2
Wall superheat, K

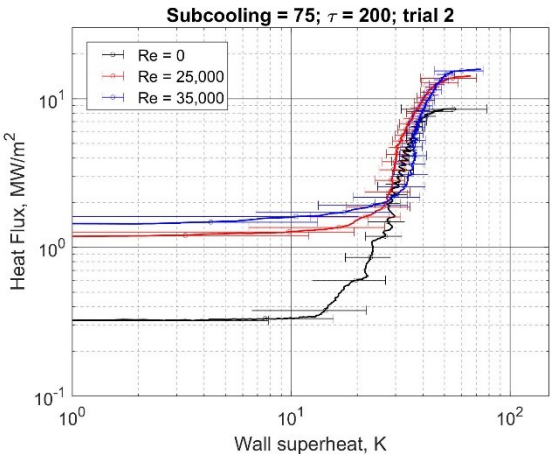
Subcooling = 75; τ = 200; trial 2
Re = 0
Re = 25,000
Re = 35,000
Heat Flux, MW/m2
Wall superheat, K

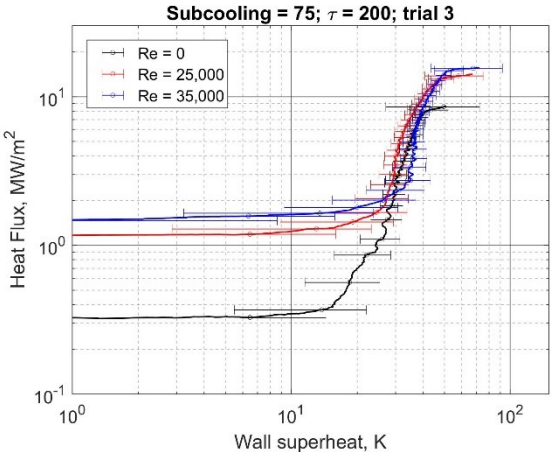
Subcooling = 75; τ = 200; trial 3
Re = 0
Re = 25,000
Re = 35,000
Heat Flux, MW/m2
Wall superheat, K

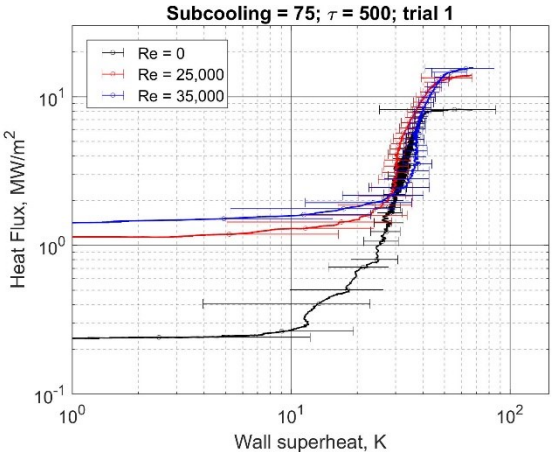
Subcooling = 75; τ = 500; trial 1
Re = 0
Re = 25,000
Re = 35,000
Heat Flux, MW/m2
Wall superheat, K

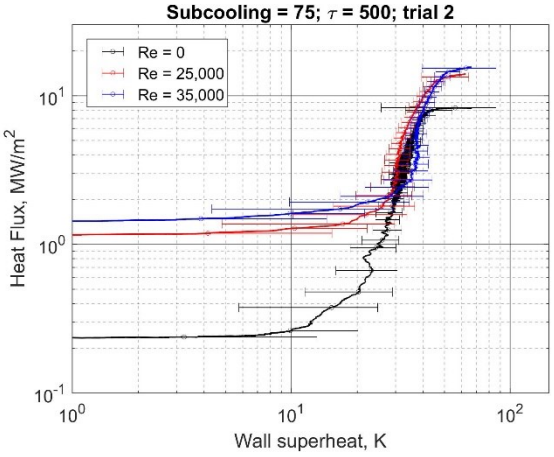
Subcooling = 75; τ = 500; trial 2
Re = 0
Re = 25,000
Re = 35,000
Heat Flux, MW/m2
Wall superheat, K

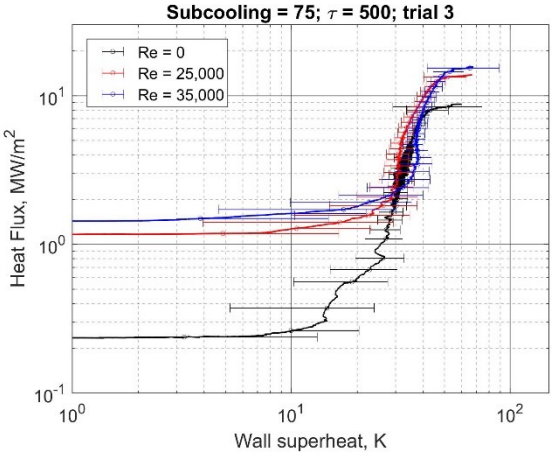
Subcooling = 75; τ = 500; trial 3
Re = 0
Re = 25,000
Re = 35,000
Heat Flux, MW/m2
Wall superheat, K

Appendix D. CHF values

In this section CHF values are plotted versus power escalation period, Reynolds number and subcooling. Additionally, CHF values with the corresponding uncertainties are tabulated.

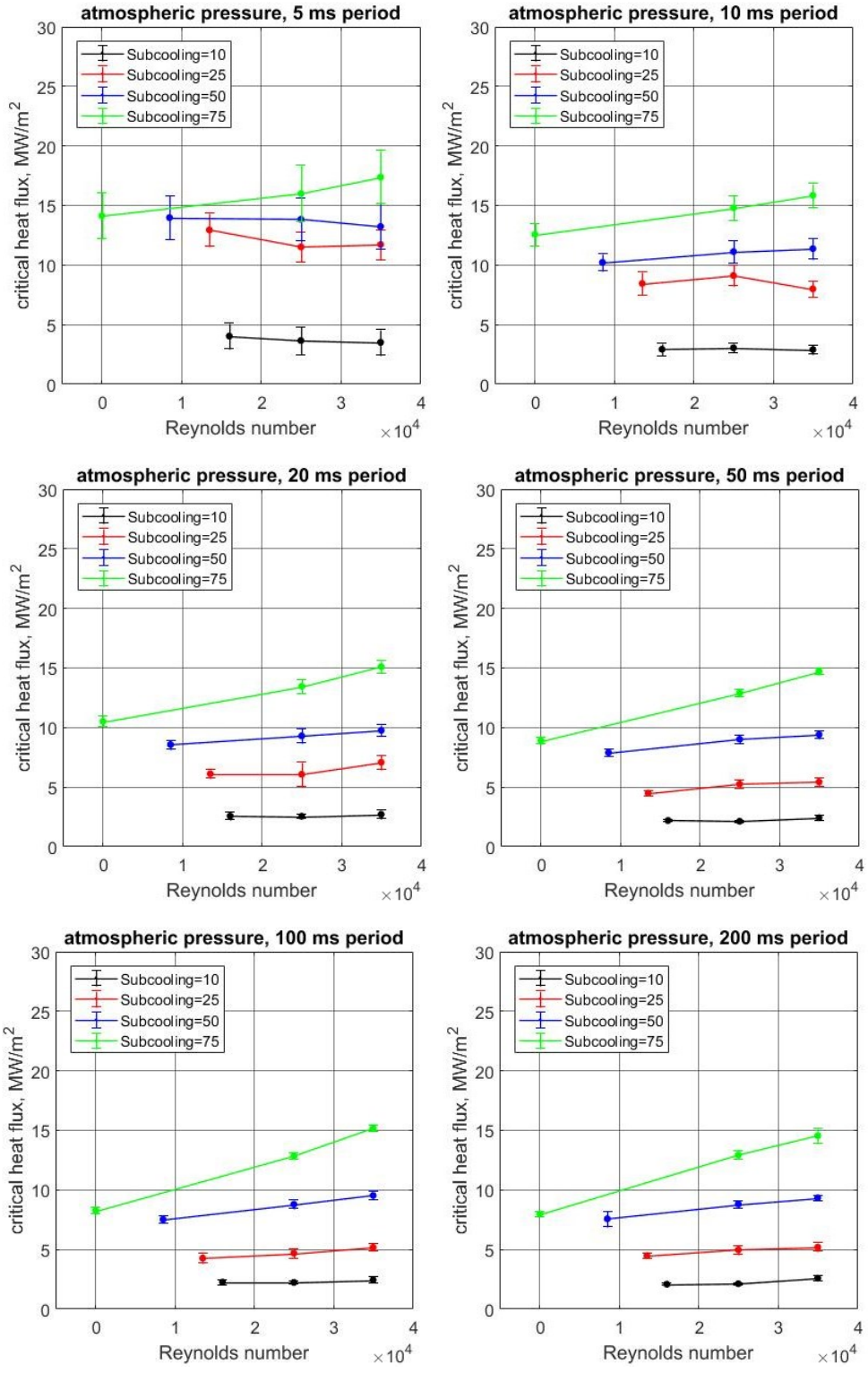

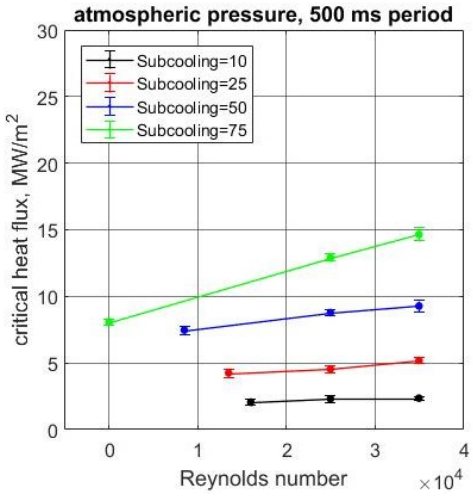
atmospheric pressure, 500 ms period
Subcooling=10
Subcooling=25
Subcooling=50
Subcooling=75
critical heat flux, MW/m2
Reynolds number
×10^4

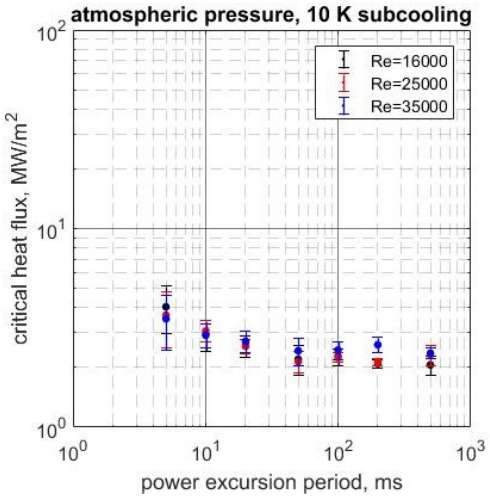
atmospheric pressure, 10 K subcooling
Re=16000
Re=25000
Re=35000
critical heat flux, MW/m2
power excursion period, ms

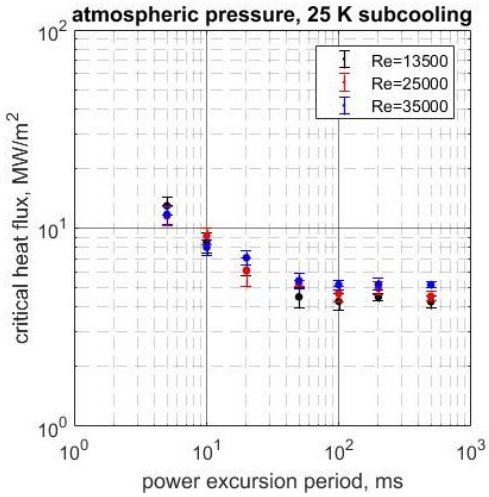
atmospheric pressure, 25 K subcooling
Re=13500
Re=25000
Re=35000
critical heat flux, MW/m2
power excursion period, ms

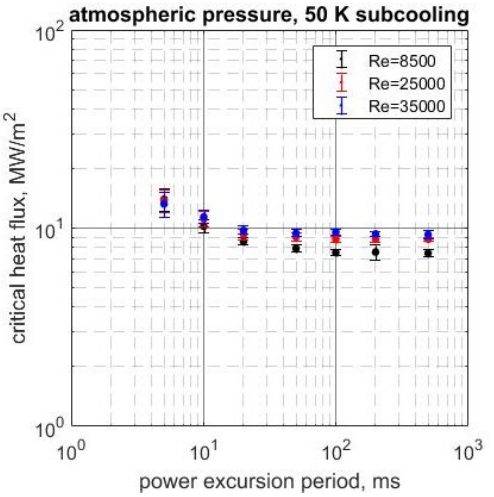
atmospheric pressure, 50 K subcooling
Re=8500
Re=25000
Re=35000
critical heat flux, MW/m2
power excursion period, ms

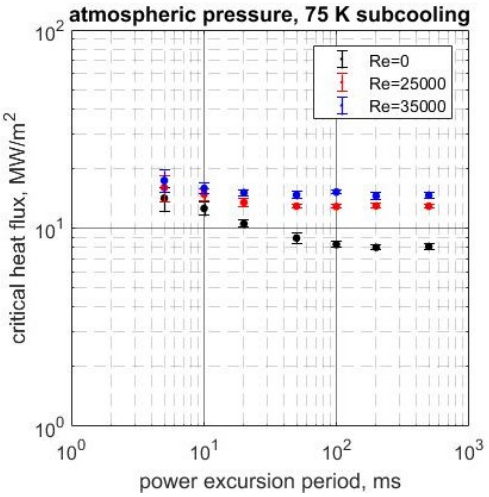
atmospheric pressure, 75 K subcooling
Re=0
Re=25000
Re=35000
critical heat flux, MW/m2
power excursion period, ms

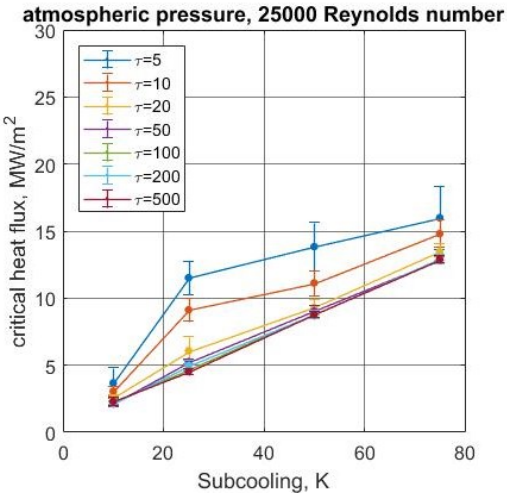
atmospheric pressure, 25000 Reynolds number
τ=5
τ=10
τ=20
τ=50
τ=100
τ=200
τ=500
critical heat flux, MW/m2
Subcooling, K

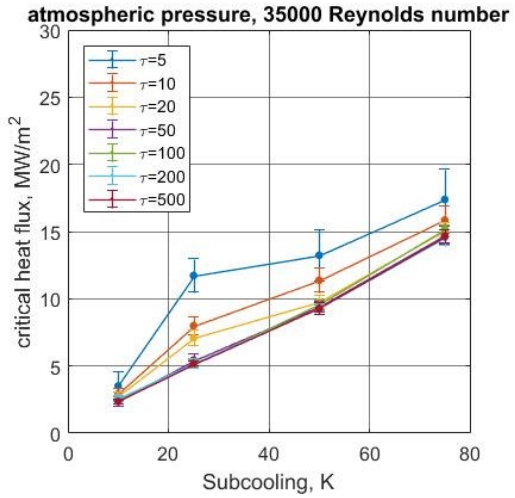

CHF values and uncertainties. All values are in MW/m^2					
Re = 0			75 K subcooling		
escalation period, ms	trial			mean	Uncertainty
	1	2	3		
5	13.98	14.28	14.18	14.15	1.93
10	12.29	12.40	13.02	12.57	0.95
20	10.31	10.60	10.64	10.52	0.43
50	8.46	8.93	9.34	8.91	0.51
100	8.32	8.03	8.44	8.27	0.29
200	7.92	7.88	8.18	7.99	0.24
500	8.27	7.99	7.98	8.08	0.24

CHF values and uncertainties. All values are in MW/m^2					
Re = 25000			75 K subcooling		
escalation period, ms	trial			mean	Uncertainty
	1	2	3		
5	17.14	15.24	15.62	16.00	2.37
10	14.43	15.14	14.86	14.81	1.02
20	13.71	13.61	13.05	13.46	0.59
50	12.90	12.79	13.00	12.90	0.29
100	12.97	12.90	12.69	12.85	0.28
200	12.67	13.03	13.14	12.95	0.35
500	12.76	13.01	12.95	12.91	0.26

CHF values and uncertainties. All values are in MW/m^2					
Re = 35000			75 K subcooling		
escalation period, ms	trial			mean	Uncertainty
	1	2	3		
5	17.34	17.50	17.32	17.39	2.24
10	15.59	16.05	15.93	15.86	1.02
20	14.95	15.14	15.23	15.11	0.52
50	14.73	14.15	15.27	14.72	0.65
100	15.18	15.20	15.21	15.20	0.26
200	14.19	15.14	14.33	14.55	0.59
500	14.29	14.57	15.10	14.65	0.49

CHF values and uncertainties. All values are in MW/m^2					
Re = 8500			50 K subcooling		
escalation period, ms	trial			mean	Uncertainty
	1	2	3		
5	14.01	13.61	14.33	13.98	1.84
10	10.13	10.47	10.07	10.22	0.73
20	8.44	8.52	8.74	8.57	0.38
50	7.64	8.02	8.03	7.90	0.32
100	7.28	7.62	7.68	7.53	0.29
200	7.12	8.23	7.37	7.57	0.64
500	7.25	7.40	7.77	7.47	0.32

CHF values and uncertainties. All values are in MW/m^2					
Re = 25000			50 K subcooling		
escalation period, ms	trial			mean	Uncertainty
	1	2	3		
5	13.79	13.76	13.98	13.84	1.81
10	11.70	10.71	10.99	11.13	0.94
20	9.76	9.22	8.93	9.30	0.60
50	8.68	9.05	9.32	9.02	0.41
100	8.73	8.57	9.09	8.80	0.34
200	8.93	8.96	8.54	8.81	0.30
500	8.66	8.77	8.92	8.78	0.23

CHF values and uncertainties. All values are in MW/m^2					
Re = 35000			50 K subcooling		
escalation period, ms	trial			mean	Uncertainty
	1	2	3		
5	13.11	13.72	12.88	13.24	1.90
10	11.54	11.66	10.93	11.38	0.88
20	10.05	9.52	9.70	9.76	0.47
50	9.47	9.11	9.66	9.41	0.39
100	9.81	9.32	9.50	9.54	0.34
200	9.22	9.36	9.46	9.35	0.23
500	9.55	8.86	9.43	9.28	0.43

CHF values and uncertainties. All values are in MW/m^2					
Re = 13500			25 K subcooling		
escalation period, ms	trial			mean	Uncertainty
	1	2	3		
5	13.60	13.07	12.19	12.95	1.38
10	7.68	8.65	9.03	8.45	0.95
20	6.32	5.78	6.25	6.12	0.36
50	4.58	4.92	3.98	4.49	0.51
100	4.49	4.49	3.84	4.27	0.41
200	4.63	4.52	4.32	4.49	0.20
500	4.24	4.53	3.98	4.25	0.31

CHF values and uncertainties. All values are in MW/m^2					
Re = 25000			25 K subcooling		
escalation period, ms	trial			mean	Uncertainty
	1	2	3		
5	11.47	11.94	11.14	11.52	1.23
10	8.44	9.48	9.46	9.13	0.86
20	6.80	NA[5]	5.35	6.08	1.03
50	5.35	5.27	5.17	5.26	0.18
100	4.28	5.08	4.70	4.69	0.42
200	4.99	5.30	4.65	4.98	0.38
500	4.34	4.50	4.76	4.53	0.25

[5] The data file for this test was corrupted

CHF values and uncertainties. All values are in MW/m^2					
Re = 35000				25 K subcooling	
escalation period, ms	trial			mean	Uncertainty
	1	2	3		
5	11.39	12.06	11.73	11.73	1.25
10	8.38	7.47	8.15	8.00	0.68
20	6.72	7.45	NA[6]	7.08	0.60
50	4.96	5.54	5.80	5.43	0.49
100	5.37	4.90	5.26	5.18	0.29
200	5.35	5.43	4.83	5.20	0.36
500	5.05	5.31	5.20	5.19	0.19

CHF values and uncertainties. All values are in MW/m^2					
Re = 16000				10 K subcooling	
escalation period, ms	trial			mean	Uncertainty
	1	2	3		
5	4.10	3.66	4.35	4.04	1.08
10	2.56	2.98	3.25	2.93	0.51
20	2.65	2.30	2.79	2.58	0.32
50	2.06	2.57	1.96	2.20	0.37
100	2.27	2.43	2.11	2.27	0.22
200	2.10	2.02	2.15	2.09	0.10
500	2.12	1.81	2.24	2.06	0.23

CHF values and uncertainties. All values are in MW/m^2					
Re = 25000				10 K subcooling	
escalation period, ms	trial			mean	Uncertainty
	1	2	3		
5	3.12	3.94	3.94	3.66	1.16
10	2.94	3.14	3.08	3.05	0.37
20	2.64	2.62	2.40	2.55	0.22
50	2.32	2.13	1.95	2.13	0.26
100	2.26	2.31	2.15	2.24	0.12
200	2.05	2.17	2.18	2.13	0.10
500	2.25	2.60	2.07	2.31	0.28

[6] The data file for this test was corrupted

CHF values and uncertainties. All values are in MW/m^2					
Re = 35000			10 K subcooling		
escalation period, ms	trial			mean	Uncertainty
	1	2	3		
5	3.28	3.43	3.82	3.51	1.07
10	3.09	2.78	2.85	2.90	0.39
20	2.69	2.99	2.45	2.71	0.34
50	2.83	2.35	2.09	2.43	0.39
100	2.71	2.37	2.27	2.45	0.25
200	2.62	2.40	2.79	2.60	0.23
500	2.33	2.27	2.48	2.36	0.14

Appendix E. Uncertainty quantification

The uncertainty quantification for heat flux and temperature measurements is presented below.

The standard deviation of the spatial distribution of temperature was significantly larger than the uncertainty of IR calibration technique. Therefore, the uncertainty of the average wall superheat (errorbars) is governed by the stochastic nature of boiling rather than the uncertainty in the IR temperature measurements.

The absolute uncertainty of CHF values $\Delta q''_{CHF}$ consists of three parts:

$$\Delta q''_{CHF} = \sqrt{(\Delta q''_m)^2 + (\Delta q''_t)^2 + (\sigma_{CHF})^2} \tag{E1}$$

where $\Delta q''_m$ – absolute measurement uncertainty; $\Delta q''_t$ – absolute temporal uncertainty related to the frame rate of the IR camera. For each combination of Reynolds number and escalation period the experiment was repeated three times. Each time a slightly different value of CHF was measured. The standard deviation of measured values σ_{CHF} is included in Eq. E1.The heat flux at CHF was calculated from readings of current (I) and voltage (U) across the heater.

$$q'' = \frac{I \cdot U}{A_H} \tag{E2}$$

where A_H – heater area. The measurement uncertainty includes uncertainties of voltage ΔV and current ΔI readings:

$$\frac{\Delta q''_m}{q''} = \sqrt{\left(\frac{\Delta V}{V}\right)^2 + \left(\frac{\Delta I}{V}\right)^2} \tag{E3}$$

The uncertainty of the heater area was omitted because it was much smaller than uncertainties of current and voltage readings. The occurrence of CHF was determined through the analysis of IR videos. Therefore, the temporal uncertainty associated with the identification of CHF is the inverse of the camera frame rate:

$$\Delta t = \frac{1}{FR} = \frac{1}{2{,}500} = 0.4 \text{ ms} \tag{E4}$$

At short periods the heat flux could increase significantly over this period of time. Therefore, a temporal uncertainty on the CHF identification was calculated as follows:

$$\Delta q''_t = q''_0 \cdot \left(e^{t_{CHF}/\tau} - e^{(t_{CHF}-\Delta t)/\tau}\right) \tag{E5}$$

where q''_0 – applied heat flux at the beginning of the transient; t_{CHF} – time when CHF happens, which is calculated as:

$$t_{CHF} = \tau \cdot \ln\left(\frac{q''_{CHF}}{q''_0}\right) \tag{E6}$$

Note, that although the fraction of the heat flux that goes to water could be much smaller than the total applied heat flux, it is more conservative to calculate the temporal uncertainty using the total applied heat flux. For all measurements a temporal uncertainty dominates at short periods whereas the standard deviation is the biggest contributor to the long period uncertainty. The measurement uncertainty for all tests was in the order of 0.1 MW/m^2.